MASTER THESIS

PHYSIK-DEPARTMENT E62 - DENSE AND STRANGE HADRONIC MATTER

Exploring the Properties of Quark-Gluon Plasma with Differential Studies of Anisotropic Flow Fluctuations at the Large Hadron Collider

Author: Anton RIEDEL

Supervisor: Dr. Ante BILANDZIC

May 3, 2022

Contents

List of Figures

List of Tables

Abstract

Quark-gluon plasma (QGP) is an extreme state of matter, characterized by deconfined quarks and gluons, which can move freely. Its properties have been probed by studying the collective behavior of the particles produced in ultra-relativistic heavy-ion collisions. Measuring anisotropic flow, the hydrodynamic response of the QGP to the initial state anisotropies, has allowed to constrain some of its transport properties, like the specific shear viscosity η/s. Its value is lower than that of every other known liquid, causing QGP to be dubbed a "perfect" fluid.
Anisotropic flow is quantified with flow amplitudes and symmetry planes, which are degrees of freedom in the Fourier series expansion of the azimuthal distribution of produced particles. The development of multiparticle correlations techniques, followed by the introduction of the formalism of uni- and multivariate cumulants, have revolutionized anisotropic flow analysis. These methods combined allow the precision measurement of flow amplitudes. Measurements of different collisions systems with various center of mass energies have shown that the studies of flow amplitudes are not sufficient to constrain all the properties of the QGP. Measurements have shown that there exists a genuine correlation between different flow harmonics which hold new and independent information about the QGP. These correlations can, for instance, be used to constrain the temperature dependence of the specific shear viscosity $\eta/s(T)$.
This work presents the mathematical formalism and the generic framework for computing multiparticle correlators. With these correlators, arbitrary cumulants as well as Symmetric Cumulants (SC) can be computed using the individual flow amplitudes as fundamental observables in the cumulant expansion. Cumulants are used for estimating the value of flow harmonics and SCs are used for estimating the correlation between two or more flow harmonics. The presented methods are being tested and verified using Toy Monte Carlo simulations. The robustness of the observables to systematic biases origination from non-flow correlations will also later be verified by analyzing data from the HIJING event generator.
This work further presents the first differential study of multi-harmonic correlations obtained with Symmetric Cumulants, SC(2,3), SC(2,4) and SC(2,3,4). We present the first results for symmetric cumulants as functions of pseudorapidity η and transverse momentum p_{T} utilizing Pb–Pb collision at LHC from 2010 collected by the ALICE detector with a collision energy of $\sqrt{s_{\mathrm{NN}}} = 2.76\,\mathrm{TeV}$ and show how granular the correlations can be extracted using the available statistics. These differential studies provide new and independent constraints both on initial conditions and on the properties of the QGP.

1. Introduction

In this chapter we present a brief introduction into all necessary physical concepts to understand the properties of Quark-Gluon Plasma (QGP) and how they can be determined by measuring anisotropic flow. In section 1.1 we review the theory of Quantum Chromodynamics (QCD) and discuss how two of its main features emerge: confinement and asymptotic freedom. These features have a profound impact on how the QGP behaves. In section 1.2 we discuss the QCD phase diagram and what conditions are necessary for the QGP to form. These conditions can be met in heavy-ion collisions. Therefore we examine the physics at play in heavy-ion collisions in section 1.3. The physical effects in heavy-ion collision are very sensitive to the initial conditions of the collision so it is important to be able to classify them. This is commonly done with dividing collisions into centrality classes. The phenomenon of anisotropic flow is introduced in section 1.4 and how it depends on the hydrodynamic properties of the QGP. The physics of anisotropic flow are generally accessed by measuring so-called flow harmonics. However, measuring the flow harmonics alone is not enough to fully constrain the properties of the QGP or to decide if one theoretical model describes the physics of the QGP better than another. Therefore, we show in section 1.5 how the fluctuation between different flow harmonics has been used to gain more information about the QGP and how to constrain its properties even further.

1.1. Quantum Chromodynamics

Quantum Chromodynamics (QCD) is a non-Abelian $SU(3)$ gauge theory that describes the strong interaction between quarks and gluons[33, 34]. The associated charge, the color, gives rise to the name Chromodynamics. In analogy with the three primary colors, the color charge can take the three values: red, blue and green. Quarks carry one type of color, antiquarks carry one type of anticolor (antired, antiblue or antigreen). The mediators of QCD are called gluons, which also carry color charge. This is in contrast to quantum electrodynamics (QED), which only has one single and neutral vector boson, the photon. There are a total of eight gluons, each of which can be related to the eight 3×3 Gell-Mann matrices of $SU(3)$. Since the gluons themselves are charged, this implies that they can interact with each other.
Hadrons are composite bound state of quarks and antiquarks. They are categorized mainly into two families: mesons and baryons. Mesons are bound states consisting of a

quark and anti-quark, while baryons consist of three quarks. The quark-antiquark pair inside a meson carry opposite color charge and the quarks inside a baryon carry different color, making both of these type of particles colorless. In fact, a single free quark or a bound state which, in total, is not colorless, have yet to be observed. The interactions between quarks and gluons is described by the QCD Lagrangian density[30]

$$\mathcal{L}_{QCD} = \sum_q \bar{q}(x)\big(i\gamma_\mu D^\mu - m_q\big)q(x) - \frac{1}{4g^2}\mathrm{Tr}G^{\mu\nu}(x)G_{\mu\nu}(x), \tag{1.1}$$

where $q(x)$ are the quark fields, m_q the masses of the quarks, γ_μ the Dirac matrices, g the coupling constant, $G^{\mu\nu}(x)$ the gluon field strength tensor and D_μ the covariant derivative. It is defined as

$$D_\mu = \partial_\mu - iA^a_\mu t^a, \tag{1.2}$$

where A^a_μ are the gauge fields and t^a the generators of $SU(3)$. Using eq. (1.2), the field strength tensors can be written as

$$G^{\mu\nu}(x) \equiv i[D^\mu, D^\nu] = \partial^\mu A^\nu(x) - \partial^\nu A^\mu(x) i[A^\mu(x), A^\nu(x)]. \tag{1.3}$$

The first term in eq. (1.1) describes the propagation of the quarks and their interaction with gluons. The second term describes the propagation of the gluons and how they interact among themselves.
The coupling constant characterizes the strength of the interaction. In QED, for instance, the coupling constant α_{QED} describes how strongly two electric charges attract or repel each other. The force is strong at small distances, α_{QED} is large, and small at large distances, α_{QED} is small. The exact opposite is observed in QCD and its coupling constant α_S. At small distances, or equivalently at large energies, the coupling constant is small. When the distance increases or the energy decreases, the coupling increases. In Quantum Field Theories (QFT), such as QCD, the beta function expresses the dependence of the coupling constant α as a function of an energy scale Q[33]. It can be written as

$$\beta(\alpha) = \frac{\partial\alpha}{\partial \ln Q^2}. \tag{1.4}$$

In the case of QCD, its beta function is written as the series

$$\beta(\alpha_S) = -\Big(b_0\alpha_S^2 + b_1\alpha_S^3 + b_2\alpha_S^4 + \ldots\Big) \tag{1.5}$$

where b_i are the $(i+1)$-loop coefficients[35]. The most important feature is the minus sign in eq. (1.5). From the result that $b_0 > 0$[33], the overall signature indicates that the coupling constant decreases with energy. At very large energies the coupling becomes so small that the quarks become free particles. This phenomenon is known as asymptotic freedom and is a property of non-Abelian gauge theories[8, 27, 28]. The running of α_S is shown in fig. 1.1. On the other hand, since the coupling increases as the distance between quarks increases, its is not possible to observe quarks outside of a, in total, colorless bound state. This feature of QCD is known as confinement[7]. If energy is provided

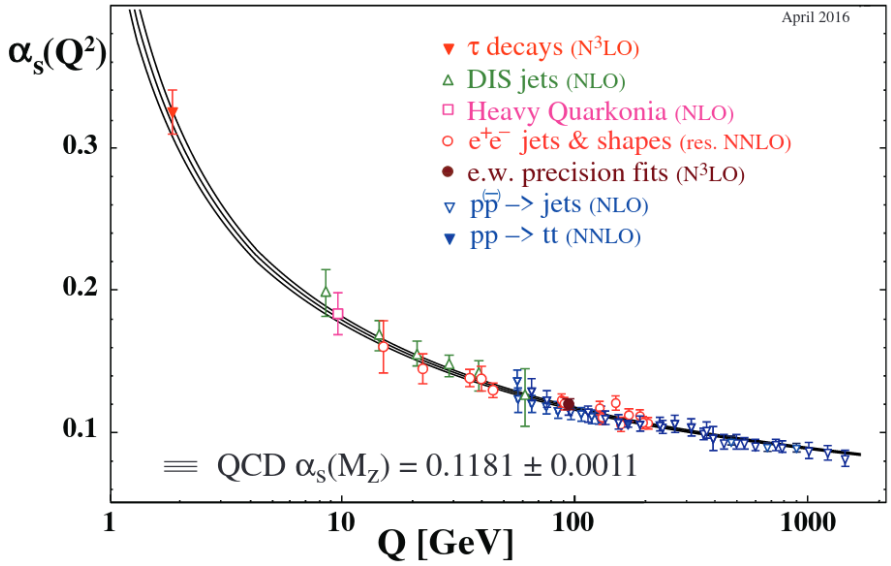

Figure 1.1.: Running of the coupling constant α_S as a function of the energy scale Q measured using different processes[35].

to separate two quarks, the energy content of the field between them also increases. This continues until such point that it becomes energetically more favorable to create a new pair of quark-antiquark than further separating the two original quarks. Therefore, instead of detecting a single quark, new mesons are produced. In collision in particle accelerators, the provided energy is enough to produce a plethora of new quarks, gluons and other force carrying bosons which then will create any possible particle species which are subsequently measured in the detectors.
The running of α_S does not only influence the phenomena related to the strong force, it also prevents solving the QCD Lagrangian at small energies using perturbation theory[34, 28]. For large energies, hence small α_S, summing the contributions of a finite amount of interaction terms gives a good approximation to the solution of the Lagrangian. Many important measurements have been tested with perturbative QCD, like the ratio of the production cross section of $e^-e^+ \rightarrow$ hadrons and $e^-e^+ \rightarrow \mu^-\mu^+$. For small energies, hence large α_S, non-perturbative techniques have to be used to solve the Lagrangian. One approach is lattice QCD[13]. In this numerical approach quark fields are placed on the nodes of space-time lattice while the connection between them are the gluon fields. The lattice spacing is denoted with a and all physical quantities are then expressed in terms of the spacing. The spacing a can be changed by changing the coupling in the QCD Lagrangian. Finally, continuum QCD is restored when the spacing a tends to zero.

1.2. Quark-Gluon Plasma

The two main features of QCD, asymptotic freedom and confinement, have important consequences on the behavior of quark matter. As such, it is of interest to study its thermodynamic properties as a function of temperature T and the net baryon density. The phase diagram of QCD is represented in fig. 1.2. At low T and densities equal to one,

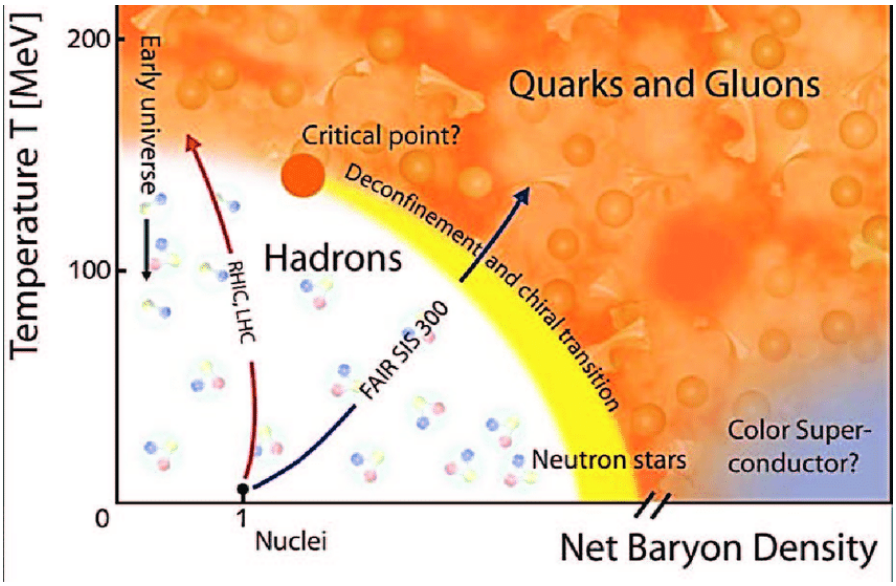

Figure 1.2.: Schematic of the QCD phase diagram where the different phases are indicated[3]. The interrogation marks indicate some remaining open questions. The QGP phase is colored in orange.

the quarks are confined inside hadrons and form ordinary matter. For lower densities the matter exists in a hadronic gas state. If the density is raised instead, it is assumed that the matter takes on the same properties as the matter inside neutron stars and may even form a color superconductor at even higher densities. However, at large temperatures, the quark matter forms the QGP. Whether the transition is a proper phase transition or a smooth-crossover is also still an open question.
After the introduction of the quark model by Gell-Mann [6] and Zweig[39, 40], hadrons could be explained as the bound state of quarks and gluons. The existence of deconfined quarks was considered later and this state has been dubbed as Quark-Gluon Plasma. At first perturbation theory at high temperatures suggested the QGP behaved like a weakly interacting gas[30], but as was later discovered by analyzing experimental data from LHC[10] and RHIC[12, 32], that is not the case. With the measurements of various effects like anisotropic flow and jet quenching, it has been found that the QGP behaves like a strongly interacting fluid. Moreover, a comparison with the predictions of relativistic hydrodynamics with the data has shown that the ratio between the shear viscosity over entropy density η/s, also known as the specific shear viscosity, is close to the lowest

theoretical bound of $1/4\pi$[16]. That is why it is sometimes referred to as a "perfect" liquid[26, 10, 12].
Figure 1.2 also shows the conditions of the early universe, small densities and high temperatures. QCD predicts that a high temperature QGP filled the universe in the first few microseconds after the Big Bang[29]. This lasted until the universe expanded and cooled down sufficiently for the quarks and gluons to recombine and form hadrons. Investigation of the QGP is therefore fundamental to get a clear picture of the phase diagram of quark matter as well as getting a better understanding of the evolution of the universe in its early stages.

1.3. Heavy-ion Collisions

QGP can be produced through ultra-relativistic collisions of heavy ions. Since its discovery in 2000, it has been observed and studied for many different collision systems and nucleon-nucleon center of mass energies $\sqrt{s_{NN}}$. Some motivation for the various configurations are the study of the formation onset of the QGP or how the different shapes of the ions influence the QGP properties. For instance, in this thesis we analyze the data set of Pb–Pb collisions at $\sqrt{s_{NN}} = 2.76\,\text{TeV}$ recorded in 2010 with the ALICE detector at the LHC. The produced QGP undergoes a time evolution as illustrated by fig. 1.3. Heavy-ions are stripped of all their electrons and accelerated to velocities close to

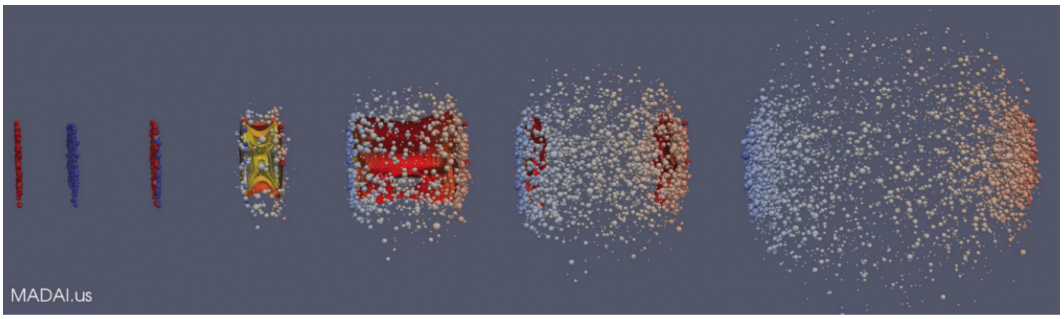

Figure 1.3.: Simulation of the time evolution of a relativistic heavy-ion collision[20].

the speed of light. At these speeds relativistic Lorentz contraction become non-negligible and the collision of the two ions can be seen as the collision of two discs in the laboratory frame. This is illustrated in the two left panels in fig. 1.3. The Lorentz contraction has two important consequences. Firstly, the density of quarks and gluons is higher in the disc than in the initial ion. Secondly, the collision time is a well defined value, identical for all nucleons[31].
The geometry of the collision influences the evolution of the produced matter. The overlap of the ions at the time of impact is with the impact parameter b, defined as the distance between the centers of two nuclei. Collisions with $b = 0$, when the nuclei perfectly overlap,

are called head-on or central collisions. If b is close to the sum of the radii the ions barely scratch each other, the collision is called peripheral. The reaction plane, or collision plane, is the plane spanned by the impact parameter vector $\mathbf{b}$, which points from the center of one ion to the other, and the beam axis z. Its angle with respect to the x-axis is denoted with Ψ_{RP}. An illustration of the collision geometry is shown in fig. 1.4.

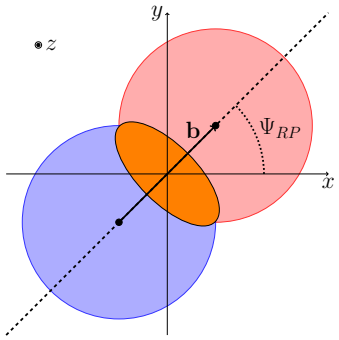

Figure 1.4.: Ideal collision geometry between two heavy ions, indicated with a shaded red and blue circle. The interacting region is marked with an orange ellipse. The arrow indicates the impact parameter vector $\mathbf{b}$. The angle of the reaction plane Ψ_{RP} is denoted with a dashed line. Based on [36].

The nucleons in the colliding ions can be divided into two groups. The ones which take part in the collision, the participants, are all inside the overlapping region, here indicated with an orange ellipse. The nucleons which do not contribute to the collision, the spectators, are inside the shaded blue and red region. While both the impact parameter and the reaction plane can be used to make theoretical prediction, they are not experimentally accessible. However, it is possible to measure the number of newly produced particles, the released energy in the collision and the number of spectators[30]. The number of newly produced particles is also called multiplicity. Both the multiplicity and the released energy are proportional to the number of participants and their respective distribution can be used to categorize the events into centrality classes. The distribution of the 5 % highest multiplicity events can be related to the 5 % most central collisions[5]. Figure 1.5 illustrates the centrality classification and its connection to the impact parameter and the shape of the overlapping region of the collision. For an event with a given impact parameter, the multiplicity or number of participants can be related to theoretical quantities like the number of wounded nucleons, i.e. the nucleon which interacted at least once, and the number of binary collisions between nucleons. This can be done with the help of the Glauber model[30, 19, 2, 18]. There are two versions of the Glauber model. The one described here and the one mostly used in practice is the Monte Carlo Glauber (MC-Glauber) model. The nucleon density of the initial ions in the MC-Glauber model is given by a Woods-Saxon distribution[30] and the number of binary collision is approximated as the number of successive independent interactions of the nucleons under the assumption that the nucleons do not change their path after an interaction. Moreover, the MC-Glauber model takes as one of its inputs the nucleon-nucleon cross-section

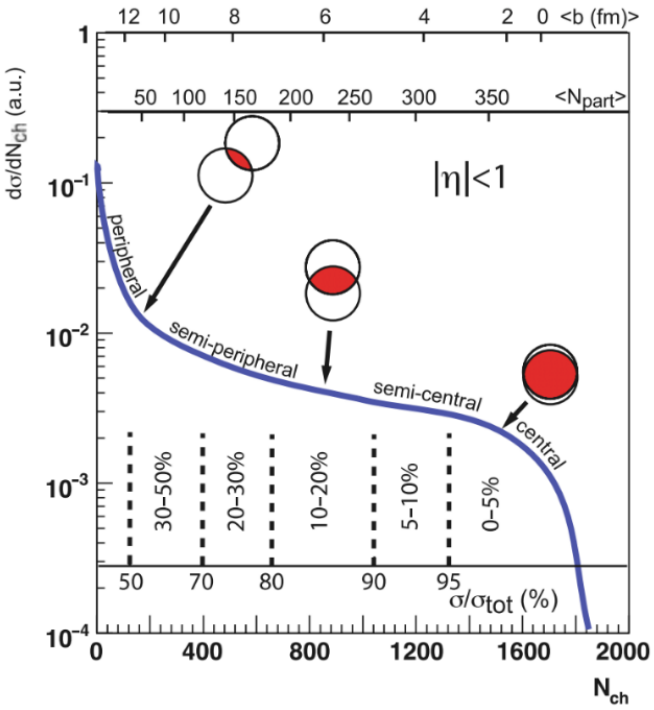

Figure 1.5.: Schematic view of the definition of centrality classes based on the multiplicity of an event[30]. The corresponding impact parameter b and the number of participants is shown.

obtained from pp collision at various energies and assumes that they stay constant after each individual nucleon-nucleon collision.
Once the ions collide, the evolution of the quark matter begins. The first processes to happen are so-called hard process with large transferred momenta. These hard particles are the origin of phenomena like jets, direct photons or pairs of dileptons and can be traced back to this pre-equilibrium phase. The bulk of the quarks and gluons liberated by the collision produces a volume of matter that evolves until thermal equilibrium is reached. In the pre-equilibrium state hydrodynamics can not be applied yet. Here other models are used, like the MC-Glauber model or TRENTO[21]. As the state continues to develop and the partons interact with each other the volume quickly reaches a local thermal equilibrium. The phase after the thermalization is known as QGP, where relativistic viscous hydrodynamics can be applied. It is visible after the fourth panel in fig. 1.3. The QGP expands until the local thermal equilibrium disappears. The density and temperatures decrease until they reach a point where the quarks and gluons can recombine into hadrons. This corresponds to the crossing between the phases in the QCD phase diagram in fig. 1.2. This phase is called hadronization and leads to the formation of a hot hadronic gas. The energy density continues to decrease as the gas expands. The hadrons within are constantly changing due to inelastic interaction until the so-called chemical freeze-out. At this point the number of particles and species do not change any more but the particle momenta can still change due to elastic interactions. The next stage is the thermal (or kinetic) freeze-out, when all elastic scatterings stop and the final state particles fly freely to the detectors. The only changes happening to particles are now the decay of particles and the interactions with the detector material. Lastly, as the collision between two heavy ion simulate the conditions which are predicted to be the ones of the Big Bang and the time evolution of the produced matter is similar in the two cases, relativistic heavy-ion collisions are sometimes called Little Bangs[32, 11].

1.4. Anisotropic flow

It was first proposed to describe the evolution of the system created by the collision of two ions by Landau in 1953[17]. Hydrodynamic predictions were first confirmed with measurements at RHIC where they were found to in good agreement with the data. Ideal hydrodynamics can only be applied if the system is close to thermodynamic equilibrium. Hydrodynamic laws are based on the thermodynamic properties of the system, like temperature, pressure and energy density and these quantities are well defined only if the system is close to equilibrium[15]. Hence, the hydrodynamic description is only valid from the thermalization of the interacting matter up to the chemical freeze-out. This also means that initial conditions have to be provided for an accurate description. We already discussed how the MC-Glauber model can be used to obtain these initial conditions.
In non-central collisions the overlapping region of the two colliding nuclei is to leading order elliptical in the transverse plane as illustrated by fig. 2.1[38]. But this geometrical

asymmetry fails to explain the results observed in central events as the overlap region is mainly circular. There is another source of anisotropy in the system which is given by the nature of the collision of two ions. They are not ideal, smooth spheres, but composite objects consisting of protons and neutrons. The position of the nucleons fluctuate event-by-event, which leads to deformations of the overlapping region. These fluctuations are present in all centralities, but they dominate in events with small centrality.
The spatial asymmetry results in anisotropic pressure gradients inside the volume which contains the thermalized nuclear matter[25]. The insertion of these pressure gradients inside the equation of motions leads to a transfer of the anisotropy in the coordinate space into an isotropy in momentum space. This transfer, called anisotropic flow phenomenon or simply anisotropic flow, can therefore be interpreted as the medium response to the initial geometry of the system[38, 25]. Figure 1.6 summarizes the full phenomenon.

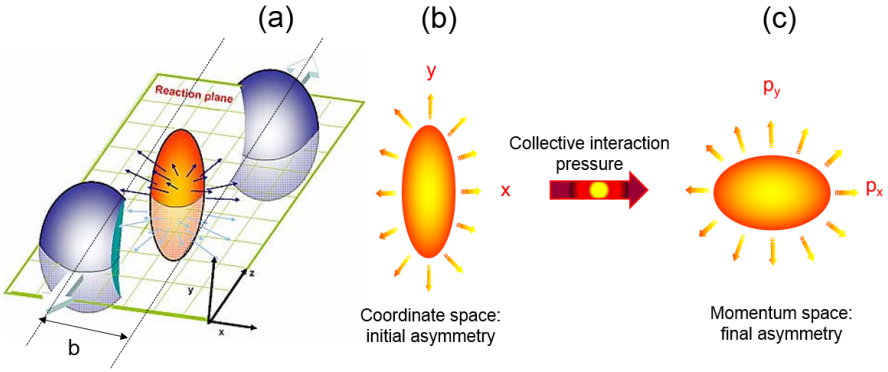

Figure 1.6.: Illustration of the anisotropic flow phenomenon, taken from[24]. The creation of the elliptic shape of the interacting volume in non-central collisions (a) and the transfer of coordinate space anisotropies (b) to momentum space anisotropies (c).

1.5. Correlation between flow amplitudes

The idea to measure the correlation between two different flow amplitudes v_n and v_m has been first proposed in [23] and the idea has been further refined in the context of the newly developed generic framework in [4]. Since then SCs have become one of the most commonly known observables to measure the genuine correlations between v_n and v_m. The generalization to compute the correlations between three and more flow amplitudes was performed in [20].
The measurement of the correlation between flow harmonics is of great interest because they contain information that cannot be gained by measuring the individual flow harmonics. In particular, even though by measuring the values of the flow harmonics it is possible to constrain the value of the specific shear viscosity of the QGP, it is not

possible to make a statement about its functional dependence on the temperature. This conundrum is illustrated in fig. 1.7. The results have been presented with the theoretical

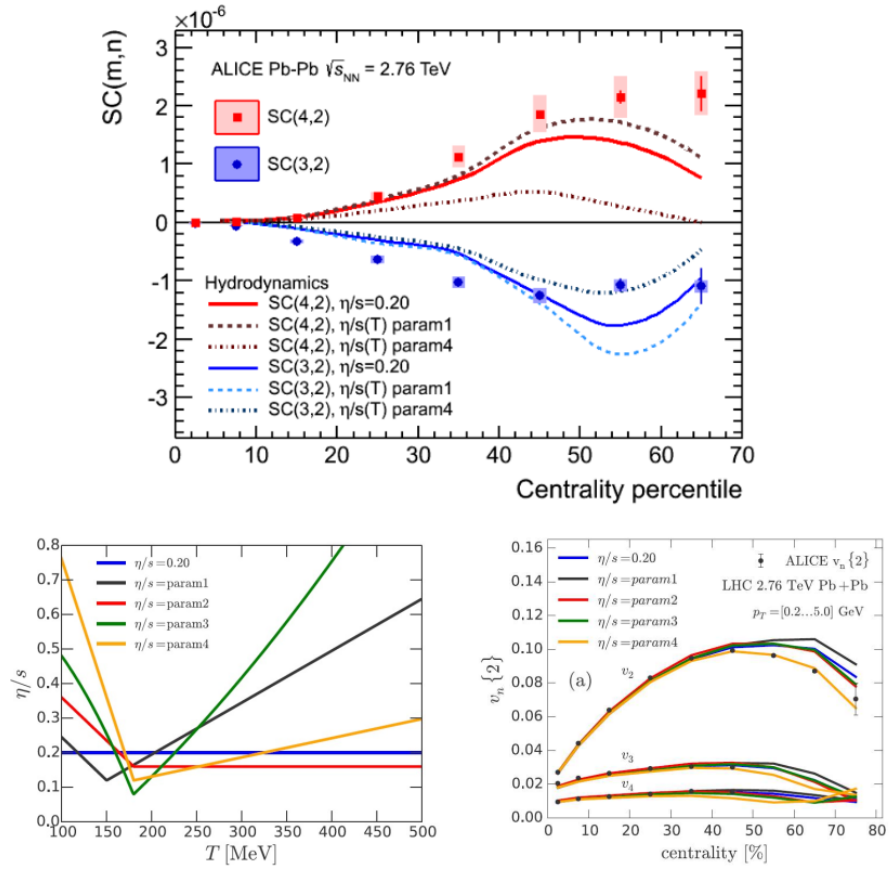

Figure 1.7.: Figure taken from [20]. In the top plot the centrality dependence of the correlation between v_2 and v_4 (SC(2,4)) in red and v_3 and v_4 (SC(3,4)) in blue is shown from ALICE in Pb–Pbcollisions at $\sqrt{s_{\mathrm{NN}}} = 2.76\,\mathrm{TeV}$[1]. The results are compared to the theoretical predictions of different parameterizations of $\eta/s(T)$ in the bottom left. The various parameterizations have the same average value $\langle \eta/s(T) \rangle = 0.20$[22]. The centrality dependence of the two particle cumulants of various v_n with the corresponding theoretical prediction to the parameterizations is shown in the bottom right[22].

predictions for various parameterizations of the temperature dependence of η/s. These parameterization are shown in the bottom left panel of fig. 1.7 and they all have the same average $\langle \eta/s(T) \rangle = 0.20$[22]. We can draw two conclusions from these results. Firstly, the SCs are sensitive to $\eta/s(T)$, while the measurement of v_n are sensitive only to $\langle \eta/s(T) \rangle$, meaning there is no distinction between the details of the temperature dependence. Secondly, no single parameterization can describe both SC(4,2) and SC(3,2) in all centrality classes at the same time. From these two points it is clear that the SCs give information

that is not accessible from the measurements of single flow amplitudes and they allow the application of new constraints on the theoretical model used to describe the QGP evolution and properties. In this work we go even further and extract even more information about the QGP with the help of SCs by studying them more differentially. We extract the transverse momentum and pseudorapidity dependence of the correlation between two and three flow harmonics.

2. Analysis Framework

In this chapter we present the theoretical framework and analysis techniques to study anisotropic flow at the Large Hadron Collider. We start by introducing the underlying probability density function of azimuthal angles of particles produced in heavy-ion collisions in section 2.1. The parameters of this function are the symmetry planes and anisotropic flow harmonics and are directly connected to the properties of the QGP. In this thesis we only study the anisotropic flow harmonics. In section 2.2 we show the generic principle by which we can estimate the value of a flow harmonic from data if the symmetry planes are known. Since there is no reliable way to estimate symmetry planes in a single heavy-ion collision, we will introduce in section 2.3 multiparticle correlation techniques which are a precision tool for estimating flow harmonics in heavy-ion collision with large multiplicities. The draw back with using multiparticle correlation techniques is that their (naive) computation for higher-order observables requires multiple passages over the data, making them computational very expensive. However, using the formalism of Q-vectors, introduced in sections 2.4 to 2.6, we can compute any multiparticle correlator with a single passage. Further taking into account that there are other sources of correlations among the particles aside from anisotropic flow we introduce more robust observables in form of cumulants of flow harmonics in section 2.7. These observables manage to suppress the contribution of so-called non-flow while preserving the flow signature. To compute the statistical uncertainty of such high-level observables we will use the Bootstrap method detailed in section 2.8. In sections 2.9 to 2.11 we take all techniques we described and introduce and validate a generic framework for computing observables such as cumulants from arbitrary multiparticle correlators with Q-vectors. Lastly, in section 2.13 we introduce Symmetric Cumulants (SC), which are the main observable in this thesis. Unlike cumulants, which can estimate the value of a flow harmonic, symmetric cumulants estimate the correlations between different flow harmonics and provide further and independent constraints for QGP. The proofs for mathematical statements made in chapter 2 can be found in appendix A.

2.1. Fourier expansion of probability density function of azimuthal angles

The azimuthal angle φ of particles produced in a heavy-ion collision is a random variable whose sample space is on the interval $[0, 2\pi)$. A schematic view of an non-central collision can be seen in fig. 2.1. As it is a periodic quantity we can expand its probability density

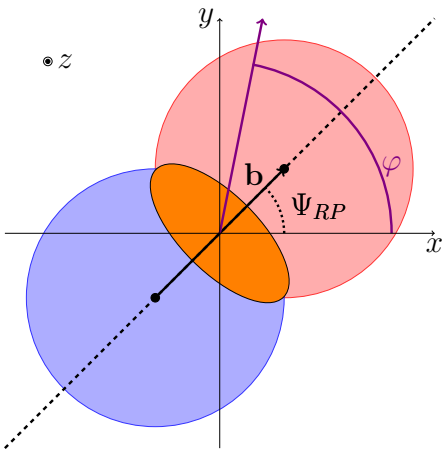

Figure 2.1.: Schematic view of a non-central heavy ion collision in the transverse plane. The azimuthal angle of a produced particle is indicated with a violet arrow and labeled with φ.

function (PDF) in a Fourier series as

$$f(\varphi) = \frac{1}{2\pi}\left[1 + 2\sum_{n=1}^{\infty}\left(c_n \cos(n\varphi) + s_n \sin(n\varphi)\right)\right], \tag{2.1}$$

where

$$c_n = \int_0^{2\pi} \mathrm{d}\varphi f(\varphi)\cos(n\varphi), \tag{2.2}$$

$$s_n = \int_0^{2\pi} \mathrm{d}\varphi f(\varphi)\sin(n\varphi). \tag{2.3}$$

This expansion can be illustrated with a simple example, like the normalized linear function $f(\varphi) = \frac{1}{2\pi^2}\varphi$ on the interval $[0, 2\pi)$. Using eqs. (2.2) and (2.3) the coefficients are

$$c_n = 0 \tag{2.4}$$

and

$$s_n = -\frac{1}{\pi n} \tag{2.5}$$

for $n \in \mathbb{N}$. The Fourier series with the first 10 coefficients can be seen in fig. 2.2. This example highlights some general features of the Fourier Series. Firstly, the expansion actually tends towards the original function using enough coefficients and the coefficients tend to decrease in magnitude with increasing n. In this case we can see from eq. (2.5) that $s_n \propto \frac{1}{n}$. This means in general we are mostly concerned with computing the lowest order coefficients to capture the most important features of the PDF. While the

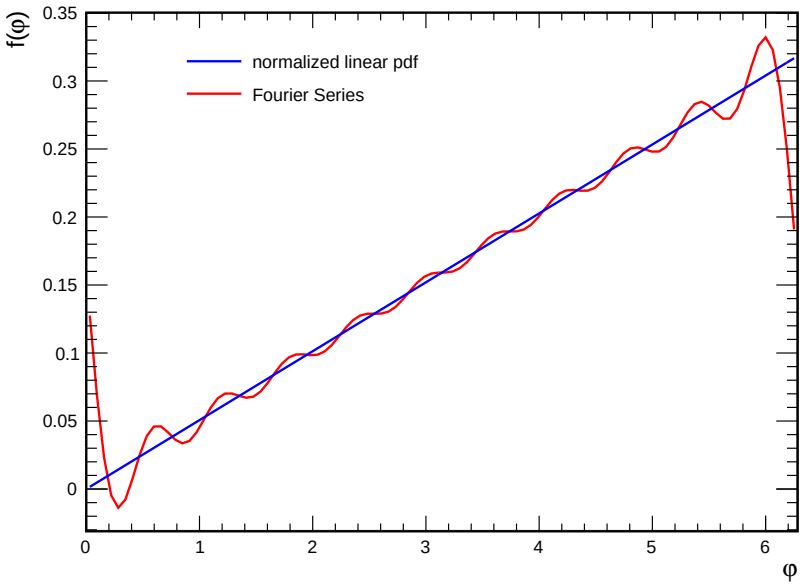

Figure 2.2.: Normalized linear PDF and its Fourier series with the first 10 coefficients.

parameterization of the Fourier series as shown in eq. (2.1) is quite common, it is not the only possible parameterization and not the favored one in anisotropic flow analysis. We will use the following parameterization instead [36]:

$$f(\varphi) = \frac{1}{2\pi}\left[1 + 2\sum_{n=1}^{\infty} v_n \cos[n(\varphi - \Psi_n)]\right], \tag{2.6}$$

where v_n are the anisotropic flow harmonics and Ψ_n are symmetry planes. The relation between the parameters of the previous definition and the new parameters read

$$v_n = \sqrt{c_n^2 + s_n^2} \tag{2.7}$$

and

$$\Psi_n = \frac{1}{n}\arctan\frac{s_n}{c_n}. \tag{2.8}$$

With this decomposition we have a more natural way of thinking about the parameters in terms of amplitudes v_n and phases Ψ_n. It is also possible to define c_n and s_n, as well

as v_n and Ψ_n, with a negative index. Due to the symmetry of the Fourier Series we can establish the following relations

$$c_{-n} = c_n \,, \tag{2.9}$$
$$s_{-n} = -s_n \tag{2.10}$$

and

$$v_{-n} = v_n \,, \tag{2.11}$$
$$\Psi_{-n} = \Psi_n \,, \tag{2.12}$$

which will be needed later. The flow harmonics have unique names depending on their order, in particular

- v_1 is directed flow,
- v_2 is elliptic flow,
- v_3 is triangular flow,
- v_4 is quadrangular flow and so on.

The most interesting harmonic to study is elliptic flow v_2. Due to its low order it carries a lot of information about the PDF and since the initial collision geometry in non-central collisions is to leading order elliptic it is by far the largest harmonic. The directed flow v_1 also contains much information, but it is sensitive to many other processes and it is difficult to disentangle all those contributions.

2.2. Estimation of anisotropic flow harmonics

The PDF of an experimental variable is generally not known and cannot be directly determined by the experiment. Instead, we are estimating flow harmonics by using expectation values, which are essentially averages. To compute the average value of some observable X which is distributed according to some PDF $f(X)$ on some interval $[a, b]$, we need to compute the integral

$$\langle X \rangle = \int_a^b \mathrm{d}X X f(X) \,. \tag{2.13}$$

This can be generalized to functions of the observable, like $g(X)$, which leads to

$$\langle g(X) \rangle = \int_a^b \mathrm{d}X g(X) f(X) \,. \tag{2.14}$$

Our goal is now to use some function $g(\varphi)$ such that we can estimate v_n from computing some average. To this end we make the ansatz

$$g(\varphi) = \cos\left[n\left(\varphi - \Psi_n\right)\right] \tag{2.15}$$

and compute its expectation value. The result reads

$$\left\langle \cos\left[n\left(\varphi - \Psi_n\right)\right]\right\rangle = v_n\,. \tag{2.16}$$

This results gives us the ability to compute flow harmonics for arbitrary n. We can illustrate the validity of this result using a simple Monte Carlo study. Let us assume a PDF expanded as in eq. (2.6), where all harmonics are zero, except $v_2 = 5 \times 10^{-2}$. We generate 10 000 events and sample 1500 particles each, compute $\cos\left[2\left(\varphi - \Psi_2\right)\right]$ and fill the resulting data into a TProfile object[1]. In each event Ψ_2 was given a uniformly random value between 0 and 2π. The result can be seen in fig. 2.3. The main issue with

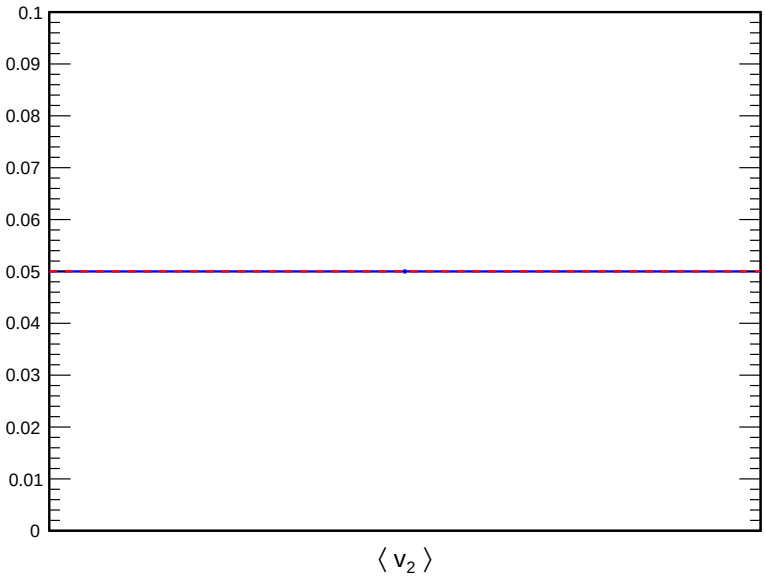

Figure 2.3.: TProfile holding the expectation value of v_2 for 10 000 events with 1500 particles each, computed using eq. (2.16). The expected value of $v_2 = 5 \times 10^{-2}$ is marked with a red line. The mean value over all events is $\langle v_2 \rangle = (4.9997 \pm 0.0182) \times 10^{-2}$.

this type of analysis is that there is generally no reliable way to estimate any Ψ_n for

[1] A TProfile is a class object of the ROOT framework developed for data analysis in high energy physics. It is very similar to a histogram, but instead of counting the number of entries in each bin it carries the mean value of the bin entries in each bin. They are very useful for computing single- and all-event averages.

any event. So we need to find a way to extract flow harmonics from the data without knowing symmetry planes. This can be achieved by utilizing multiparticle correlation techniques.

2.3. Multiparticle correlation techniques

When only collective flow is present, all produced particles are emitted independently to each other, and are correlated only to some common symmetry plane. This implies that the joint PDF for any number of particles will factorize as

$$f(\varphi_1, \ldots, \varphi_n) = f_{\varphi_1}(\varphi_1) \ldots f_{\varphi_n}(\varphi_n)\,, \tag{2.17}$$

where for each φ_i the functional form of the normalized marginalized PDF, $f_{\varphi_i}(\varphi_i)$, is the same and given by a Fourier series as in eq. (2.6). Based on this reasoning, one can build up in principle infinitely many independent azimuthal observables sensitive to various combinations of flow harmonics and corresponding symmetry planes by adding more and more particles to the correlators. Using multiparticle correlation we can now construct correlators that can estimate flow harmonics without having any knowledge about symmetry planes. As an example, we can use a two-particle correlator to estimate v_n with

$$\langle 2 \rangle \equiv \langle \cos\left[n(\varphi_1 - \varphi_2)\right] \rangle\,, \tag{2.18}$$

$$= \sum_{\substack{k,l=0 \\ k \neq l}}^{M} \cos\left[n(\varphi_k - \varphi_l)\right]\,, \tag{2.19}$$

$$= v_n^2\,, \tag{2.20}$$

where M is the number of particles in the event, φ_k is the azimuthal angle with of the kth particle and the condition $k \neq l$ eliminates the trivial but dominate self-correlations. This example shows that we can construct powers of flow harmonics by computing multiparticle correlators. Once again we can illustrate this result using the same Monte Carlo study as in the section 2.1. Let us again assume a PDF expanded as in eq. (2.6), where all harmonics are zero, except $v_2 = 5 \times 10^{-2}$. Now we generate 10 000 events and sample 1500 particles in each event, compute the two-particle correlator $\langle 2 \rangle$ and put the result into a TProfile. In each event Ψ_2 was given a uniformly random value between 0 and 2π. The result can be seen in fig. 2.4.

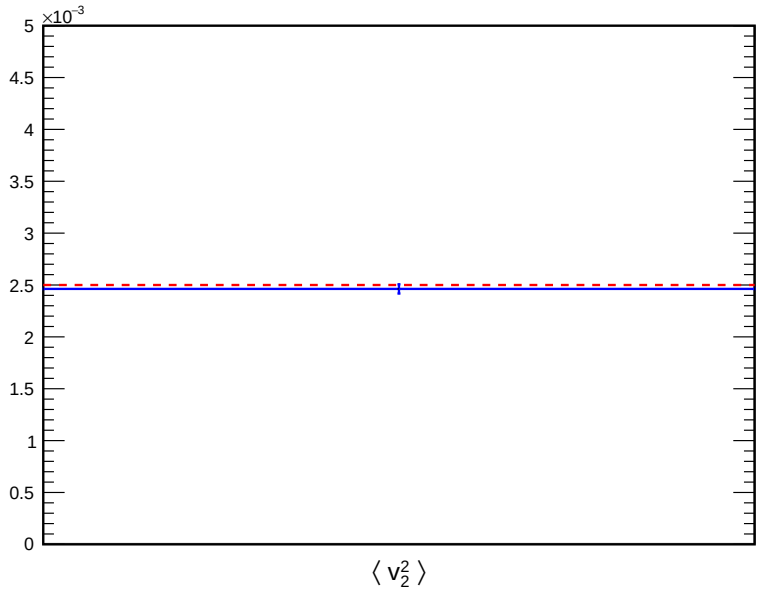

Figure 2.4.: TProfile holding the expectation value of v_2^2 for 10 000 events with 1500 particles each, computed using $\langle 2 \rangle$ with nested loops. The expected value of $v_2^2 = 2.5 \times 10^{-3}$ is marked with a red dashed line. The mean value over all events is $\left\langle v_2^2 \right\rangle = (2.5037 \pm 0.0047) \times 10^{-3}$.

2.4. Q-vector

Multiparticle correlators are a good tool for computing flow harmonics, but they are computationally very expensive. If we were to compute a k particle correlator, we would have to compute an expectation value with k nested loops over all M particles produced in an event. That means the computation time would scale like M^k, which is not feasible. That is why in practice we express multiparticle correlators in terms of Q-vectors. Using Q-vectors to compute multiparticle correlators gives the exact same analytical result as if computing it with a nested loop. A Q-vector evaluated in harmonic n is defined as

$$Q_n = \sum_{k=1}^{M} e^{in\varphi_k} \,, \tag{2.21}$$

where M is the multiplicity. Using this definition we can express the two-particle correlator from before like

$$v_n^2 = \langle \cos\left[n\left(\varphi_1 - \varphi_2\right)\right] \rangle = \frac{1}{\binom{M}{2} 2!} \left(|Q_n|^2 - M \right) \,, \tag{2.22}$$

where Q_n can be computed in only one loop over all M particles. To validate this result, we perform the same Monte Carlo study again as in section 2.3. The result can be seen in fig. 2.5. Both techniques produce the exact same value of v_2^2, namely

$$\left(v_2^{\text{nested loop}}\right)^2 = \left(v_2^{\text{Q-vector}}\right)^2 = 2.5037 \times 10^{-3} \,, \tag{2.23}$$

but using Q-vectors is orders of magnitudes faster. The comparison of the runtime using Q-vectors and a nested loop with only two levels can be seen in table 2.1.

Table 2.1.: Comparison of runtime between nested loops and Q-vectors for v_2^2. The runtime was measured for a computation of 10 000 events with 1500 particles per event. It was tested on a machine equipped with an Intel(R) Core(TM) i5-2520M CPU @ 2.50GHz. Using Q-vectors is roughly 90 times faster.

technique	runtime [s]
nested loop	2167
Q-vector	24

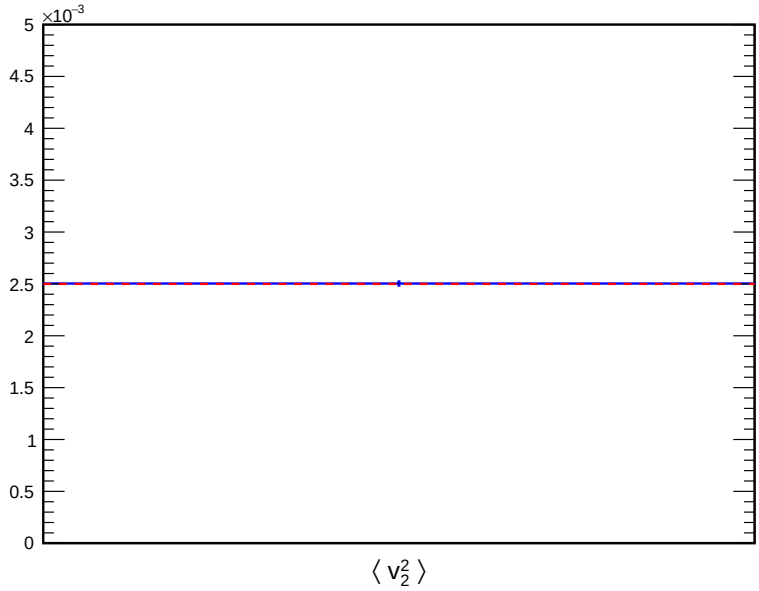

Figure 2.5.: Expectation value of v_2^2 for 10 000 events with 1500 particles each, computed using $\langle 2 \rangle$ with Q-vectors. The expected value of $v_2^2 = 2.5 \times 10^{-3}$ is marked with a red dashed line. The mean value over all events is $\left\langle v_2^2 \right\rangle = (2.5037 \pm 0.0195) \times 10^{-3}$.

2.5. Multiplicity fluctuations

In the Monte Carlo studies used so far we always assumed to have the same multiplicity in each event. This is obviously not the case for real data. While this is not a problem when computing correlators with nested loops, if we use Q-vectors we have to be very careful when computing all-event averages. For the case of a two-particle correlator and using nested loops, we fill $M\,(M-1)$ values into the TProfile for each event, where the multiplicity M fluctuates from event to event. That means if we compute the mean value over all entries, the multiplicity of each event is then taken into account and the correct result is produced. In contrast to using Q-vectors, we compute the Q-vector for each event and just fill this one value into the TProfile. If we were to compute the mean value now, the value would be wrong because all Q-vectors would carry unit weight, even though each Q-vector represents a different number of particles or more precisely, a different number of combinations of particles. To account for this discrepancy, we weight each Q-vector appropriately with its combinatorial weight, which in case of a two-particle correlator is $M\,(M-1)$. This ensures that we get the exact same analytical results as if we were computing the multiparticle correlator using nested loops. We can show the validity of this statement once again with a Monte Carlo study. Let us again assume a PDF expanded as in eq. (2.6), where all harmonics are zero, except $v_2 = 5 \times 10^{-2}$. Now we generate 10 000 events and sample a random number of particles between 500 and 1500 in each event, compute the two-particle correlator and put the result into a TProfile. Additionally, in the case of using Q-vectors, we assign to each event its combinatorial weight depending on the multiplicity. The results can be seen in figs. 2.6 and 2.7. The all-event averages are exactly the same value, namely

$$\left(v_2^{\text{nested loop}}\right)^2 = \left(v_2^{\text{Q-vector}}\right)^2 = 2.5520 \times 10^{-3}\,. \tag{2.24}$$

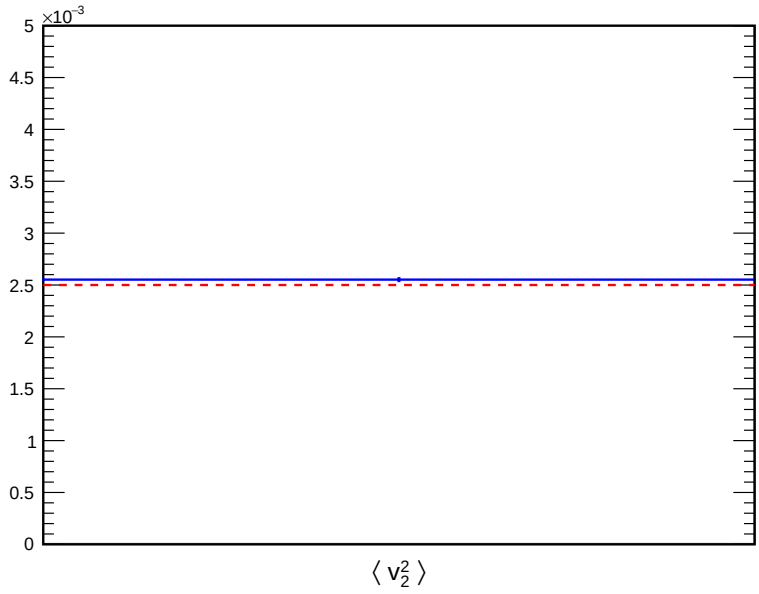

Figure 2.6.: Expectation value of v_2^2 for 10 000 events with a number of particles between 500 and 1500 each, computed using $\langle 2 \rangle$ with nested loops. The expected value of $v_2^2 = 2.5 \times 10^{-3}$ is marked with a red dashed line. The mean value over all events is $\left\langle v_2^2 \right\rangle = (2.5520 \pm 0.0131) \times 10^{-3}$.

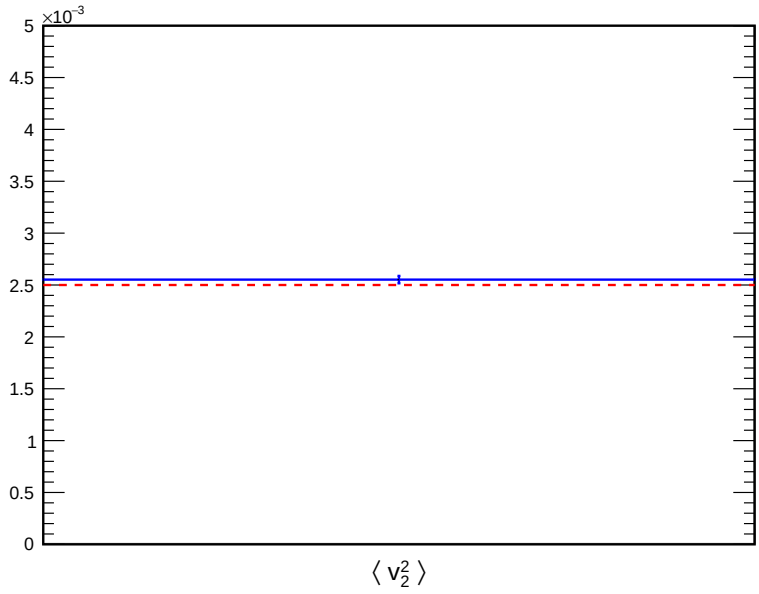

Figure 2.7.: Expectation value of v_2^2 for 10 000 events with a number of particles between 500 and 1500 each, computed using $\langle 2 \rangle$ with Q-vectors. The expected value of $v_2^2 = 2.5 \times 10^{-3}$ is marked with a red dashed line. The mean value over all events is $\left\langle v_2^2 \right\rangle = (2.5520 \pm 0.0357) \times 10^{-3}$.

2.6. Multiparticle correlator

We already introduced why and how we use multiparticle correlation techniques, but in the Monte Carlo studies shown so far we only looked at correlation between two particles. In general, we only refer to multiparticle correlations as such when we study correlations of at least three particles. Therefore, we will now introduce a real multiparticle correlator and verify that the results of the previous sections still hold. The four-particle correlator is defined as

$$\langle 4 \rangle \equiv \langle \cos \left[n \left(\varphi_1 + \varphi_2 - \varphi_3 - \varphi_4 \right) \right] \rangle = v_n^4 \,. \tag{2.25}$$

Using this correlator we can estimate the fourth power of a flow harmonic with arbitrary n. To evaluate this correlator explicitly, we would, as mentioned in section 2.4, have to compute a nested loop with four levels over all events. As this is computationally not feasible, we rewrite this correlator analytically in terms of Q-vectors. The analytic result reads

$$\begin{aligned} \langle 4 \rangle = \frac{1}{\binom{M}{4} 4!} \Big[& |Q_n|^4 + |Q_{2n}|^2 - 2 \operatorname{Re}(Q_{2n} Q_n^* Q_n^*) \\ & -4 \left(M - 2 \right) |Q_n|^2 + 2M \left(M - 3 \right) \Big] \,. \end{aligned} \tag{2.26}$$

Let us again assume a PDF expanded as in eq. (2.6), where all harmonics are zero, except $v_2 = 5 \times 10^{-2}$. Now we generate 10 000 events and sample a random number of particles between 500 and 1500 in each event, compute $\langle 4 \rangle$ and put the result into a TProfile. Additionally, since we are using Q-vectors, we assign to each bin its combinatorial weight depending on the multiplicity, which in this case is $M(M-1)(M-2)(M-3)$. The result can be seen in fig. 2.8. As with the two-particle correlator, the all-event average is close to the expected result.

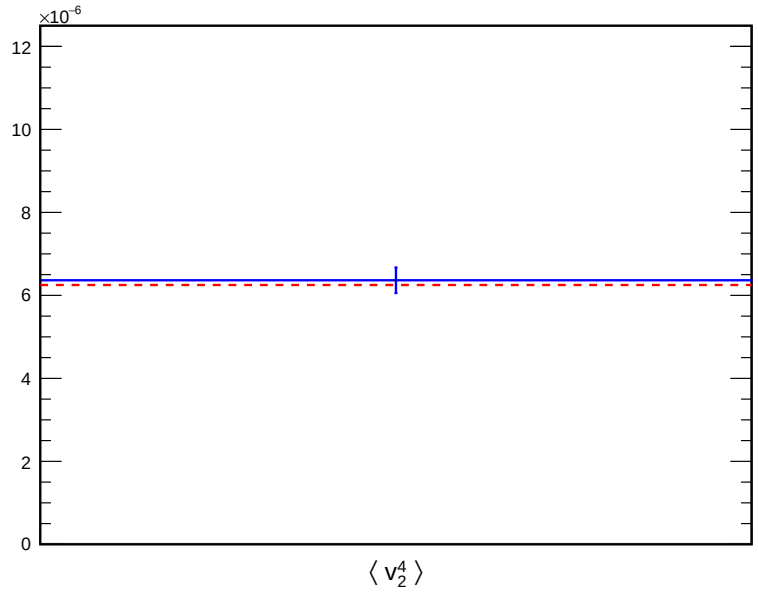

Figure 2.8.: Expectation value of v_2^4 for 10 000 events with a number of particles between 500 and 1500 each, computed using $\langle 4 \rangle$ with Q-vectors. The expected value of $v_2^4 = 6.25 \times 10^{-6}$ is marked with a red dashed line. The mean value over all events is $\left\langle v_2^4 \right\rangle = (6.3640 \pm 0.3074) \times 10^{-6}$.

2.7. Cumulants

All machinery developed thus far has relied on the assumption that eq. (2.17) holds, which has been the case for the Monte Carlo studies performed until now. However, in a real experiment we expect to have correlations between subsets of particles, for example due to interactions, resonance decays, jets, detector artifacts and so on. All these sources of correlations among only a subset of particles are typically called non-flow. Any non-flow contribution spoils the equality in eq. (2.17), which in turn spoils all the methods we developed so far for analyzing data of real experiments. This means we have to use new observables which are sensitive to flow and less sensitive to non-flow. Before we introduce these observables, lets us first have a look at how the contribution of non-flow would scale to a k-particle correlator $\langle k \rangle$. Assume we have an event in which $M \gg k$ particles are produced and non-flow is present in form of a single jet or resonance decay, correlating k particles. If we were to compute the non-flow contribution δ_k to $\langle k \rangle$ it would scale like

$$\delta_k \sim \frac{k-1}{M-1} \cdot \frac{k-2}{M-2} \cdot \ldots \cdot \frac{1}{M-(k-1)} \approx \frac{1}{M^{k-1}}\,, \tag{2.27}$$

because the probability of picking particles which are part of the jet or decay is the fraction between the number of particles left to pick for the k-particle correlator and all other particles left in the whole event. On the other hand if more than k particles are correlated due to non-flow it would scale like

$$\delta_k \sim \frac{k}{M-1} \cdot \frac{k-1}{M-2} \cdot \ldots \cdot \frac{2}{M-(k-1)} \approx \frac{1}{M^{k-1}}\,, \tag{2.28}$$

using the same argument as for eq. (2.28). This means we expect the contribution δ_k of non-flow to $\langle k \rangle$ to scale like

$$\delta_k \sim \frac{1}{M^{k-1}}\,, \tag{2.29}$$

telling us, that the scaling of the non-flow contribution is only determined by the order of the multiparticle correlator, which is equal to k. This argument also holds if less than k particles are correlated. In fig. 2.9 this principle is demonstrated for a 4-particle correlator. In contrast, the contribution of flow δ_k^{flow} to $\langle k \rangle$ scales like

$$\delta_k^{flow} \sim \frac{M-1}{M-1} \cdot \frac{M-2}{M-2} \cdot \ldots \cdot \frac{M-(k-1)}{M-(k-1)} \approx 1\,, \tag{2.30}$$

because flow is a collective effect, we will always pick another particle which is correlated to the first one due to flow. This means, in general multiparticle correlators have both non-flow and flow contribution, which can be schematically written as

$$\langle k \rangle \simeq \delta_k + \delta_k^{flow} + \cdots\,, \tag{2.31}$$

$$\simeq \frac{1}{M^{k-1}} + v^k + \cdots\,, \tag{2.32}$$

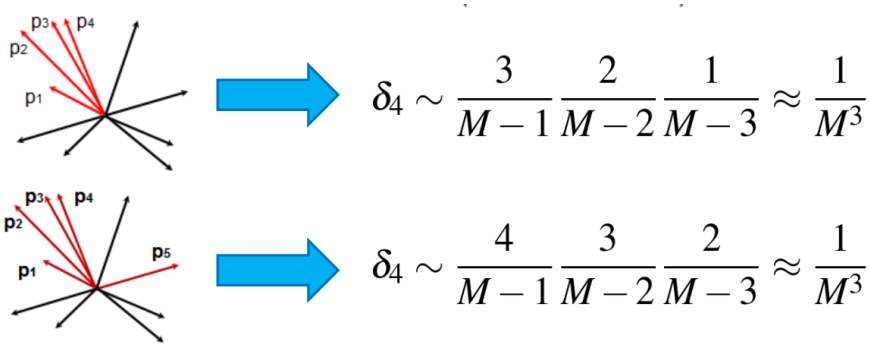

Figure 2.9.: Example of how the non-flow contribution scales for a 4-particle correlator. In the top part of the figure, particle $p_1, \ldots, p_4$ are correlated by non-flow. In the bottom part of the figure, particles $p_1, \ldots, p_5$ are correlated by non-flow. As we can see in both cases the non-flow contribution scales as $\frac{1}{M^3}$, only depending on the order of the correlator.

where we used the scaling of δ_k and that we can rewrite δ_k^{flow} as the kth power of some flow harmonic v_n. The key question is how can we isolate the genuine k-particle correlation from the measured k-particle correlator. For this purpose we use cumulants. Cumulants are objects which quantify the genuine correlation between stochastic variables as a function of moments. To illustrate this, let us look at the most general decomposition of a joint p.d.f of two random variables X_1 and X_2, namely

$$f(X_1, X_2) = f_{X_1}(X_1) f_{X_2}(X_2) + f_c(X_1, X_2) , \tag{2.33}$$

where the product of the marginal PDF of X_1 and X_2 parameterize their independence of each other and f_c the genuine correlation. This decomposition can not be done in general, but if we compute the expectation values on both sides, we receive

$$\langle X_1 X_2 \rangle = \langle X_1 \rangle \langle X_2 \rangle + \langle X_1 X_2 \rangle_c , \tag{2.34}$$

where $\langle X_1 X_2 \rangle_c$ is by definition a 2-particle cumulant. Since we cannot measure cumulants directly, but we can measure moments, we invert this relation to

$$\langle X_1 X_2 \rangle_c = \langle X_1 X_2 \rangle - \langle X_1 \rangle \langle X_2 \rangle , \tag{2.35}$$

which describes the 2-particle cumulant as a function of moments. This is also true for any higher order cumulant. Now, we want to derive an expression which lets us compute some flow harmonic v_n as a function of a 2-particle cumulant. For this purpose we choose our stochastic variables to be $X_1 = e^{in\varphi_1}$ and $X_2 = e^{-in\varphi_2}$ respectively[2]. Plugging this into eq. (2.35) and performing averages not only over one event, but many events, results

[2] In the appendix A.6 we showed that $\left\langle \left\langle e^{in(\varphi_1 - \varphi_2)} \right\rangle \right\rangle$ and $\langle \langle \cos[n(\varphi_1 - \varphi_2)] \rangle \rangle$ give the same result, so they can be used interchangeably.

in

$$c_n\{2\} \equiv \left\langle\left\langle e^{in(\varphi_1-\varphi_2)}\right\rangle_c\right\rangle = \left\langle\left\langle e^{in(\varphi_1-\varphi_2)}\right\rangle\right\rangle - \underbrace{\left\langle\left\langle e^{in\varphi_1}\right\rangle\right\rangle}_{=0}\underbrace{\left\langle\left\langle e^{-in\varphi_2}\right\rangle\right\rangle}_{=0}, \tag{2.36}$$

$$= \langle\langle 2\rangle\rangle\ , \tag{2.37}$$

$$= \left\langle v_n^2\right\rangle \equiv \left(v_n\{2\}\right)^2\ , \tag{2.38}$$

where we adopted the notation $c_n\{2\}$ for the 2-particle cumulant, $v_n\{2\}$ for the flow harmonic v_n estimated by a 2-particle cumulant and used eq. (2.20) to rewrite the 2-particle correlator as the square of v_n. The double angle bracket notation means that at first we take the average with respect to data belonging to only one event and afterwards averaging the results over all events in the data set. This is also the reason why the expectation values computed over a single azimuthal angle evaluate to 0. Averaging over a single event gives a term whose real part is proportional to the cosine and whose imaginary part is proportional to the sine of the symmetry plane Ψ. Since the symmetry planes are uniformly randomly distributed between 0 and 2π, the average over the cosine and sine vanish. Using this formalism analogously for the 4-particle case, where we set $X_1 = e^{in\varphi_1}$, $X_2 = e^{in\varphi_2}$, $X_3 = e^{-in\varphi_3}$ and $X_4 = e^{-in\varphi_4}$, we arrive at

$$c_n\{4\} \equiv \left\langle\left\langle e^{in(\varphi_1+\varphi_2-\varphi_3-\varphi_4)}\right\rangle_c\right\rangle = \langle\langle 4\rangle\rangle - 2\langle\langle 2\rangle\rangle^2\ , \tag{2.39}$$

$$= \left\langle v_n^4\right\rangle - 2\left\langle v_n^2\right\rangle^2\ , \tag{2.40}$$

$$\equiv -\left(v_n\{4\}\right)^4\ , \tag{2.41}$$

where we introduced the same notation as before and used additionally eq. (2.25) to evaluate the 4-particle correlator. Finally, using these relations, we introduce our main observables, namely $v_n\{2\}$ and $v_n\{4\}$, which are harmonics v_n estimated via 2- and 4-particle cumulants, respectively. Inverting the previous results, they are defined as

$$v_n\{2\} = \sqrt{c_n\{2\}}\,, \tag{2.42}$$

$$v_n\{4\} = \sqrt[4]{-c_n\{4\}}\,. \tag{2.43}$$

Using these equation and expanding the RHS in terms of Q-vectors gives so-called Q-cumulants (QC). As we discussed before, evaluating multiparticle correlators explicitly is in general not feasible, so going forward all cumulants will be computed using Q-vectors, even though we may not refer to them explicitly as QCs. These results can also be verified with a Monte Carlo study. Let us assume a PDF expanded as in eq. (2.6), where all harmonics are zero, except $v_2 = 5 \times 10^{-2}$. We generate 10 000 events and sample a random number of particles between 500 and 1500 in each event, compute the 2- and 4-particle correlator using Q-vectors, average over all events and use eq. (2.42) to compute $v_2\{2\}$ and $v_2\{4\}$. The results read

$$v_2\{2\} = (5.0517 \pm 0.0373) \times 10^{-2}\,, \tag{2.44}$$

$$v_2\{4\} = (5.0802 \pm 0.2635) \times 10^{-2}\,. \tag{2.45}$$

The result for $v_2\{2\}$ is very close to the theoretical value of $v_2 = 5 \times 10^{-2}$ while $v_n\{4\}$ differs a bit more. That is due to the fact that for $v_n\{4\}$ we need to compute correlators of a higher order than for $v_n\{2\}$. The higher the order of the correlators, the more statistics are needed for a numerically stable result. Since both cumulants were computed on the same data set, this explains why $v_2\{2\}$ gives a more accurate results than $v_2\{4\}$. Nevertheless, $v_n\{4\}$ suppresses non-flow correlations better than $v_n\{2\}$ and is therefore the preferred observable for analyzing real data. The statistical uncertainties of both quantities were computed using the Bootstrap method, which will be introduced in the following.

2.8. Bootstrap

Normally, we use error propagation to compute the statistical uncertainties of compound observables, like for example $v_n\{4\}$. However, this becomes intractable for complicated compound observables, like for example $v_n\{4\}$. As a substitute we will use a simplified Bootstrap method which is endorsed by the ALICE collaboration. The Bootstrap method is performed using the following 3-step process. Firstly, we divide the initial data set into 10 subsamples such that they have roughly the same statistics. Secondly, for the whole dataset we compute the mean μ and for each subsample we compute the mean μ_i of the observable of interest. We can use these values to compute the unbiased variance

$$\sigma^2 = \frac{1}{10-1} \sum_{k=1}^{10} (\mu - \mu_k)^2 \ . \tag{2.46}$$

Thirdly, the uncertainty of μ can then be computed with

$$\Delta\mu = \sqrt{\frac{\sigma^2}{10}} \tag{2.47}$$

and we can report observable μ with statistical uncertainties as $\mu \pm \Delta\mu$.

2.9. Particle weights

While great efforts have been put into the development and production of the detectors used in high energy physics, they are still imperfect. These imperfections cause systematic biases in our computed observables. One example would be if the detector does not have uniform acceptance over certain ranges of kinematic variables, like azimuthal angle φ, transverse momentum p_{T} or pseudorapidity η. But if we know about these beforehand[3],

[3] Detectors inefficiencies can be obtained either by measuring the detector response to known sources or through Monte Carlo simulations.

we can correct for them during the analysis to remove the systematic bias from our result. Therefore, we introduce particle weights

$$w_k = w_k\left(\varphi, p_\mathrm{T}, \eta, \ldots\right) , \tag{2.48}$$

for each particle k which are functions of any particle attribute which can influence the detector response. Note that we associate one weight to one particle, meaning we assume the weights to independent of each other. Moreover, we assume that each particle attribute influences the detector independently of the others and we can factorize the functional dependence of the weights like

$$w_k(\varphi, p_\mathrm{T}, \eta, \ldots) = w_{k,\varphi}(\varphi) \cdot w_{k,p_T}(p_\mathrm{T}) \cdot w_{k,\eta}(\eta) \cdots . \tag{2.49}$$

These weights enter the calculation of correlators when we replace the simple averages we used before, like for example in eq. (2.20), and use a weighted sum instead. The formula for computing a 2-particle correlator of an event with multiplicity M with correction for detector inefficiencies now reads

$$\langle 2 \rangle = \langle \cos\left[n\left(\varphi_1 - \varphi_2\right)\right] \rangle \tag{2.50}$$

$$= \frac{\sum\limits_{\substack{k,l=1 \\ k\neq l}}^{M} w_k w_l \cos\left[n\left(\varphi_k - \varphi_l\right)\right]}{\sum\limits_{\substack{k,l=1 \\ k\neq l}}^{M} w_k w_l} \tag{2.51}$$

$$= v_n^2 . \tag{2.52}$$

Assuming we have a perfect detector, i.e. setting all weights $w_k = w_l = 1$, we get our previous result, eq. (2.20), back. However, as it is written above, we perform a nested loop over all particles which is, as we discussed before, computationally not feasible for a large number of particles. This means we have to incorporate particle weights in the computation of Q-vectors. It is just as straight forward as above. We simply need to replace the normal sum, as shown in eq. (2.21), with a weighted sum and receive

$$Q_n = \sum_{k=1}^{M} w_k e^{in\varphi_k} . \tag{2.53}$$

This definition will be further generalized in eq. (2.71), but it is sufficient for the Monte Carlo study in this section. Using it we can rewrite the expression for a 2-particle correlator with Q-vectors as

$$\langle 2 \rangle = \frac{1}{\sum\limits_{\substack{k,l=1 \\ k\neq l}}^{M} w_k w_l} \left(|Q_n|^2 - \sum_{k=1}^{M} w_k^2 \right) . \tag{2.54}$$

Take note of the prefactor. As we discussed in section 2.5, if we want to average correlators of events whose multiplicity is fluctuating we need to assign it a combinatorial weight. In the absence of systematic biases this combinatorial would simply be the number of possible combinations of particles, here $M(M-1)$. Instead we now have to sum the particle weights over all possible combinations of particles which is given by

$$\sum_{\substack{k,l=1 \\ k\neq l}}^{M} w_k w_l \,. \tag{2.55}$$

2.9.1. Monte Carlo study with φ-weights

In this study we will verify the results in the case of a detector which does not uniformly accept azimuthal angles φ. More specifically, we assume that angles $\varphi \in \left[\frac{2\pi}{6}, \frac{2\pi}{3}\right]$ are accepted with a probability of only 60 %. A possible response of such a detector to uniformly randomly emitted particles can be seen in the histogram in fig. 2.10. Using

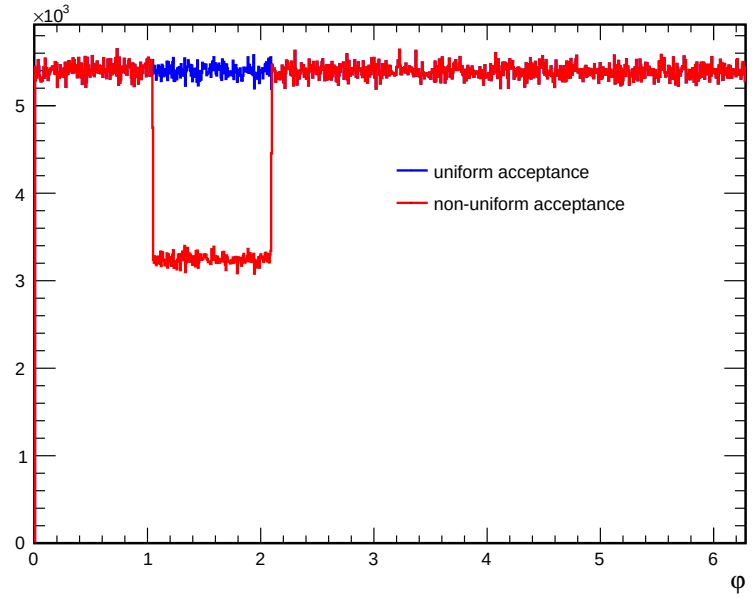

Figure 2.10.: Response of a detector which has uniform azimuthal acceptance in blue and reduced acceptance for azimuthal angles $\varphi \in \left[\frac{2\pi}{6}, \frac{2\pi}{3}\right]$ of 60 % in red to uniformly randomly emitted particles.

this spectrum we can construct particle weights w as a function of φ by inverting the bin content in each bin of the histogram shown in fig. 2.10. Note that due to the way we defined the weighted sum in eq. (2.51) and eq. (2.54) we can trivially scale all our weights

without changing the results. A good choice to make sure that the weights are of the order $\mathcal{O}(1)$ is to scale them with the average number of particles per bin. The resulting weights can be seen in fig. 2.11. Now, let us assume a PDF expanded as in eq. (2.6),

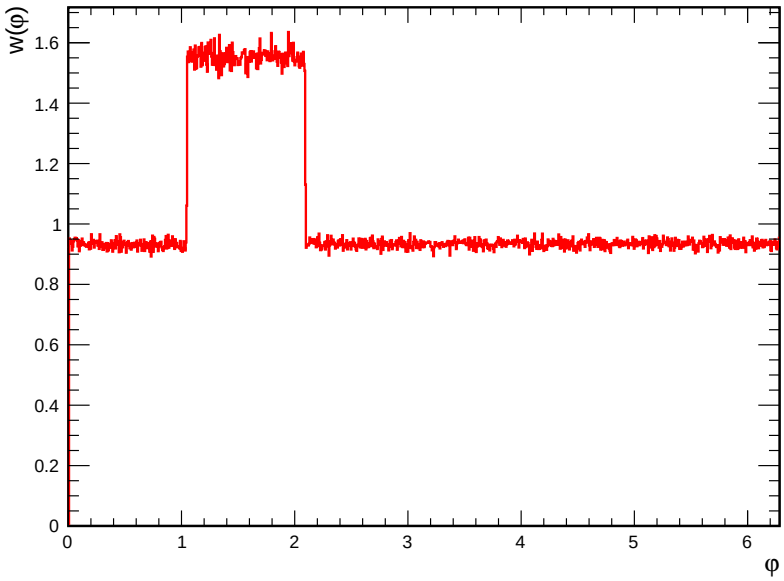

Figure 2.11.: Particle weights to remove systematic biases introduced by a detector with reduced acceptance for azimuthal angles $\varphi \in \left[\frac{2\pi}{6}, \frac{2\pi}{3}\right]$ of 60 %.

where all harmonics are zero, except $v_2 = 5 \times 10^{-2}$. We generate 10 000 events, sample a random number of particles between 500 and 1500 in each event and compute the two-particle correlator using Q-vectors. We will do this twice, once including the weights and once without them. Then we average over all events and obtain our result, which can be seen in fig. 2.12. As we can see, with weights we are able to correct for the systematic biases induced by an imperfect detectors with non-uniform azimuthal acceptance and we obtain the correct result for the correlator.

2.9.2. Monte Carlo study with p_{T}-weights

In this study we will verify the results in the case of a detector which does not uniformly accept transverse momentum p_{T}. This is more involved than the previous study since the distribution of the transverse momentum of the particles is not flat but a Boltzmann distribution. The p_{T}-distribution can be parameterized with

$$f_{p_{\mathrm{T}}}(p_{\mathrm{T}}) = \mathcal{N} p_{\mathrm{T}} \exp\left(\frac{-\sqrt{p_{\mathrm{T}}^2 + m^2}}{T}\right), \tag{2.56}$$

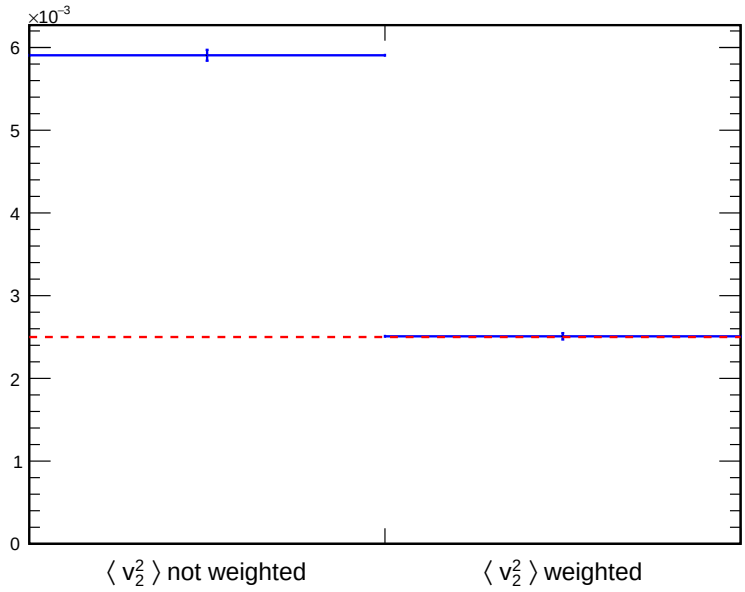

Figure 2.12.: Expectation value of v_2^2 for 10 000 events with a number of particles between 500 and 1500 each, using a biased detector and computed using $\langle 2 \rangle$ with Q-vectors. The expected value of $v_2^2 = 2.5 \times 10^{-3}$ is marked with a red dashed line. The mean value over all events, without weights, is $\left\langle v_2^2 \right\rangle = (5.9059 \pm 0.0065) \times 10^{-3}$ and with weights is $\left\langle v_2^2 \right\rangle = (2.5085 \pm 0.0038) \times 10^{-3}$.

where we set $\mathcal{N}$ such that the distribution is normalized, $m = 0.139\,\text{GeV}$ the mass of the charged pion and $T = 0.44\,\text{GeV}$. Choosing a higher value for T would shift the peak of the distribution to higher values of p_T. Assuming the detector accepts transverse momentum $p_\text{T} \in [0.4, 1.2]$ with a probability of only 60 % we will receive a detector response as shown in fig. 2.13. The weights can be computed by taking the bin-by-bin ratio between the

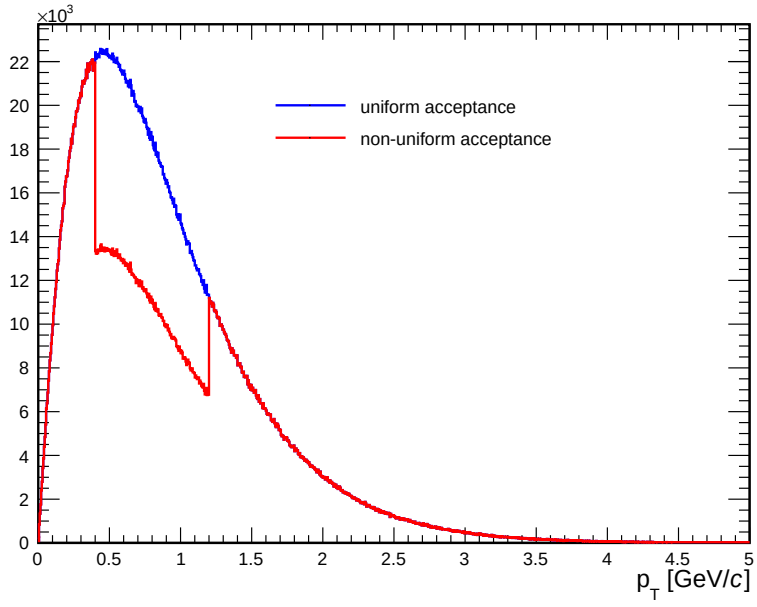

Figure 2.13.: Response of a detector which has uniform transverse momentum acceptance in blue and reduced acceptance for transverse momentum $p_\text{T} \in [0.40, 1.2]$ of 60 % in red to randomly emitted particles following eq. (2.56).

two histograms shown in fig. 2.13. The result can be seen in fig. 2.14. Additionally, in this study we will also let the flow harmonics be a function of transverse momentum. In particular we will let v_2 be a function of p_T as given by

$$v_2(p_\text{T}) = v_{2,max} \cdot \begin{cases} \frac{p_\text{T}}{p_C} & \text{for } p_\text{T} < p_C \\ 1 & \text{for } p_\text{T} \geq p_C \end{cases}, \tag{2.57}$$

where we set $v_{2,max} = 0.30$ and the cutoff momentum $p_C = 2.0\,\text{GeV}$. Using these parameters we can compute the expectation value

$$\langle v_2 \rangle = 1.6787 \times 10^{-2}\,, \tag{2.58}$$

with respect to transverse momentum. Now, let us assume a PDF expanded as in eq. (2.6), where all harmonics are zero, except v_2 which is given by eq. (2.57). We generate 10 000 events, sample a random number of particles between 500 and 1500 in each event and compute the two-particle correlator using Q-vectors. We will do this twice, once including

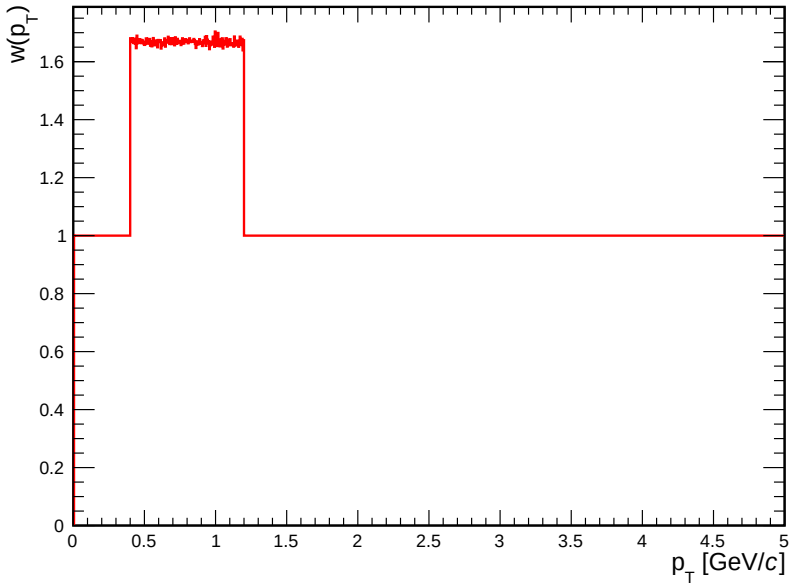

Figure 2.14.: Particle weights to remove systematic biases introduced by a detector with reduced acceptance for transverse momentum $p_{\mathrm{T}} \in [0.40, 1.2]$ of 60 %.

the weights and once without them. Then we average over all events and obtain our result, which can be seen in fig. 2.12. We see again with weights we are able to correct for the systematic biases induced by an imperfect detectors, in this case with non-uniform acceptance of transverse momentum and obtain the correct result for the correlator.

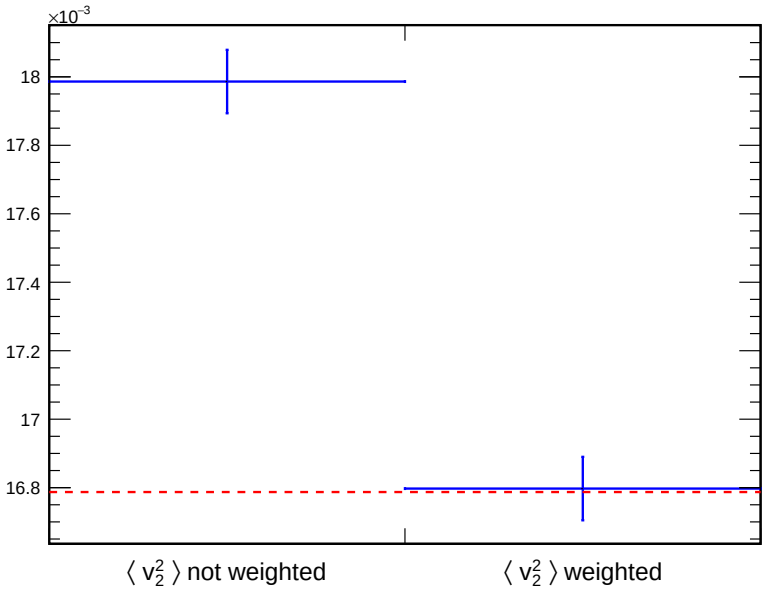

Figure 2.15.: Expectation value of v_2^2 for 10 000 events with a number of particles between 500 and 1500 each, using a biased detector and computed using $\langle 2 \rangle$ with Q-vectors. The expected value of $v_2^2 = 1.6787 \times 10^{-2}$ is marked with a red dashed line. The mean value over all events, without weights, is $\left\langle v_2^2 \right\rangle = (1.7986 \pm 0.0093) \times 10^{-2}$ and with weights is $\left\langle v_2^2 \right\rangle = (1.6813 \pm 0.0082) \times 10^{-2}$.

2.10. Binned multiparticle correlator

So far we have used all particles created within an event to compute multiparticle correlators, which is equivalent to computing the integrated value of the correlator with respect to all attributes of a particle, like p_{T}. This is subsequently also true for the corresponding flow harmonic. But, as we have assumed in the last section, the flow harmonics can in principle be also function of particle attributes. In this section we want to outline how to compute multiparticle correlators more differentially, as functions of these attributes. The idea is very simple. Instead of grouping all particles together for the computation of a correlator, we group the particles into bins of the particle attribute of interest. Then we compute the correlators for each bin individually and perform the all-event average individually for each bin. We will demonstrate the validity with a Toy Monte Carlo study. Let us assume a PDF expanded as in eq. (2.6), where all harmonics are zero, except for $v_2(p_{\mathrm{T}})$. The functional dependence of v_2 on p_{T} will the same as the one given by eq. (2.57). For the study the chosen p_{T} bins are shown in table 2.2. The choice for these

Table 2.2.: p_{T}-bins for Toy Monte Carlo study of a binned multiparticle correlator.

	bins
p_{T} [GeV/c]	$(0.20; 0.50)$, $(0.34; 0.50)$, $(0.50; 0.70)$, $(0.70; 1.0)$, $(1.0; 2.0)$, $(2.0; 5.0)$

bins is inspired by the choice for the real analysis. The transverse momentum of the particles will be distributed according to eq. (2.56). We generate 10 000 events, sample a random number of particles between 500 and 1500 in each event and group them with respect to their transverse momentum in the above defined bins. Then we compute the two-particle correlator using Q-vectors in each bin separately. Then we average over all events in each p_{T}-bin and obtain our result, which can be seen in fig. 2.16. As we can see we are able to resolve v_2^2 as a function of p_{T} very precisely.

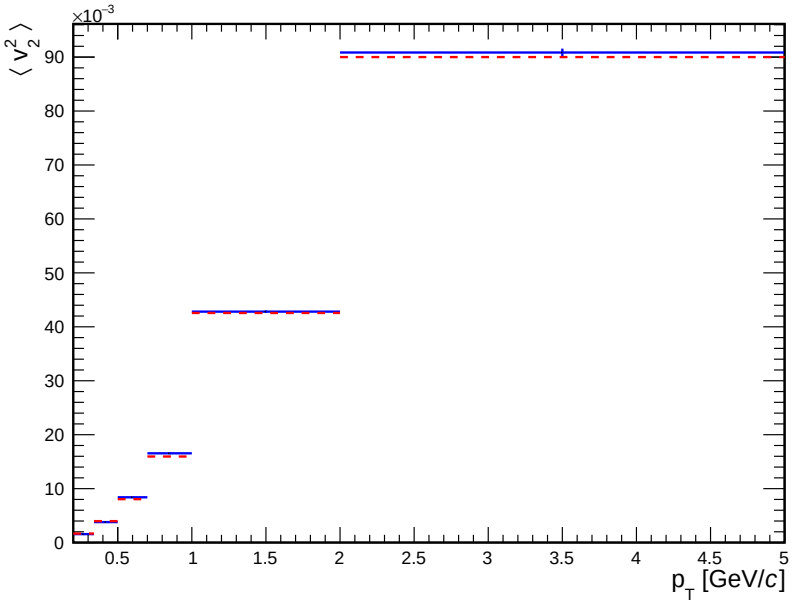

Figure 2.16.: Expectation value of v_2^2 as a function of p_T for 10 000 events with a number of particles between 500 and 1500 each. The theory values are marked with a red line in each bin. The computed estimates in each bin are marked with a blue line.

2.11. Generic framework

Now that we have introduced all necessary components to conduct anisotropic flow analysis on real data, we will introduce a generic framework to compute arbitrary multiparticle correlators. We define an arbitrary multiparticle correlator of an event with multiplicity M as

$$\langle m \rangle_{n_1,n_2,\ldots,n_m} \equiv \left\langle e^{i(n_1\varphi_1+n_2\varphi_2+\cdots+n_m\varphi_m)} \right\rangle \tag{2.59}$$

$$\equiv \frac{\sum\limits_{\substack{k_1,k_2,\ldots,k_m=1 \\ k_1\neq k_2\neq\cdots\neq k_m}}^{M} w_{k_1} w_{k_2} \cdots w_{k_m} e^{i\left(n_1\varphi_{k_1}+n_2\varphi_{k_2}+\cdots+n_m\varphi_{k_m}\right)}}{\sum\limits_{\substack{k_1,k_2,\ldots,k_m=1 \\ k_1\neq k_2\neq\cdots\neq k_m}}^{M} w_{k_1} w_{k_2} \cdots w_{k_m}}\,, \tag{2.60}$$

(2.61)

where $\langle m \rangle$ is a m-particle correlator, φ_{k_i} is the azimuthal angle of the k_ith particle, w_{k_i} is the weight of the k_ith particle and $n_1, n_2 \ldots, n_m \in \mathbb{Z}$ are the m flow amplitudes we want to extract. Note that we already have shown that $v_{-n} = v_n$ so it is perfectly reasonable to choose negative harmonics. Using this definition we can see the correlators we used so far would be expressed in this notation as $\langle 2 \rangle \equiv \langle 2 \rangle_{n,-n}$ and $\langle 4 \rangle \equiv \langle 4 \rangle_{n,n,-n,-n}$. The expectation value of a multiparticle correlator can also be computed analytically which results in

$$\langle m \rangle_{n_1,n_2,\ldots,n_m} \equiv \left\langle e^{i(n_1\varphi_1+n_2\varphi_2+\cdots+n_m\varphi_m)} \right\rangle\,, \tag{2.62}$$

$$= v_{n_1} v_{n_2} \cdots v_{n_m} e^{i(n_1\Psi_1+n_2\Psi_2+\cdots+n_m\Psi_m)}\,, \tag{2.63}$$

where $v_{n_1}, v_{n_2} \ldots, v_{n_m}$ are the flow harmonics and $\Psi_1, \Psi_2, \ldots, \Psi_m$ are the symmetry planes. Since we do not have any means to estimate the symmetry plane Ψ for a single event we need to make their contribution to the above equation disappear. We already argued that the joint PDF of all produced particles factorizes as seen in eq. (2.17). This means, if we enforce the condition

$$\sum_{k=1}^{m} n_k = 0\,, \tag{2.64}$$

then the contribution of the symmetry planes drop out. If we further average over multiple events we arrive at the final expression

$$\left\langle \langle m \rangle_{n_1,n_2,\ldots,n_m} \right\rangle = \left\langle v_{n_1} v_{n_2} \cdots v_{n_m} \right\rangle\,, \tag{2.65}$$

where the inner bracket is with respect to an event average and the outer bracket is with respect to an average over multiple events. We already explicitly demonstrated the validity for the cases of

$$\left\langle \langle 2 \rangle_{-2,2} \right\rangle = \left\langle v_2^2 \right\rangle \tag{2.66}$$

and

$$\left\langle \langle 4 \rangle_{-2,-2,2,2} \right\rangle = \left\langle v_2^4 \right\rangle \tag{2.67}$$

in previous Monte Carlo studies of sections 2.3 and 2.6. The final step is now to express an arbitrary multiparticle correlator in terms of Q-vectors. Therefore, we rewrite eq. (2.60) as

$$\langle m \rangle_{n_1,n_2,\ldots,n_m} = \frac{N \langle m \rangle_{n_1,n_2,\ldots,n_m}}{D \langle m \rangle_{n_1,n_2,\ldots,n_m}} , \tag{2.68}$$

where the numerator is given by

$$N \langle m \rangle_{n_1,n_2,\ldots,n_m} = \sum_{\substack{k_1,k_2,\ldots,k_m=1 \\ k_1 \neq k_2 \neq \cdots \neq k_m}}^{M} w_{k_1} w_{k_2} \cdots w_{k_m} e^{i(n_1\varphi_n + n_2\varphi_2 + \cdots + n_m\varphi_m)} \tag{2.69}$$

and the denominator is given by

$$D \langle m \rangle_{n_1,n_2,\ldots,n_m} = \sum_{\substack{k_1,k_2,\ldots,k_m=1 \\ k_1 \neq k_2 \neq \cdots \neq k_m}}^{M} w_{k_1} w_{k_2} \cdots w_{k_m} . \tag{2.70}$$

We see that $D \langle m \rangle_{n_1,n_2,\ldots,n_m} = N \langle m \rangle_{0,0,\ldots,0}$, so we will only focus on the computation of the numerator. But before we can express it in terms of Q-vectors, we have to slightly modify our definition of a Q-vector as given by eq. (2.54). We will give the Q-vector another index and define it as

$$Q_{n,p} = \sum_{k=1}^{M} w_k^p e^{in\varphi_k} , \tag{2.71}$$

where the weights w_k are raised to the power of the additional index p. Using this new definition we can compute a two-particle correlator $\langle 2 \rangle_{n_1,n_2}$ in a fully generic way while using Q-vectors with

$$N \langle 2 \rangle_{n_1,n_2} = Q_{n_1,1} Q_{n_2,1} - Q_{n_1+n_2,2} \tag{2.72}$$

and

$$D \langle 2 \rangle_{n_1,n_2} = N \langle 2 \rangle_{0,0} = Q_{0,1}^2 - Q_{0,2} . \tag{2.73}$$

A fully generic algorithm for computing arbitrary multiparticle correlators with Q-vectors can be found in [4]. This concludes the introduction of the generic framework. Lastly, we want to validate the outlined framework for arbitrary multiparticle correlators with a Monte Carlo study similar to the one performed in the aforementioned reference. Let us again assume a PDF expanded as in eq. (2.6), where all harmonics are zero, except v_1 up to v_6. We assign values to the flow harmonics with

$$v_n = 0.04 + n \cdot 0.01 \tag{2.74}$$

for $n = 1, 2, \ldots 6$. We will compute the values of the following correlators

$$\langle 2 \rangle \equiv \langle 2 \rangle_{-2,2} = v_2^2 = 3.6 \times 10^{-3}\,, \tag{2.75}$$

$$\langle 3 \rangle \equiv \langle 3 \rangle_{-5,-1,6} = v_1 v_5 v_6 = 4.5 \times 10^{-4}\,, \tag{2.76}$$

$$\langle 4 \rangle \equiv \langle 4 \rangle_{-3,-2,2,3} = v_2^2 v_3^3 = 1.764 \times 10^{-5}\,, \tag{2.77}$$

$$\langle 5 \rangle \equiv \langle 5 \rangle_{-5,-4,3,3,3} = v_3^3 v_4 v_5 = 2.4696 \times 10^{-6}\,, \tag{2.78}$$

$$\langle 6 \rangle \equiv \langle 6 \rangle_{-2,-2,-1,-1,3,3} = v_1^2 v_2^2 v_3^2 = 4.41 \times 10^{-8}\,, \tag{2.79}$$

$$\langle 7 \rangle \equiv \langle 7 \rangle_{-6,-5,-1,1,2,3,6} = v_1^2 v_2 v_3 v_5 v_6^2 = 9.45 \times 10^{-9}\,, \tag{2.80}$$

$$\langle 8 \rangle \equiv \langle 8 \rangle_{-6,-6,-5,2,3,3,4,5} = v_2 v_3^2 v_4 v_5^2 v_6^2 = 1.905\,12 \times 10^{-9}\,, \tag{2.81}$$

which have been randomly chosen with the condition that the harmonics fulfill eq. (2.64). Now we generate 10 000 events and sample a random number of particles between 500 and 1500 in each event. Moreover, we assume our detector has the same reduced acceptance for azimuthal angles as discussed in section 2.9. The results can be seen in fig. 2.17. As

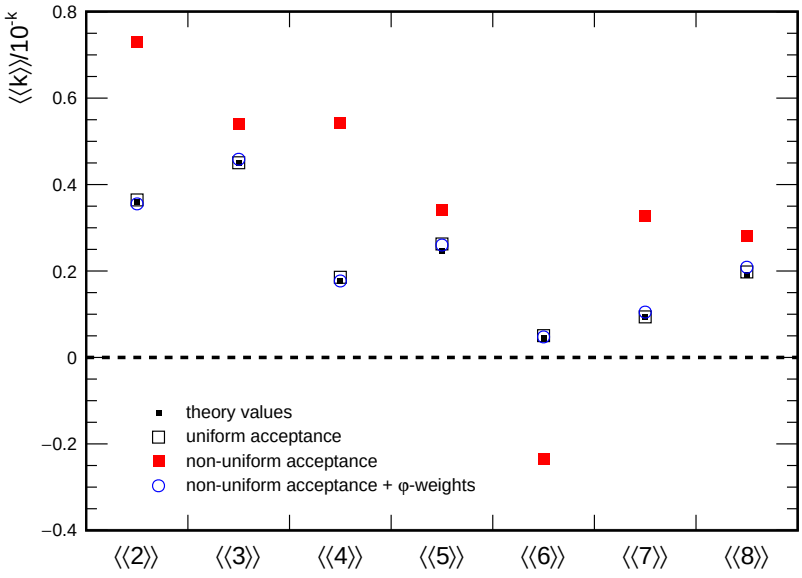

Figure 2.17.: Multiparticle correlators computed using the described generic framework. The results for uniform acceptance and the corrected results using weights agree with the theory values. The results with non-uniform acceptance and without weights are off by up to a factor of two or can even have the wrong sign.

we can see the framework is able to compute arbitrary multiparticle correlators while correcting for systematic biases and multiplicity fluctuations.

2.12. Monte Carlo closure

After verifying the generic framework with Monte Carlo data we will now perform a Monte Carlo closure, i.e. we will verify that the framework also works using real data. We will perform the closure in several steps. Firstly, we will compute multiparticle correlators over a real data set, giving us base line values for our correlators. We will be using the same correlators as the used in section 2.11, namely eqs. (2.75) to (2.81). After computing the base line, we will artificially introduce detector inefficiencies and compute the correlators again with and without using particle weights. The detector inefficiencies will be same as the one discussed in section 2.9. Lastly, we compare our base line with these values and see if we managed to correct for our known detector conditions. The data used is taken from Run 000137161 of the LHC Run 1 data set from 2010. The main reason we chose this data set is because the detector conditions where mostly stable during the data taking and we can reasonably assume uniform acceptance of azimuthal angles for the whole set. Perfect for introducing our own inefficiencies. The results can be seen in fig. 2.18. As we can see the framework is able to reproduce the base line values

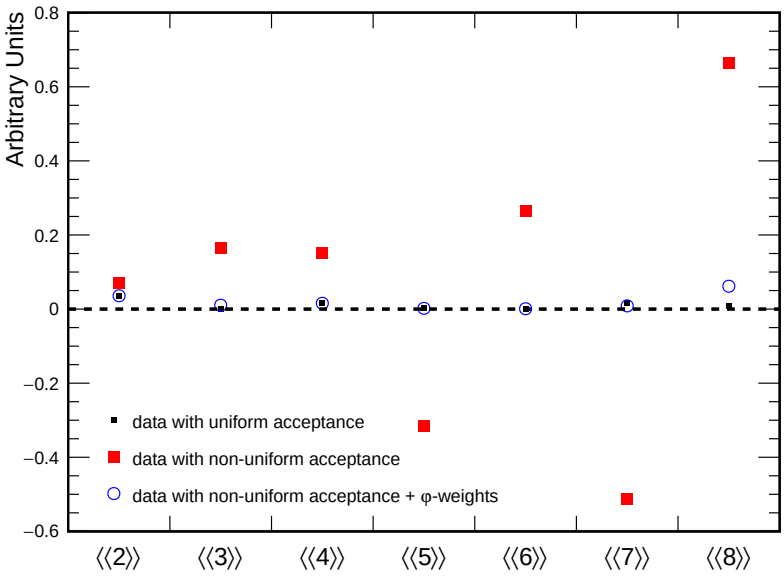

Figure 2.18.: Multiparticle correlators computed using the generic framework using real data from Run 000137161 of LHC Run 1 data set from 2010. The unmodified data with uniform acceptance are taken as a base line. The results with non-uniform acceptance and weights are able to reproduce the base line.

of arbitrary multiparticle correlators while correcting for systematic biases.

2.13. Symmetric Cumulants

Now that we are able to compute generic multiparticle correlators we will generalize the idea of estimating flow harmonics with cumulants to estimate the correlations between flow harmonics with so-called Symmetric Cumulants (SC). We neglected so far that even in events where the initial collision geometry is similar, i.e. within the same centrality class, due to the quantum nature of the whole collision system we expect the values of the flow amplitudes to fluctuate. Measuring these fluctuation gives independent and non-trivial constrains on the properties of the QGP. We can motivate this with the following observation. The correlation of even flow harmonics like v_2, v_4, ... can be attributed to fluctuations in the ellipsoidal shape of the interaction region in mid-central heavy ion collisions [14]. For example SC$(2,4)$ or SC$(2,4,6)$ will be able to quantify such fluctuations. However, if an observable like SC$(2,3,4)$ is also non-vanishing, then this would imply that there are additional fluctuations in the system which couple v_2, v_3 and v_4 which can not be captured by a cumulant of only even harmonics. We already showed how to estimate one flow harmonic v_n with a 4-particle correlator, by choosing $X_1 = e^{in\varphi_1}$, $X_2 = e^{in\varphi_2}$, $X_3 = e^{-in\varphi_3}$ and $X_4 = e^{-in\varphi_4}$. To generalize this idea to two flow harmonics v_n and v_m we now choose $X_1 = e^{in\varphi_1}$, $X_2 = e^{-in\varphi_2}$, $X_3 = e^{im\varphi_3}$, $X_4 = e^{-im\varphi_4}$. Thus we define the Symmetric Cumulant between v_n and v_m with

$$\mathrm{SC}(n,m) \equiv \left\langle e^{in(\varphi_1-\varphi_2)+im(\varphi_3-\varphi_4)} \right\rangle_c , \tag{2.82}$$

$$= \left\langle v_n^2 v_m^2 \right\rangle - \left\langle v_n^2 \right\rangle \left\langle v_m^2 \right\rangle . \tag{2.83}$$

As we can see SCs are symmetric under the exchange of the two harmonics n and m. This will in general be true also for higher order SCs. Similarly we can define a SC between three flow amplitudes v_k, v_l and v_m with

$$\begin{aligned}\mathrm{SC}(k,l,m) = \left\langle v_k^2 v_l^2 v_m^2 \right\rangle - \left\langle v_k^2 v_l^2 \right\rangle \left\langle v_m^2 \right\rangle - \left\langle v_k^2 v_m^2 \right\rangle \left\langle v_l^2 \right\rangle - \left\langle v_l^2 v_m^2 \right\rangle \left\langle v_k^2 \right\rangle \\ + 2 \left\langle v_k^2 \right\rangle \left\langle v_l^2 \right\rangle \left\langle v_m^2 \right\rangle .\end{aligned} \tag{2.84}$$

We can illustrate the sensitivity of SCs to the correlation between flow harmonics with a Toy Monte Carlo study. Let us assume a PDF expanded as in eq. (2.6), where all harmonics are zero except for v_2 and v_3. Further, we assume that the values of both of v_2 and v_3 fluctuate according to this PDF,

$$f(v_2, v_3) = \mathcal{N} \cdot (v_2 + v_3) , \tag{2.85}$$

where $\mathcal{N}$ is the normalization constant and we restrict $v_2 \in [0.15, 0.25]$ and $v_3 \in [0.05, 0.15]$. Note that this PDF cannot be factorized, i.e. $f(v_2, v_3) \neq f_{v_2}(v_2) f_{v_3}(v_3)$, meaning that v_2 and v_3 are not independent and their fluctuations are correlated. This means the computation of SC(2,3) will give a non-vanishing value. We generate 10^6 events where we sample the values v_2 and v_3 from eq. (2.85). Then we sample between

500 and 1500 particles in each event and compute SC(2,3) according to eq. (2.83) and fill the result into a TProfile. The uncertainty of SC(2,3) will be computed with the bootstrap method. The result of the study can be seen in fig. 2.19. The result agrees

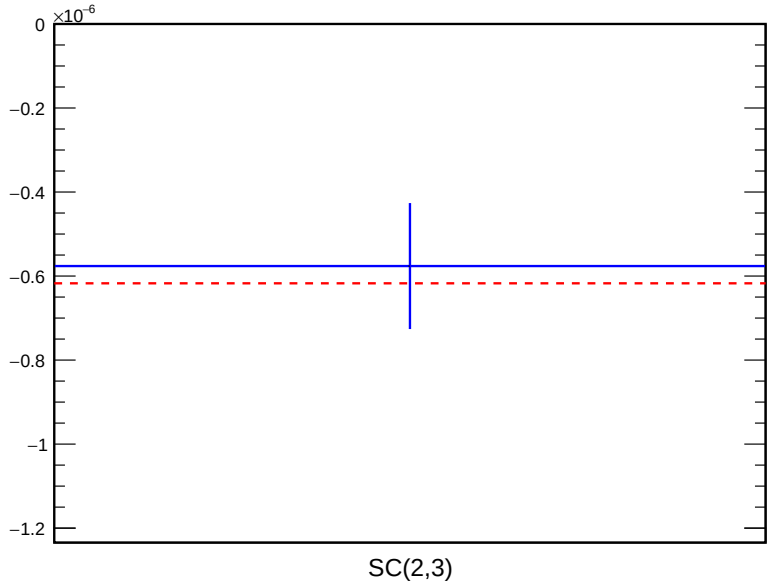

Figure 2.19.: SC(2,3) for 10^6 events with a number of particles between 500 and 1500 each. The expected value of $\mathrm{SC}(2,3) = -6.1728 \times 10^{-7}$ is marked with a red dashed line. The mean value of over all events is $(-5.7621 \pm 1.4992) \times 10^{-7}$.

with the theoretical value within its uncertainty.

3. Experimental Setup

3.1. A Large Ion Collider Experiment (ALICE)

ALICE is one of the four major detector experiments at the Large Hadron Collider (LHC) at CERN. It contains 18 subdetectors, some of which can be seen in the schematic shown in fig. 3.1. In particular the Time Projection Chamber (TPC), the Inner Tracking System

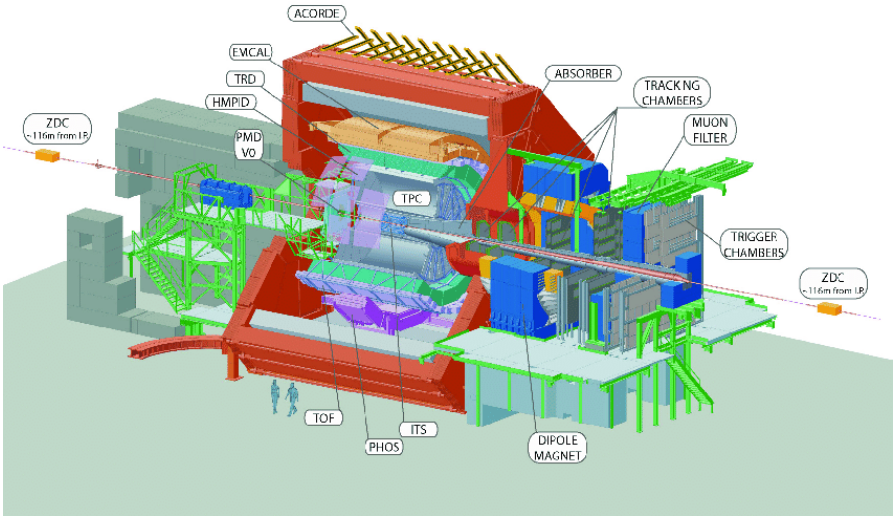

Figure 3.1.: ALICE detector.

(ITS) and the VZERO were used for the analysis presented in the thesis and will be discussed in more detail in the following sections. The ALICE experiment is optimized for heavy-ion collisions for a center of mass energy of up to 5.02 TeV. There are several possible beam configurations, but we will concentrate on Pb–Pb collisions. The resulting energy density and temperature in such collisions allows the study of the properties of quark-gluon plasma, a deconfined state of matter where even hadrons are melted down into their composite particles. This is the state the universe was in shortly after the Big Bang, before it cooled down enough to allow quarks and gluons to form hadrons. The secondary goal of ALICE is to try to answer why the sum of the individual quark masses are so much lighter than the mass of the composite objects they are building up.

3.2. Time Projection Chamber (TPC)

The TPC detector is a type of detector that uses electrical and magnetic field in combination with a sensitive volume of gas to perform a three-dimensional reconstruction of particle trajectories. A schematic view can be see in fig. 3.2 It has cylindrical shape

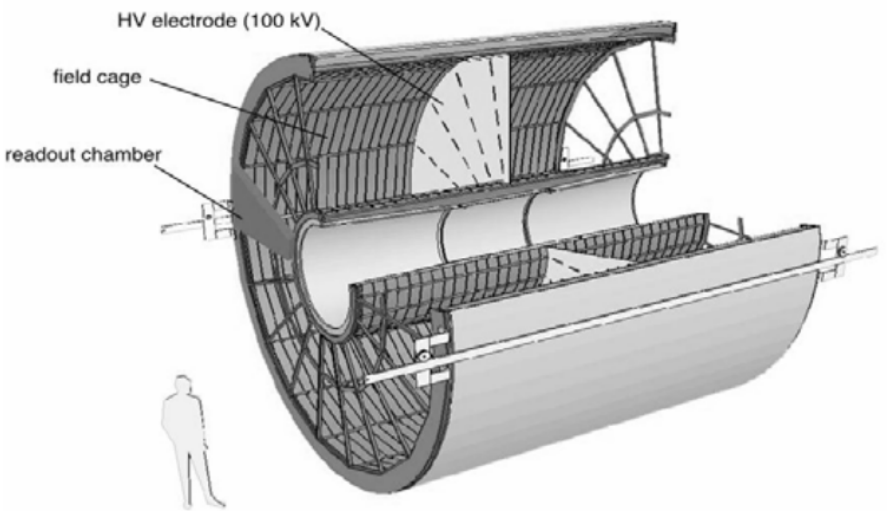

Figure 3.2.: ALICE's TPC.

separated in two volumes with a cathode in the middle, with a longitudinal length of 5 m, an inner radius of 85 cm and outer radius of 250 cm. Its chambers are filled with with $90\,\mathrm{m}^3$ gas mixture of $\mathrm{Ne}/\mathrm{CO}_2/\mathrm{N}_2$. Charged particles traversing through the TPC ionize the gas after which the produced electrons travel to the end plates along a electric field. The z coordinates of the track can be determined with the drift time, i.e. the time the electrons need to travel to the end plates, while the r and ϕ coordinates are obtained directly by the measuring the positions on which the electrons impact the end plates. The slow drift time of $\approx 90\,\mu\mathrm{s}$ is limiting the maximum luminosity that ALICE can handle. The TPC was designed to cope with the large number of particles which can be produced in Pb–Pb events, which in the most central collisions can reach about 20 000 primary and secondary particles. The TPC is capable of detecting particles in the transverse momentum range of $0.1\,\mathrm{GeV}/c < p_\mathrm{T} < 100\,\mathrm{GeV}/c$ with a resolution of about 6 % for $p_\mathrm{T} < 20\,\mathrm{GeV}/c$ in central Pb–Pb collisions. For higher transverse momenta the resolution deteriorates. In contrast the track finding efficiency of the TPC saturates at around 90 % for $p_\mathrm{T} > 1\,\mathrm{GeV}/c$. It covers nearly all azimuthal angels. Due to dead zones between the neighboring sectors about 10 % are lost. The azimuthal resolution is about $\Delta\varphi = 0.7 \times 10^{-3}$, not depending on the transverse momentum. The TPC can track particles whose pseudorapidity is $|\eta| < 0.9$ if only the tracks with maximum radial track length are being considered. While the primary use of the TPC is tracking particles, it can also be used for particle identification (PID) via the standard $\mathrm{d}E/\mathrm{d}x$ technique.

Additionally, TPC can also be used as a centrality estimator with a resolution of about 0.5 % centrality bin width in the most central collisions. For Run 3 operations at LHC and beyond, the TPC has been equipped with new GEM-based technology, which enables must faster readout.

3.3. Inner Tracking System (ITS)

The Inner Tracking System of ALICE consists of 6 silicon layers, grouped into three distinct groups of two layers, forming three distinct detectors. The two innermost silicon layers are Silicon Pixel Detector (SPD), the third and fourth layer are Silicon Drift Detectors (SSD) and the two outermost layers are Silicon Strip Detectors (SSD). The ITS and its subcomponents can be seen in fig. 3.3. The ITS is situated between the

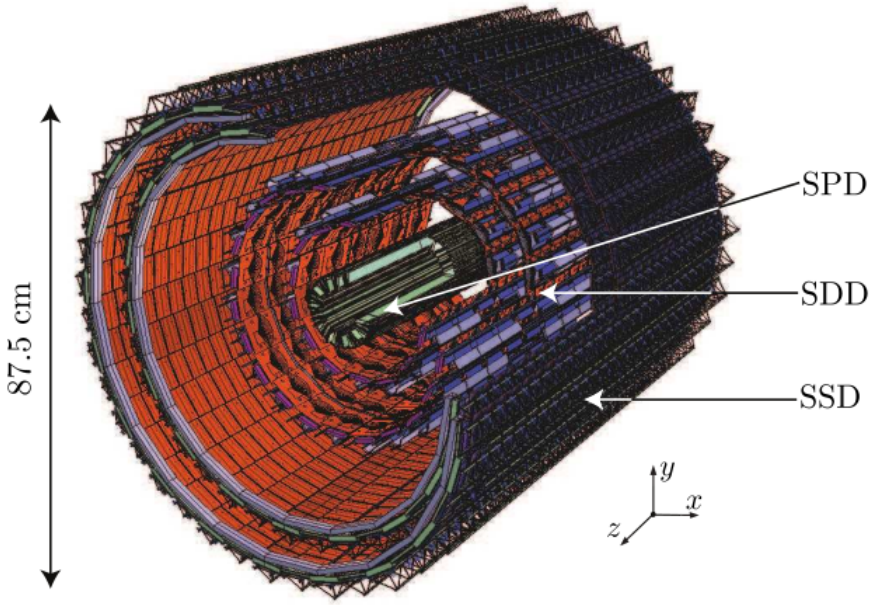

Figure 3.3.: ALICE's ITS. The innermost part is the Silicon Pixel Detector (SPD), the middle part is the Silicon Drift Chamber (SDD) and the outer most part is the Silicon Strip Detector (SSD).

inner side of the TPC and the beam pipe. It is being used both for the primary vertex reconstruction as well as the reconstruction of secondary particles. It can detect particles within a transverse momentum range of $0.1\,\mathrm{GeV}/c < p_\mathrm{T} < 3\,\mathrm{GeV}/c$ with a relative resolution better than 2 % for pions. For $p_\mathrm{T} > 3\,\mathrm{GeV}/c$ it can give additional information to improve the transverse momentum resolution for the tracks which are also captured by the TPC. By design it has the coverage as the TPC for pseudorapidity and azimuthal angles, but due to cooling problems in the two innermost layers the azimuthal acceptance

is not uniform. Even though ITS has these standalone tracking capabilities, especially for tracking charged particles that traverse the dead zones of the TPC or do not even reach the TPC due to their small momentum, its main role it to improve the transverse momentum and azimuthal angle resolution of the particles reconstructed by the TPC. It can also use standard $\mathrm{d}E/\mathrm{d}x$ techniques to determine the PID and it can also be use as a centrality estimator with a resolution for about 0.5 % centrality bin width in the most central collision.

3.4. VZERO

The VZERO detector consists of two different arrays of scintillator counters, V0A and V0C, placed on opposite sides of the central barrel detectors perpendicular to the beam line. The positions of V0A and V0C can be seen in fig. 3.4. They are placed asymmetrically

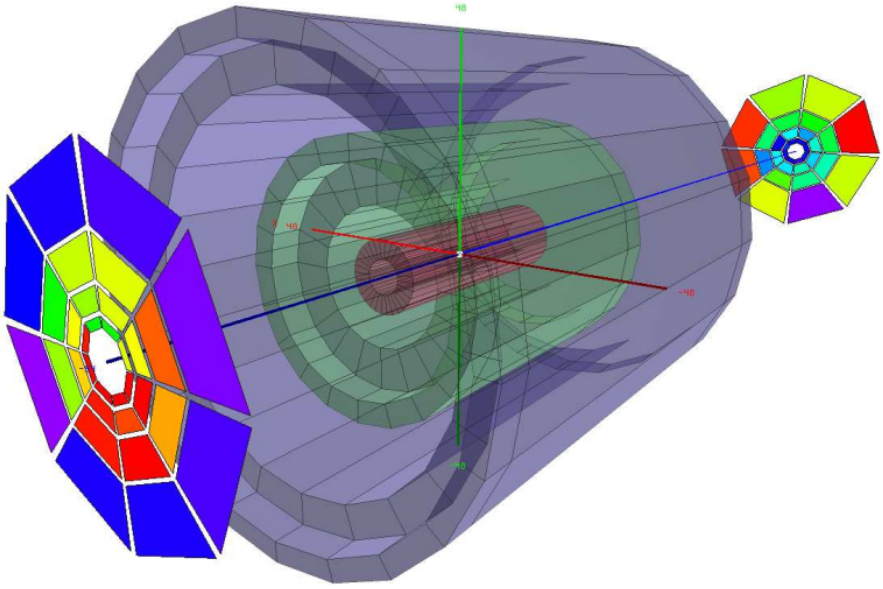

Figure 3.4.: VZERO detectors on both sides of the ITS.

with respect to the interaction point. V0A is located 340 cm and V0C is placed 90 cm from the interaction point. Due to this asymmetry, they have different pseudorapidity coverage. V0A covers pseudorapidity range $2.8 < \eta < 5.1$, while V0C covers $-3.7 < \eta < -1.7$. Each of them contain 32 elementary counters arranged in 4 rings and 8 sectors of 45°. The VZERO detectors serve several purposes within the ALICE experiment. Both of them provide and online trigger and are use as centrality estimators, with a resolution of about 0.5 % centrality bin width in the most central collisions better than 2 % of centrality bin width for peripheral collisions.

4. Data Validation

In this chapter we outline the event and track selection criteria (cuts) applied in the analysis. We illustrate the effects of the various cuts on the distributions of the physical quantities of interest. In section 4.1 we outline the cuts applied on event observables and in section 4.2 the cuts applied on track observables. After applying all cuts the analysis still has to be corrected for detector inefficiencies. Therefore we will demonstrate in section 4.3 how the track weights are computed and show their distribution. In the last section of this chapter, section 4.4, we outline all systematic variations used for the computation of systematic errors and how they change the data sample. The analysis is performed on the Pb–Pb collision data taken by the LHC Run 1 in 2010 with the ALICE detector with a collision energy of $\sqrt{s_{\mathrm{NN}}} = 2.76\,\mathrm{TeV}$.

4.1. Event cuts

The default cuts on event observables are shown in table 4.1. We also cut on centrality,

Table 4.1.: List of all default event cuts and their respective ranges.

observable	Range
multiplicity M	$12 \leq M \leq 3000$
Vertex coordinate in X-direction $\mathbf{V}_X$	$-1\,\mathrm{cm} \leq \mathbf{V}_X \leq 1\,\mathrm{cm}$
Vertex coordinate in Y-direction $\mathbf{V}_Y$	$-1\,\mathrm{cm} \leq \mathbf{V}_Y \leq 1\,\mathrm{cm}$
Vertex coordinate in Z-direction $\mathbf{V}_Z$	$-10\,\mathrm{cm} \leq \mathbf{V}_Z \leq 10\,\mathrm{cm}$
Vertex distance from the origin $\lvert\mathbf{V}\rvert$	$1 \times 10^{-6}\,\mathrm{cm} \leq \lvert\mathbf{V}\rvert \leq 18\,\mathrm{cm}$

depending on the centrality bin we want to analyze. The centrality bins are shown in table 4.2. Additionally, we use correlation cuts between different centrality and multiplicity

Table 4.2.: Centrality bins for data analysis.

	bins
centrality [%]	$(0.0; 5.0)$, $(5.0; 10)$, $(10; 20)$, $(20; 30)$, $(30; 40)$, $(40; 50)$, $(50; 60)$, $(60; 70)$, $(70; 80)$

estimators which will be outlined in section 4.1.4.

4.1.1. Cut on centrality

The histogram of the centrality distribution of the whole data set before and after applying event cuts can be seen in fig. 4.1. To avoid bias in the data analysis it is important the

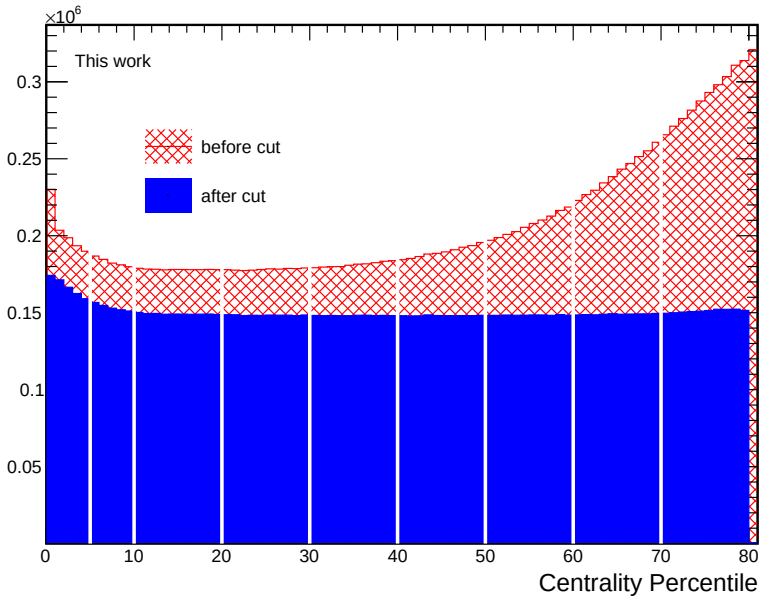

Figure 4.1.: Centrality distribution of the whole data set before and after applying event cuts. The edges of the centrality bins are indicated with white spacing.

centrality distribution is flat. As can be seen in fig. 4.1 there is small excess in events for centralities smaller than 10 % after applying all cuts. However, since the excess events are in the regime of head-on collisions, where the initial anisotropy is small due to the almost circular collision geometry we expect a weak flow signature anyway and therefore this region is not of main interest in this analysis. The main interest is in the realm of mid-central collisions, 20 % to 50 %, where anisotropies are large and the flow signature in the data is strong. Here the centrality distribution is flat. It is possible to flatten the centrality distribution with the use of centrality weights. A weight is assigned to each centrality bin. The larger the count in the bin with respect to the average bin content the smaller will be weight. These weights indicate the probability of including the event in the analysis. Meaning if there is bin with a bin count higher than the average, events within this centrality bin have a lesser probability of being included in the analysis. Using weights like this we randomly remove excess events with as little bias as possible and the centrality distribution is flattened. But as we argued above, the centrality distribution is flat in the centrality region of interest and we therefore forego the use of centrality weights.

4.1.2. Cut on multiplicity

In this thesis we estimate the multiplicity M of an event with the number of tracks that will be used for the computation of Q-vectors. This means that the multiplicity is be the number of particles in an event that survive the track cuts that are outlined in section 4.2. We also compare this multiplicity estimate to a so-called reference multiplicity M_{ref}. If these two estimates differ too much then we also cut these events away. The histograms of the multiplicity estimate of the whole data set in centrality bin 0 % to 5 % and 40 % to 50 % before and after applying event cuts are shown in fig. 4.2. The shape of the

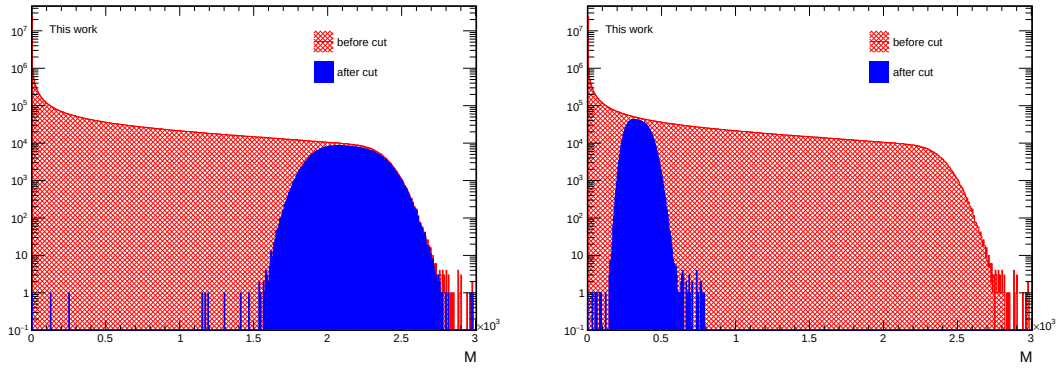

(a) Multiplicity distribution in centrality bin 0 % to 5 %.

(b) Multiplicity distribution in centrality bin 40 % to 50 %.

Figure 4.2.: Distribution of multiplicity estimate before and after applying event cuts of the whole data set in different centrality bins. The y-axis is scaled logarithmically.

multiplicity distribution after the event cuts is mainly determined by the choice of the centrality bin. The centrality determines the collision geometry. The smaller it is, the more the colliding heavy-ions overlap, the more particles collide and the more energy is deposited into the collision volume. This means more particles are produced in collision with small centrality compared to larger centrality. As is shown in fig. 4.2, in events within 0 % to 5 % the number of particles is way larger than for 40 % to 50 %. The multiplicity range detailed in table 4.1 is more of a sanity check than an actual cut since nearly all healthy events lie within that range. We also point out that the distributions are peaked and that there are no so-called high multiplicity outliers. These are events which have a much higher multiplicity then any other event in the same centrality bin. Since we need to weight the Q-vectors of an event by its multiplicity weight, which scales like $\propto M^k$ for a k-particle correlator, this would mean that a single event could potentially outweigh the whole sample if its multiplicity is much larger than the average multiplicity within a given centrality bin. This also means events which have a very small multiplicity compared to the other events have hardly any impact on the computation. In the shown

distributions we see a few events which have a slightly larger multiplicity than most other events, but these are well within expectations and under control.

4.1.3. Cuts on vertex position

The histograms of the different components of the primary vertex position as well as the absolute distance from the origin before and after applying event cuts of the whole data set in centrality bin 40 % to 50 % can be seen in fig. 4.3. The distributions of $\mathbf{V}_X$, $\mathbf{V}_Y$,

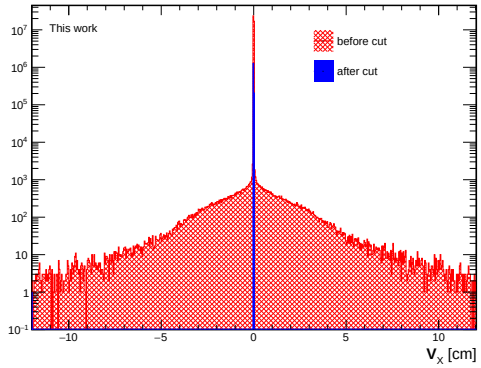

(a) Distribution of $\mathbf{V}_X$, before and after applying event cuts.

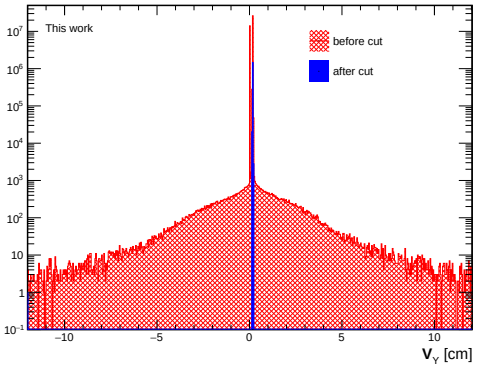

(b) Distribution of $\mathbf{V}_Y$, before and after applying event cuts.

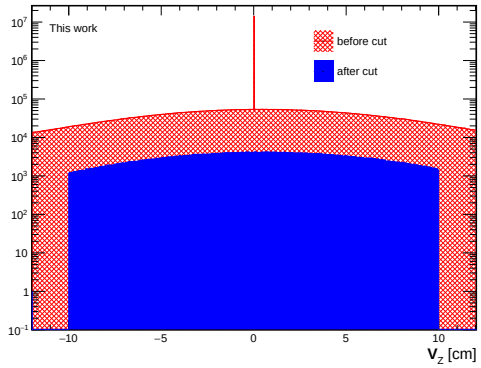

(c) Distribution of $\mathbf{V}_Z$, before and after applying event cuts.

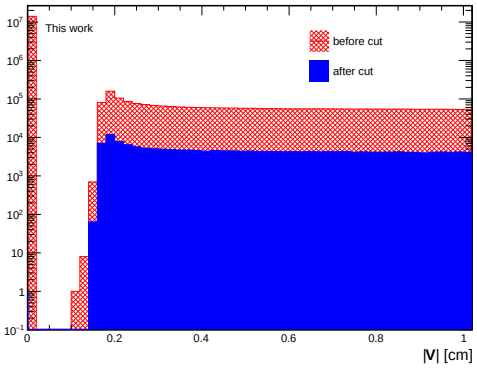

(d) Distribution of $|\mathbf{V}|$, before and after applying event cuts. Distribution is only shown up to 1 cm.

Figure 4.3.: Distributions of vertex coordinates before and after applying event cuts of the whole data set in centrality bin 40 % to 50 %. The y-axis is scaled logarithmically.

$\mathbf{V}_Z$ and $|\mathbf{V}|$ before applying the event cuts are strongly peaked near 0. $\mathbf{V}_Z$ is also more evenly distributed than $\mathbf{V}_X$ and $\mathbf{V}_Y$. This is due to the fact that it is easier to focus the beam in the transverse directions than in the longitudinal direction. After applying the cuts we are left with the peaks in the $\mathbf{V}_X$ and $\mathbf{V}_Y$ distribution, while we loose the sharp peak in the $\mathbf{V}_Z$ distribution. This is also mirrored in the $|\mathbf{V}|$ distribution where we loose all events at 0 due to the cut applied on this observable. In fact, the events we cut away are all suspicious in the sense that the primary vertex is directly situated at the origin where $|\mathbf{V}| = 0$ exactly. This is the reason why this cut was applied in the first place. It is very unlikely that the primary vertex is exactly at the origin and there was probably an issue with the detector or reconstruction software that set this value to 0. Nevertheless, we decided to not use these event in the analysis. The loss in statistics is not large since most of these event would have been cut away but other event cuts anyway. The cut on $\mathbf{V}_Z$ is by comparison way more substantial and we loose a significant amount of statistics. But if the primary vertex is far away from the nominal interaction point, then the produced particles cannot be measured optimally by the detectors. Therefore, this cut is very important to guarantee the quality of the data.

4.1.4. Correlation cuts

For both centrality and multiplicity there are several choices of estimators possible. Since we do not want to bias the analysis by the choice of a particular estimator and assume that if two estimators for the same observable are not consistent then there is something wrong with the event, we cut those events away. We can check if two estimators are consistent by plotting the correlation between them in a 2D histogram and cut the event if the estimates differ more than some set amount. If the two estimates are perfectly consistent, then the correlation plot will simply be a linear function $f(x) = x$, since the estimate of one equals the other. We can then define an upper limit with another linear function $g(x) = mx + t$ above which we cut events away. By reflecting g on f we get lower bound $h(x) = \frac{x-t}{m}$, resulting in a cone around f in which we require the events to be. We obviously assume here a linear correlation between our estimates. The parameters defining the cut are hence the slope m and the offset t. This concept is illustrated in fig. 4.4. The results in this section will be shown in the full centrality range from 0 % to 80 %.

Centrality correlation cut

In ALICE there are four centrality estimators available, i.e.

- V0M,

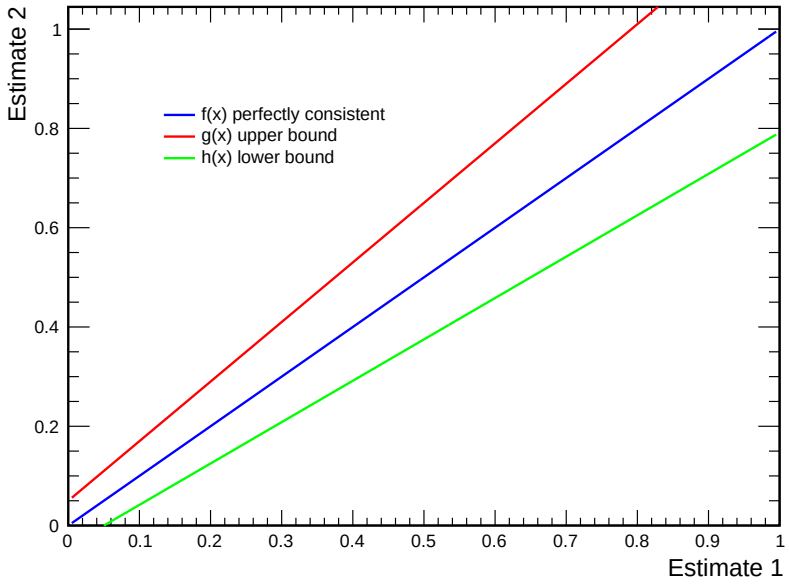

Figure 4.4.: Principle correlation cut.

- CL0,
- CL1,
- SPD tracklets.

For the analysis we use V0M as the default centrality estimator. We require the estimates for all 4 centrality estimators to be consistent. Hence we perform $\frac{4 \cdot 3}{2} = 6$ correlation cuts between any two centrality estimators. The parameters for these cuts are shown in table 4.3. In fig. 4.5 the correlation distribution between V0M and SPD tracklets

Table 4.3.: Parameter values for centrality correlation cut.

$g(x) = mx + t$ $h(x) = \frac{x-t}{m}$	value
slope m	1.0
offset t	10

are shown. Generating 2D correlation histograms is computationally very expensive and requires a lot of disk space hence the validation was performed only on subset of the data set. Figure 4.5 illustrates the correlation cut perform on Run 000137161 of the 2010 data set. There are quite a few events where centrality estimator SPD tracklets underestimates the centrality percentile compared to V0M, for the bulk of the events the estimates are

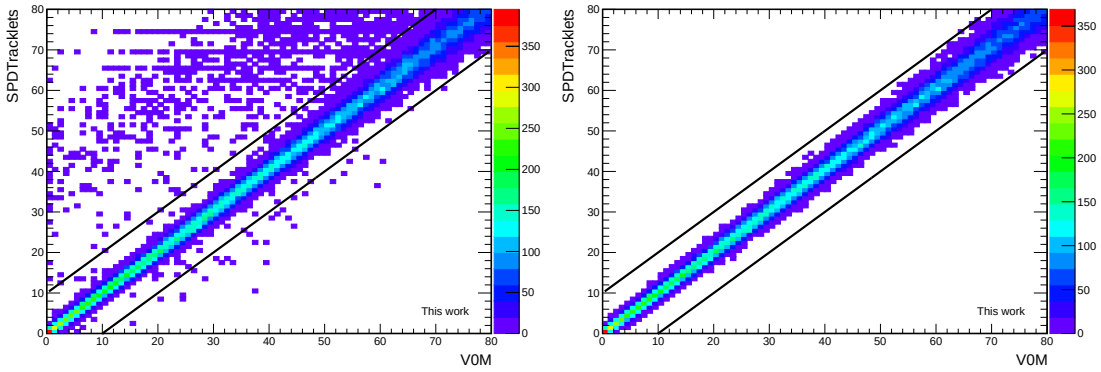

(a) Correlation between V0M and SPD tracklets before applying event cuts.

(b) Correlation between V0M and SPD tracklets after applying event cuts.

Figure 4.5.: Centrality correlation histograms between V0M and SPD tracklets before and after applying cuts in Run 000137161. The correlation cut is indicated with two black lines.

consistent.

Multiplicity correlation cut

There are several possible choices for multiplicity estimator. In section 2.5 we have shown why it is sensible to define the multiplicity as the number of tracks used for the computation of Q-vectors. But this choice is not generally accepted so we want to make our choice for the multiplicity M generally consistent with M_{ref}. The values for the multiplicity correlation cut can be seen in table 4.4. Incidentally, this cut also takes care

Table 4.4.: Parameter values for multiplicity correlation cut.

$g(x) = mx + t$ $h(x) = \frac{x-t}{m}$	value
slope m	1.4
offset t	300

of high-multiplicity outliers events we briefly mentioned before. The correlation between M and M_{ref} in Run 000137161 before and after applying event cuts can be seen in fig. 4.6. The distribution shows that for small multiplicities both estimates are consistent with each other and that for larger multiplicities M_{ref} takes larger values than M. This can be understood as follows. Since M_{ref} is a estimate given by the detector, it will not be changed by subsequent track cuts. M on the other hand is the number of tracks we use

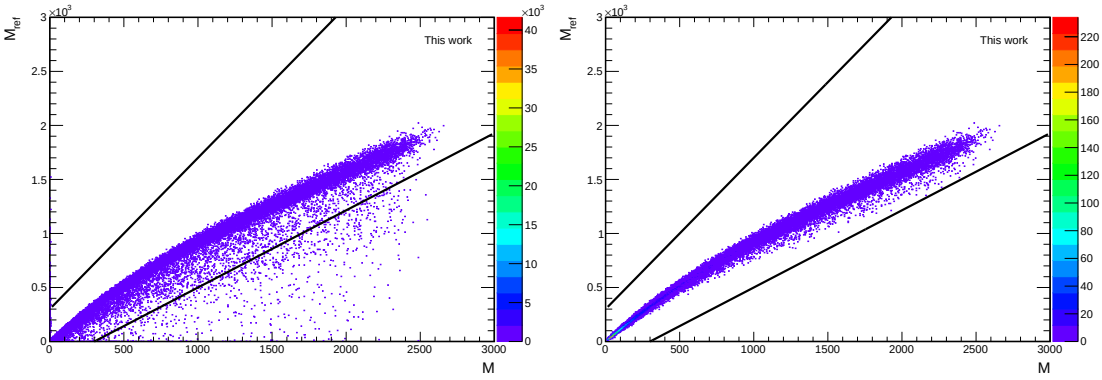

(a) Multiplicity correlation between M and M_{ref} before applying event cuts.

(b) Multiplicity correlation between M and M_{ref} after applying event cuts.

Figure 4.6.: Multiplicity correlation histograms between M and M_{ref} before and after applying cuts of in Run 000137161. The correlation cut is indicated with two black lines.

in the computation of Q-vectors and after applying event cuts we still apply further track cuts, reducing the amount of tracks used for the analysis.

Correlation between multiplicity and centrality

In this section we briefly want to show the correlation between the multiplicity estimates M_{ref} and centrality. We do not cut on this correlation directly and we know the expected shape of the correlation. Therefore looking at this correlation it gives a nice visual confirmation that the applied event cuts do not introduce any obvious biases into the analysis. We use M_{ref} instead of M because it is constant and not affected by the subsequent track cuts. The correlation plot between the centrality and M_{ref} is shown in fig. 4.7. The correlation between centrality and M_{ref} is, as expected, monotonically decreasing. The larger the centrality class, the further apart the two colliding heavy-ions are and the smaller the overlapping region becomes. This means we have a smaller volume containing interacting matter and less deposited energy in the collision, which means less particles are produced and the multiplicity decreases.

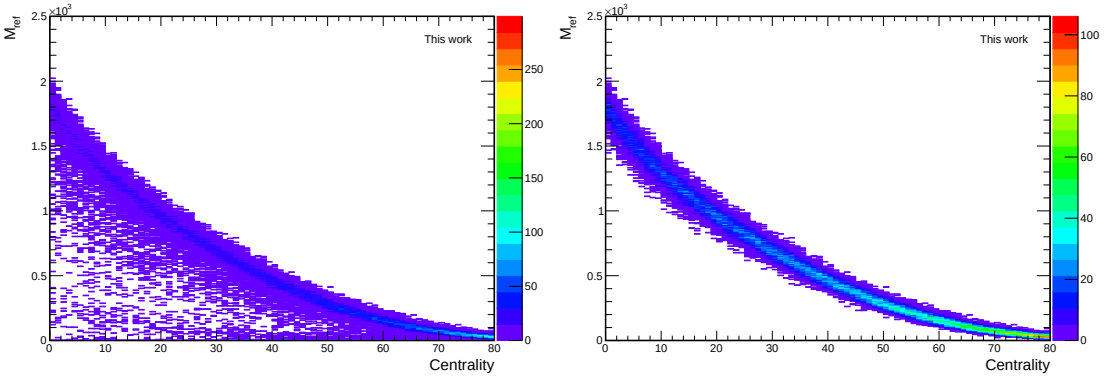

(a) Correlation between M_{ref} and centrality before applying event cuts.

(b) Correlation between M_{ref} and centrality after applying event cuts.

Figure 4.7.: Centrality and reference multiplicity correlation histograms before and after applying cuts of in Run 000137161.

4.2. Track cuts

Track cuts are applied to each reconstructed track in an event. If they are cut, they will not be used in the computation of Q-vectors and are not used in the analysis. The values or ranges for the different cuts can be seen in table 4.5. In the analysis we will only

Table 4.5.: List of all track cuts and their respective ranges or values.

observable	Range/Value
transverse momentum p_{T}	$0.2\,\mathrm{GeV}/c \leq p_{\mathrm{T}} \leq 5\,\mathrm{GeV}/c$
pseudorapidity η	$-0.8 \leq \eta \leq 0.8$
azimuthal angle φ	$0 \leq \varphi \leq 2\pi$
charge q	$-1 \leq q \leq 1$ and $q \neq 0$
primary particles only	true
DCA in Z-direction DCA_Z	$-2.4\,\mathrm{cm} \leq DCA_Z \leq 2.4\,\mathrm{cm}$
DCA in XY-plane DCA_{XY}	$-3.2\,\mathrm{cm} \leq DCA_{XY} \leq 3.2\,\mathrm{cm}$
Filterbit	128
Goodness of TPC track fits χ^2_{TPC}/NDF	$0 \leq \chi^2_{TPC}/NDF \leq 4$
Number of TPC clusters n_{TPC}	$70 \leq n_{TPC} \leq 160$

use particles which are labeled as primary, i.e. particle which were generated from the cooling QGP and not from a subsequent decay of a heavier particles, and particles which are charged. Furthermore, the ALICE collaboration provides predefined cuts on various observables known as Filterbits. In this analysis Filterbit 128 was used, which indicated that tracks were reconstructed only by using the information from TPC detector.

4.2.1. Kinematic cuts

The distributions of the kinematic track variables, i.e. transverse momentum p_{T}, pseudo-rapidity η, azimuthal angle φ and charge q, of all tracks in the whole data set in centrality bin 40 % to 50 % before and after applying cuts are shown in in fig. 4.8. We see that

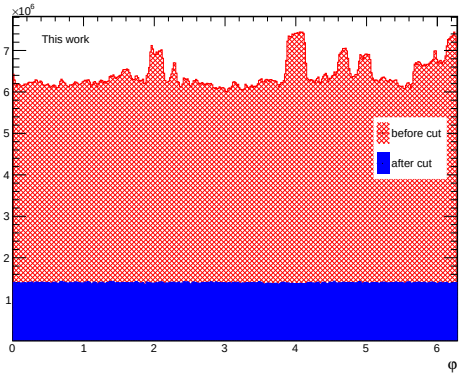

(a) φ distribution.

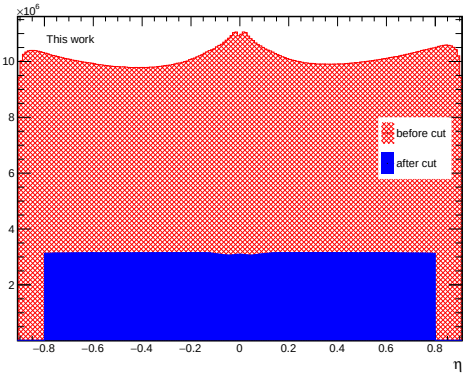

(b) η distribution.

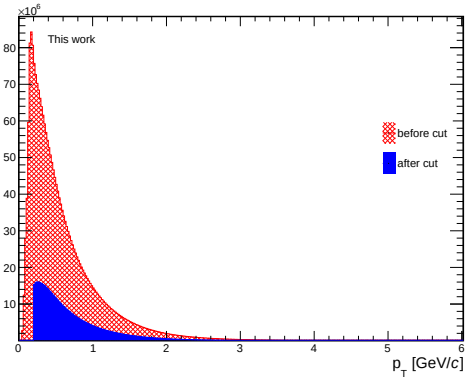

(c) p_{T} distribution.

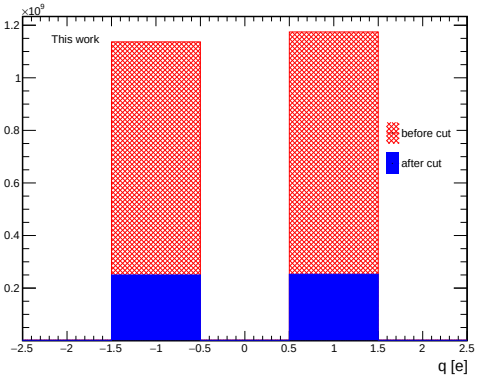

(d) q distribution.

Figure 4.8.: Distributions of kinematic track variables of the whole data set in centrality bin 40 % to 50 % before and after applying track cuts.

the cuts manage to flatten the φ, η and q distribution while the p_{T} takes the from of a Boltzmann. We do not apply any cut on φ since the TPC has uniform acceptance over the whole 2π range, as demonstrated by the flat distribution after applying the track cuts. The η and q distribution flatten out after applying the track cuts. Several physical effects favor the production of positive particles when the particles produced in the heavy-ion collision interact with the detectors, which leads to an overabundance of positive particles. The applied cuts are also able to reduce this discrepancy.

4.2.2. Track quality cuts

In this section we present cuts which are performed to ensure the quality of the tracks used for the analysis. These cuts are necessary since a track is not always close to the center of the detector, the detector conditions are not always ideal, the reconstruction software is not perfect and the list goes on. The results can be seen in fig. 4.9. The cut on

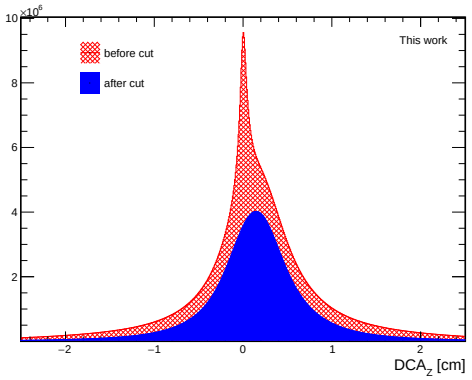

(a) DCA_Z distribution.

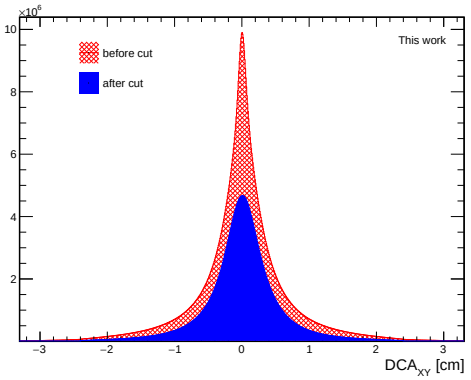

(b) DCA_{XY} distribution.

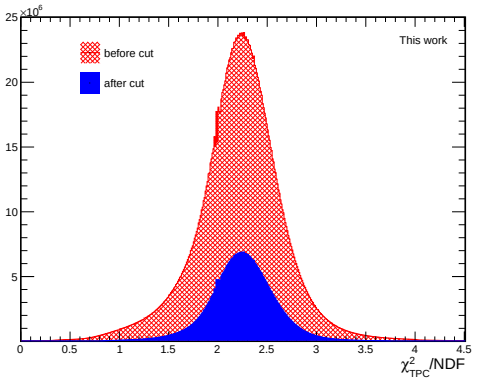

(c) $\chi^2_{TPC}/_{NDF}$ distribution.

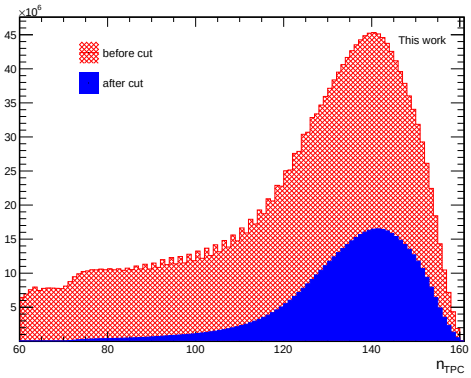

(d) n_{TPC} distribution.

Figure 4.9.: Distributions of track quality variables of the whole data set in centrality bin 40 % to 50 % before and after applying track cuts.

the distance-of-closest-approach (DCA) of the extrapolated track to the primary position in Z-direction (DCA_Z) and the XY-plane (DCA_{XY}) is performed to ensure that the tracks are close to the primary vertex. This minimizes the contribution from secondary particles originating either from decays or interaction with the detector material. The distribution take a Gaussian-like form after applying the cuts. Cutting on n_{TPC} ensures that the track leaves enough cluster within the TPC to ensure good reconstruction. The distribution takes the form of a Poisson distribution with its maximum at approximately

140, which is close to 160, the maximum number of clusters a particle can leave in the TPC. The cut on χ^2_{TPC}/NDF also takes the form of a Gaussian and removes a majority of poorly reconstructed tracks and

4.3. Particle weights

Detector conditions are not always ideal and tracks can be missed, falsely identified, poorly reconstructed, etc. In the analysis we assume that the detector conditions are stable within a single run so weights are applied on a run-by-run basis. For this reason we will perform the analysis with weights, which were introduced in section 2.9, to correct for these inefficiencies. To compute particle weights we will use two approaches: data driven and Monte Carlo driven. We us the data driven method for the computation of φ-weights. Since we know that the φ-distribution over many events has to approach a flat distribution we can simply invert the measured φ-distribution bin-by-bin and gain the weights. This has the effect that bins with a count below the average, which indicates that the detector missed particles in this bin, have a higher weight than bins with a count above the average, where the detector did not miss any or less particles. The resulting distribution of φ-weights for Run 000137161 can be seen in fig. 4.10. The absolute value

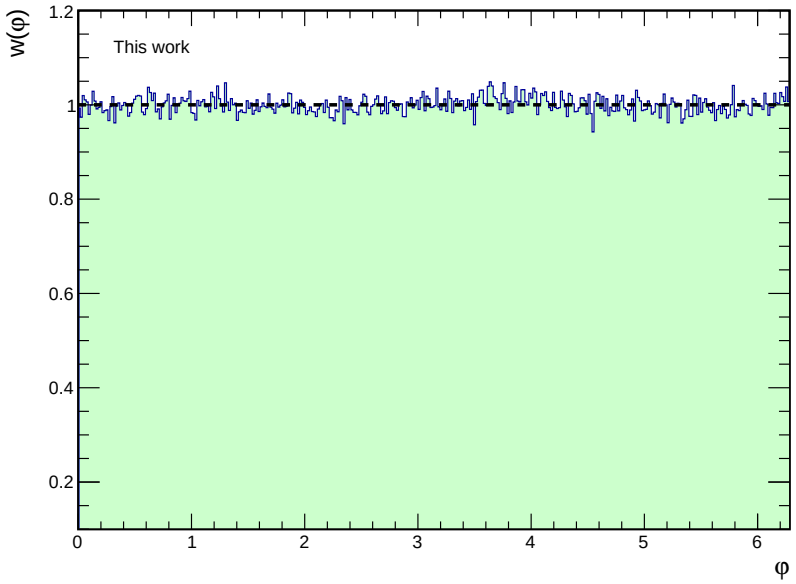

Figure 4.10.: φ-weights for Run 000137161 compute using a data-driven approach. The value 1 is indicated with a dash blue line.

of the weights does not matter but we have scaled them such that they are close to one.

As we have already shown the φ-distribution for all Runs after applying track cuts in fig. 4.8a, which was already flat, it is no surprise that the φ-weights are also very flat. This indicates that all azimuthal sectors of the used detector were performing equally well, without introducing any non-uniformities in the azimuthal distributions, which could be interpreted as a spurious anisotropic flow. The Monte Carlo driven approach is a bit more involved. Since we do not know which distribution to expect for p_{T} and η we compute their weights as the ratio between the distributions we measure and the distributions of a Monte Carlo simulation which simulates a heavy-ion collision of the same centrality and the same conditions of the real detector at the time of the collision. For this purpose we have chosen the Monte Carlo production that was anchored to the same data set we analyze in this thesis. The η-weights are close to one, as is expected given the η-

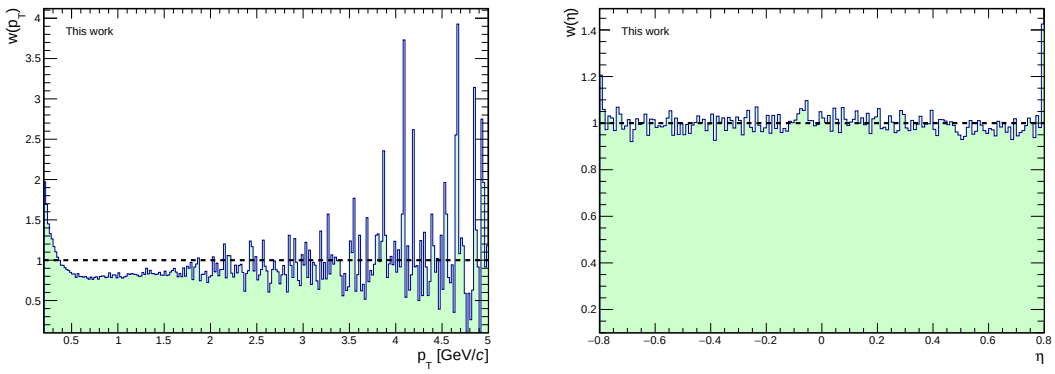

(a) p_{T}-weights for Run 000137161.

(b) η-weights for Run 000137161.

Figure 4.11.: p_{T}- and η-weights for Run 000137161 computed using Monte Carlo data. The value 1 is indicated with a blue, dashed line.

distribtuion in fig. 4.8b. Though, we do see a slight rise at the edges of the distribution. This is because at $|\eta| = 0.8$ we reach the edges of the TPC. The η-weights have similar distribution to the φ-weights because the TPC has a uniform pseudorapidity acceptance in the chosen range $|\eta| > 0.8$. The p_{T}-weights have a more complex distribution. The rise at momenta smaller than $0.5\,\mathrm{GeV}/c$ indicates that the detector has difficulties detecting particles with small momenta. Those are charged particles that spiral in the magnetic field in which the tracking detector is embedded and do not fully transverse TPC or may not even enter it. For momenta between $0.5\,\mathrm{GeV}/c$ and $2.0\,\mathrm{GeV}/c$ the acceptance is constant which indicates that the detector is working at optimal efficiency. The η-weights have similar distribution to the φ-weights because the TPC has a uniform pseudorapidity acceptance in the chosen range $|\eta| < 0.8$.

4.4. Systematic variations

In this section we summaries all systematic variations of the applied cuts for the computation of systematic uncertainties. All observables whose cuts have been varied are shown in table 4.6. All variations are performed independently of each other. The systematic

Table 4.6.: Table of all cut variations for the computation of systematic uncertainties.

observable	Variation	original value
Centrality	SPD tracklets	V0M
Centrality correlation	$m = 1.1; t = 11$	$m = 1.0; t = 10$
Multiplicity correlation	$m = 1.6; t = 350$	$m = 1.4; t = 300$
$\mathbf{V}_Z$	$-14\,\mathrm{cm} \leq \mathbf{V}_Z \leq 14\,\mathrm{cm}$	$-10\,\mathrm{cm} \leq \mathbf{V}_Z \leq 10\,\mathrm{cm}$
DCA_Z	$-2.2\,\mathrm{cm} \leq DCA_Z \leq 2.2\,\mathrm{cm}$	$-2.4\,\mathrm{cm} \leq DCA_Z \leq 2.4\,\mathrm{cm}$
DCA_{XY}	$-2.4\,\mathrm{cm} \leq DCA_{XY} \leq 2.4\,\mathrm{cm}$	$-3.2\,\mathrm{cm} \leq DCA_{XY} \leq 3.2\,\mathrm{cm}$
n_{TPC}	$60 < n_{TPC} < 160$	$70 < n_{TPC} < 160$
n_{TPC}	$80 < n_{TPC} < 160$	$70 < n_{TPC} < 160$
Filterbit	1	128
Filterbit	96	128
Filterbit	768	128

uncertainty σ_{sys} is determined by computing

$$\sigma_{sys} = \sqrt{\sum_{k}^{\text{Variations}} (\mu - \mu_k)^2}\,, \tag{4.1}$$

where the sum goes over all systematic variations, μ_k is the results for variation k and μ is the result of the default configuration.

4.4.1. Variation of event cuts

The variations of all event cuts are listed in table 4.6. The first variation is changing the centrality estimator from V0M to SPD tracklets. This variation has a very small effect since consistency between centrality estimators is ensured due to the cut on the centrality estimator correlation. The next two variations are the opening on the cuts on the correlation between the centrality and multiplicity estimates. Opening these cuts gives access to a few more events where the correlations are not as consistent as before, but their influence is rather small. The variation on the cut on $\mathbf{V}_Z$ gives access to a substantial amount of more events. Though, since the primary vertex is quite out of the center of the detector, the quality of the tracks is not as high.

4.4.2. Variation of track cuts

The variations of all track cuts are listed in table 4.6. Shrinking the acceptance for DCA_Z and DCA_{XY} increases the quality of the data sample while reducing the amount of statistics. But since the distributions are mainly Gaussian, as shown in fig. 4.9, and we vary the cut in the tails, the impact is not large. The same can be said for the variations of n_{TPC}. The distribution is also shown in fig. 4.9 and is takes the from of a Poisson distribution and we vary the cut in the tail. The variation of the Filterbit has the largest impact. Since a Filterbit is a collection of cuts changing the Filterbits means that we change multiple cuts at the same time. Furthermore, the default cuts have been carefully chosen in accordance to Filterbit 128 to give a flat centrality and φ-distribution and they do not necessarily work for other Filterbits. The φ-distributions of the whole data set in centrality bin 40 % to 50 % after applying all track cuts and for all variation of the Filterbit according to table 4.6 are shown in fig. 4.12. The φ-distribution is only flat for the default Filterbit 128. For this reason we only include the variation of the Filterbit in the systematic checks in the case where we compute our observables with weights.

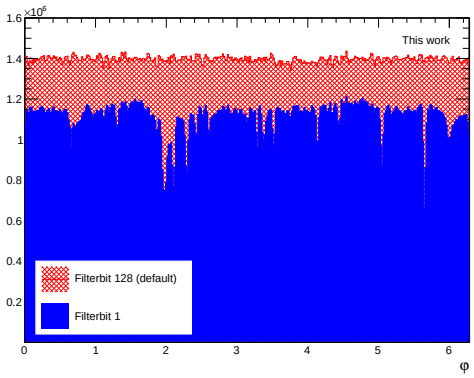

(a) Filterbit 1.

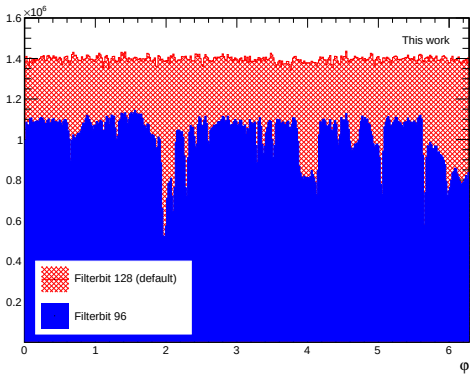

(b) Filterbit 96.

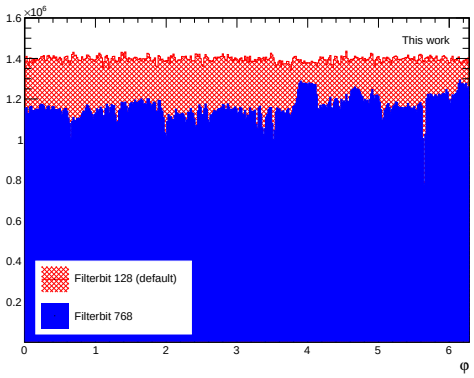

(c) Filterbit 768.

Figure 4.12.: φ-distribution of the whole data set in centrality bin 40 % to 50 % after applying all track cuts for different variations of the Filterbit compared to the default Filterbit.

5. Data Analysis

In this chapter we present the results of the differential studies of SC(2,3), SC(2,4) and SC(2,3,4), in sections 5.1 to 5.3 respectively, using Pb–Pb collision data taken by the LHC Run 1 in 2010 with the ALICE detector at $\sqrt{s_{\mathrm{NN}}} = 2.76\,\mathrm{TeV}$. The SCs are first shown as a function of centrality, which gives an indication of the strength of the fluctuations between the respective flow amplitudes in the corresponding centrality bin. Then we present, for the very first time, the transverse momentum and pseudorapidity dependence of the SCs in each centrality bin separately. Unless otherwise indicated, error bars represent statistical uncertainties, colored boxes the systematical uncertainties and vertical bars indicate the bin width. Statistical uncertainties are computed using the Bootstrap method introduced in section 2.8 and systematic uncertainties are computed using the systematic variations discussed in section 4.4.
We use the binning in centrality, transverse momentum and pseudorapidity described in table 5.1. The bins have been chosen such that the number of particles within one bin is

Table 5.1.: Binning of centrality, transverse momentum and pseudorapidity for the differential study of SC(2,3), SC(2,4) and SC(2,3,4)

	bins
centrality [%]	$(0.0; 5.0)$, $(5.0; 10)$, $(10; 20)$, $(20; 30)$ $(30; 40)$, $(40; 50)$, $(50; 60)$
p_{T} [GeV/c]	$(0.20; 0.34)$, $(0.34; 0.50)$, $(0.50; 0.70)$, $(0.70; 1.0)$, $(1.0; 2.0)$
η	$(-0.80; -0.40)$, $(-0.40; 0.0)$, $(0.0; 0.40)$, $(0.40; 0.80)$

large enough that the use of multiparticle correlation techniques is feasible and the result is not dominated by statistical uncertainties. The number of particles in the separate bins are also comparable to each other. We omit results for a centrality larger than 60 %, i.e. for peripheral collisions, because the results are unstable and have huge associated uncertainties, meaning there are not enough statistics to make useful statements in these centrality bins.
We present the results of the analysis with and without the use of weights as described in section 2.9 and section 4.3. The data taking conditions during Run 1 in 2010 were optimal and so we are able to obtain a flat φ- and centrality distribution after applying all cuts, as was demonstrated in chapter 4. This makes the use of weights almost unnecessary, except for the detector inefficiencies at small and large p_{T}. Since most of the results for p_{T} larger than $2.0\,\mathrm{GeV}/c$ were unstable and had huge uncertainties, we will only present results up to this value of transverse momentum. The usage of weights can also

be interpreted as another systematic variation of the analysis. This means the effects of weights on the result can be added to the systematic uncertainties and not interpreted as the baseline, i.e. unweighted, results. In this spirit, we present both results along side each other, demonstrating in which circumstances the use of weights only has a marginal impact on the baseline results.
The results obtained by the analysis performed on the data is additionally compared to the results obtained by performing the identical analysis on HIJING data generated in 2011 anchored to the original detector conditions of Run 1. HIJING[9, 37] is a widely used Monte Carlo generator designed for the studies of jet and multiparticle production in high energy nuclear collisions. It contains description of mechanism like jet quenching, multiple minijet production, soft beamjets, a parton structure dependent on the impact parameter of the collisions and more. While all these make HIJING a splendid prediction and analysis tool for nuclear physics in general, its role in flow analysis is slightly different. Firstly, as we have demonstrated in section 4.3, we can use the generated Monte Carlo data to obtain weights to correct the analysis for detector inefficiencies. Secondly, all the mechanism implemented in HIJING introduce correlations only between a few particles in the system. Therefore flow, which is a collective effect between all produced particles, is not present in HIJING and therefore it can be used to test the robustness of the observables and analysis techniques against non-flow. In particular, if we compare the results of the analysis performed on the data with the results of the analysis performed on the Monte Carlo data and we can see a signal in the data but not in the Monte Carlo data, this means that our analysis framework successfully isolated the flow signature and that we can suppress the contributions of non-flow.
The analysis code developed and used in this thesis is based on the AliRoot framework developed by the ALICE collaboration. The AliRoot framework itself is open source and publicly available and the analysis code for this thesis, which is now part of this framework, is encapsulated in the class *AliAnalysisTaskAR(.h,.cxx)* and can be found in the Github repository `https://github.com/alisw/AliPhysics/blob/master/PWG/FLOW/Tasks/`. For the analysis itself the computational resources provided by the ALICE collaboration, also known as the Grid, have been used. Additionally, we created another repository containing code to automate the submission, monitoring and other tasks related to running jobs on the Grid. The repository is also open source and publicly available on Github and can be found with `https://github.com/ariedel-cern/GridUtilityScripts`.

5.1. Experimental results for SC(2,3)

5.1.1. Centrality dependence of SC(2,3)

Figure 5.1 illustrates the centrality dependence of SC(2,3) from 0.0 % up to 60 % centrality. The results obtained using the HIJING data is consistent with zero within its

uncertainties in all centrality bins. The results using the ALICE data are non-zero and show that SC(2,3) is negative and increases in magnitude with centrality. Using HIJING for comparison we see that SC(2,3) is able to isolate the flow signal in the data and extract the correlation between v_2^2 and v_3^2. The result is also consistent with a previous measurement of SC(2,3) presented in [20]. We also observe that the correlations decrease when we perform the analysis with particle weights. Back in fig. 4.11a we demonstrated that the detectors have difficulties with detecting particles with small transverse momenta. Meaning these particles will have a larger weight associated with them in the computation of multiparticle correlators. Considering the results for the transverse momentum dependence, shown in figs. 5.2 to 5.3, we also see that, generally, the magnitude of SC(2,3) is diminishing at small transverse momenta. In total, that means we give more weight to particles which contribute less to the integrated value of SC(2,3), explaining why including weights in the computation decreases the value for SC(2,3).

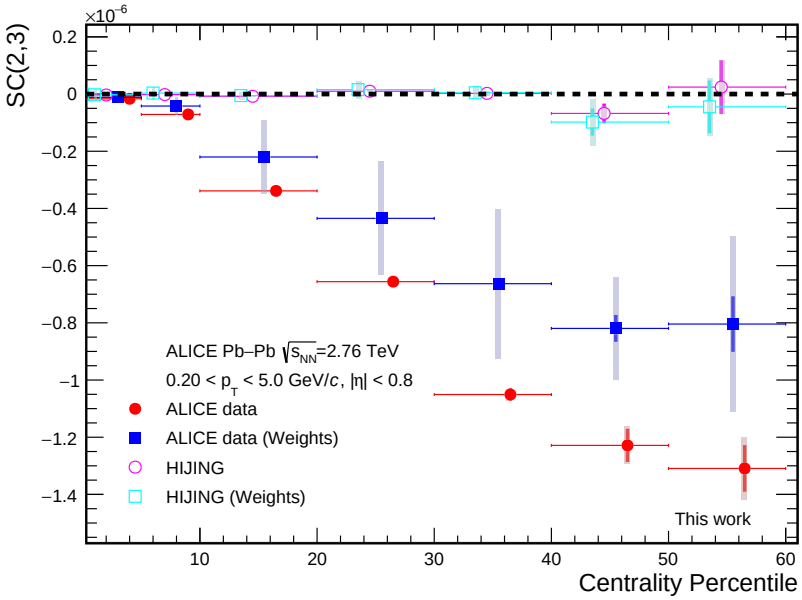

Figure 5.1.: Centrality dependence of SC(2,3). The red and blue markers show the unweighted and weighted result using the ALICE data respectively. The magenta and the cyan markers show the unweighted and weighted result using the HIJING data respectively.

5.1.2. p_{T}-dependence of SC(2,3)

In figs. 5.2 to 5.3 SC(2,3) is displayed as a function of transverse momentum from 0.20 GeV/c to 2.0 GeV/c in each centrality bin individually. Overall, we see that the

HIJING result is compatible with zero in all p_{T}-bins in all centrality classes while we observe non-zero values for SC(2,3) in the ALICE data. This means within the p_{T}-bins we are still able to extract the flow signal reliably. Generally, within each centrality class, we see that SC(2,3) is negative and its magnitude increases strongly with the transverse momentum. Furthermore, the larger the centrality class, the larger the values of SC(2,3) get. For examples, the value of SC(2,3) in the p_{T}-bin 1.0 GeV/c to 2.0 GeV/c in centrality bin 0.0 % to 5.0 % is approximately -0.2×10^{-6} while in centrality bin 50 % to 60 % its value is approximately -30×10^{-6}. This is an increase by two orders of magnitude. Another observation is that the unweighted and weighted results are compatible with each other and we do not see a similar difference as in the centrality dependence. Once again, looking back at fig. 4.11a, the weights are flat for p_{T} between 0.50 GeV/c and 2.0 GeV/c. This means they only have a small impact on the result in this range. And since the magnitude of SC(2,3) is small at small p_{T} and we plot the values for the whole range we do not see the deviation in the first two bins. This results in an overall agreement between the unweighted and weighted results.

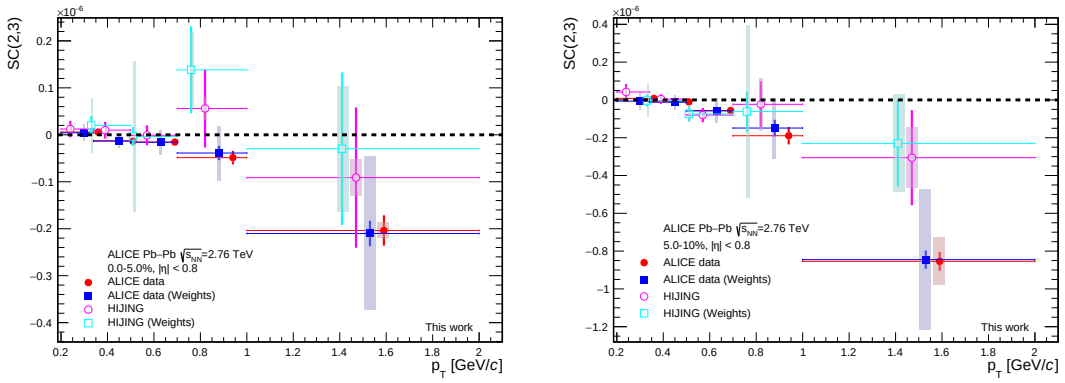

(a) p_{T}-dependence of SC(2,3) in centrality bin 0.0 % to 5.0 %.

(b) p_{T}-dependence of SC(2,3) in centrality bin 5.0 % to 10 %.

Figure 5.2.: p_{T}-dependence of SC(2,3) in centrality 0.0 % to 10 %. The red and blue markers show the unweighted and weighted result using the ALICE data respectively. The magenta and the cyan markers show the unweighted and weighted result using the HIJING data respectively.

5.1.3. η-dependence of SC(2,3)

In figs. 5.4 to 5.5 SC(2,3) is displayed as a function of pseudorapidity from -0.80 to 0.80 in each centrality bin individually. Once again, we see that overall the HIJING result is compatible with zero within the uncertainty and we observe non-zero values for SC(2,3) for centrality larger than 10 % and smaller than 50 %. All in all, the η-dependence of

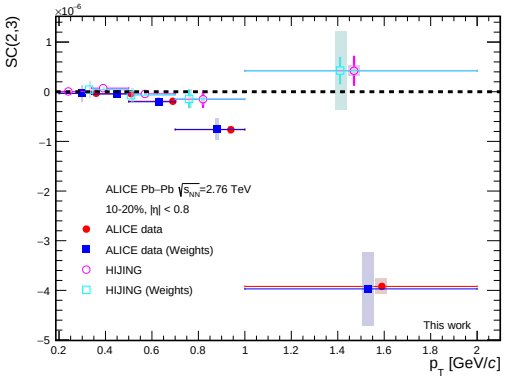

(a) p_{T}-dependence of SC(2,3) in centrality bin 10 % to 20 %.

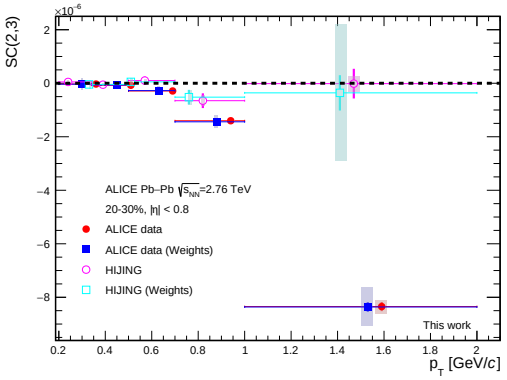

(b) p_{T}-dependence of SC(2,3) in centrality bin 20 % to 30 %.

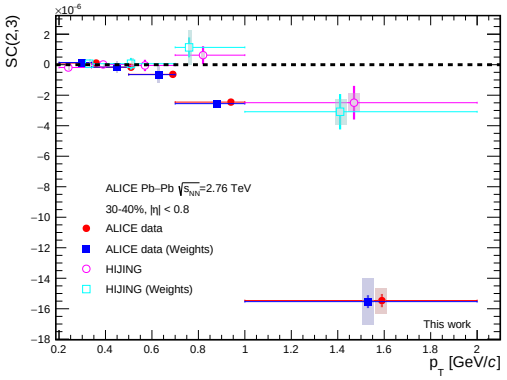

(c) p_{T}-dependence of SC(2,3) in centrality bin 30 % to 40 %.

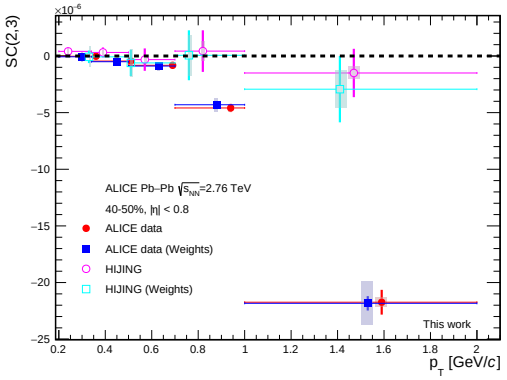

(d) p_{T}-dependence of SC(2,3) in centrality bin 40 % to 50 %.

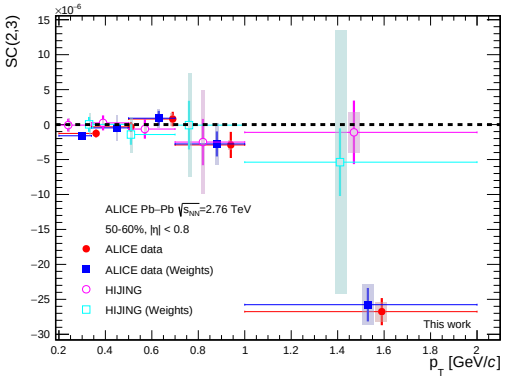

(e) p_{T}-dependence of SC(2,3) in centrality bin 50 % to 60 %.

Figure 5.3.: p_{T}-dependence of SC(2,3) in centrality 10 % to 60 %. The red and blue markers show the unweighted and weighted result using the ALICE data respectively. The magenta and the cyan markers show the unweighted and weighted result using the HIJING data respectively.

SC(2,3) is flat and we do not see a non-trivial dependence as we have observed for p_{T}. Furthermore, compared to the p_{T}-dependence, while the values of SC(2,3) inside the η-bins increase for higher centrality, the order of the values does not change dramatically. In centrality bin 10 % to 20 % the weighted result is approximately -0.2×10^{-6} in all η-bins while in centrality bin 40 % to 50 % it is approximately -1×10^{-6}. These values are in the same order compared to the observed difference of two orders in the case of p_{T} dependence. Lastly, as was the case with the integrated result of SC(2,3), the weighted results are smaller than the unweighted results, independent of centrality and η-bin. This indicates that there is no correlation between the p_{T}- and η-dependence and all η-bins are affected equally by the usage of the p_{T}-weights.

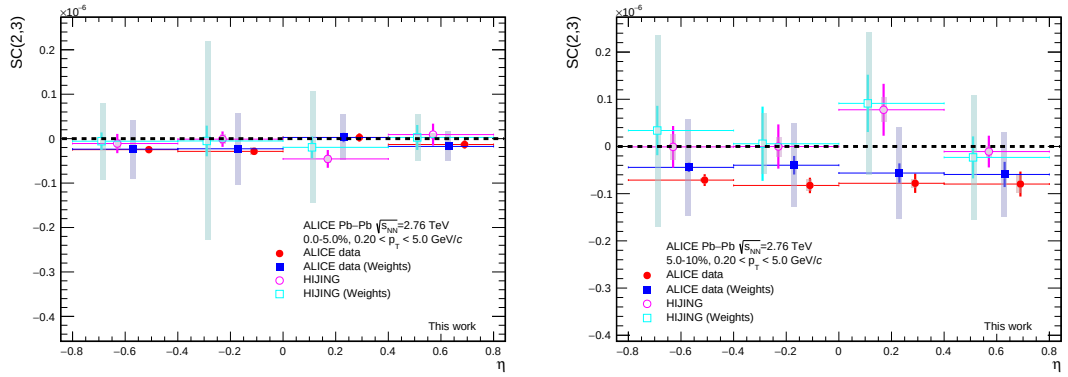

(a) η-dependence of SC(2,3) in centrality bin 0.0 % to 5.0 %.

(b) η-dependence of SC(2,3) in centrality bin 5.0 % to 10 %.

Figure 5.4.: η-dependence of SC(2,3) in centrality 10 % to 60 %. The red and blue markers show the unweighted and weighted result using the ALICE data respectively. The magenta and the cyan markers show the unweighted and weighted result using the HIJING data respectively.

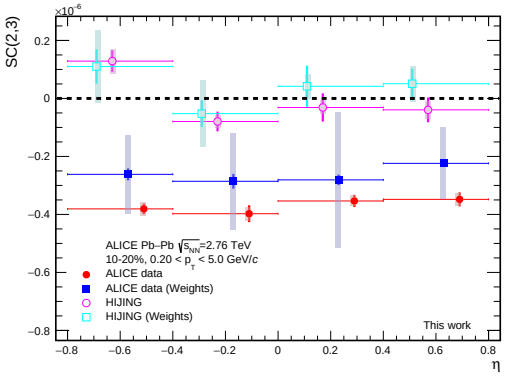

(a) η-dependence of SC(2,3) in centrality bin 10 % to 20 %.

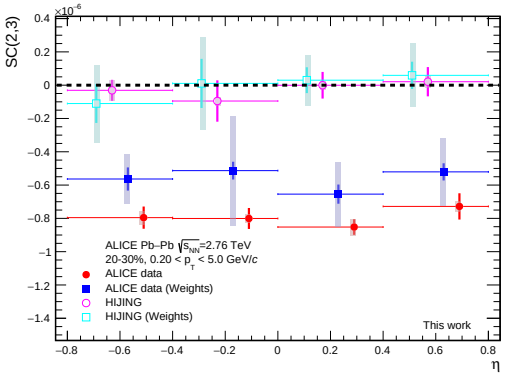

(b) η-dependence of SC(2,3) in centrality bin 20 % to 30 %.

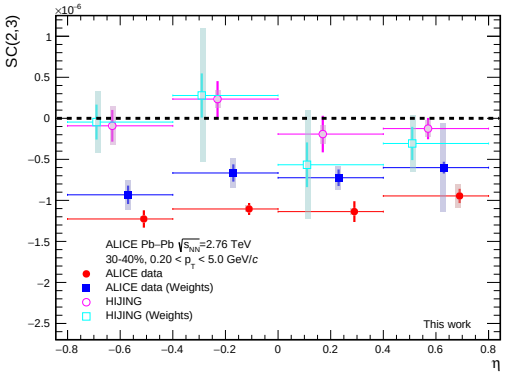

(c) η-dependence of SC(2,3) in centrality bin 30 % to 40 %.

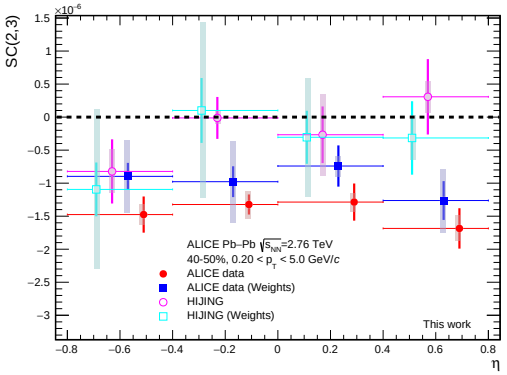

(d) η-dependence of SC(2,3) in centrality bin 40 % to 50 %.

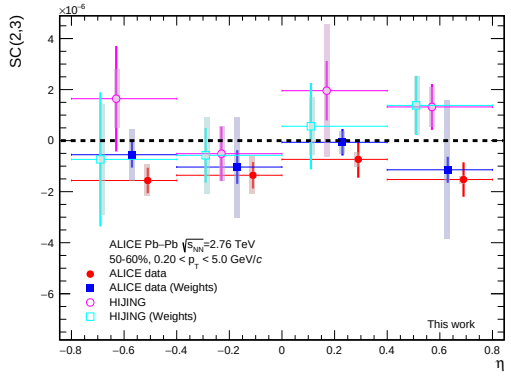

(e) η-dependence of SC(2,3) in centrality bin 50 % to 60 %.

Figure 5.5.: η-dependence of SC(2,3) in centrality 10 % to 60 %. The red and blue markers show the unweighted and weighted result using the ALICE data respectively. The magenta and the cyan markers show the unweighted and weighted result using the HIJING data respectively.

5.2. Experimental results for SC(2,4)

5.2.1. Centrality dependence of SC(2,4)

In fig. 5.6 the centrality dependence of SC(2,4) from 0.0 % to 60 % is shown. We find again that the HIJING result is compatible with zero while the result using ALICE data is non-zero confirming that we manage to extract the flow signal and the correlation between v_2^2 and v_4^2. The value of SC(2,4) is positive and it increases with centrality. This is also consistent with a previous measurement presented in [20]. We also observe again that the values of SC(2,4) decreases when we use weights during the analysis. We can use the same argument as the one we used for SC(2,3) to explain this circumstance. This is justified because if we look at the p_{T}-dependence of SC(2,4) in figs. 5.7 to 5.8, we observe overall the same behavior as for SC(2,3) with a opposite sign.

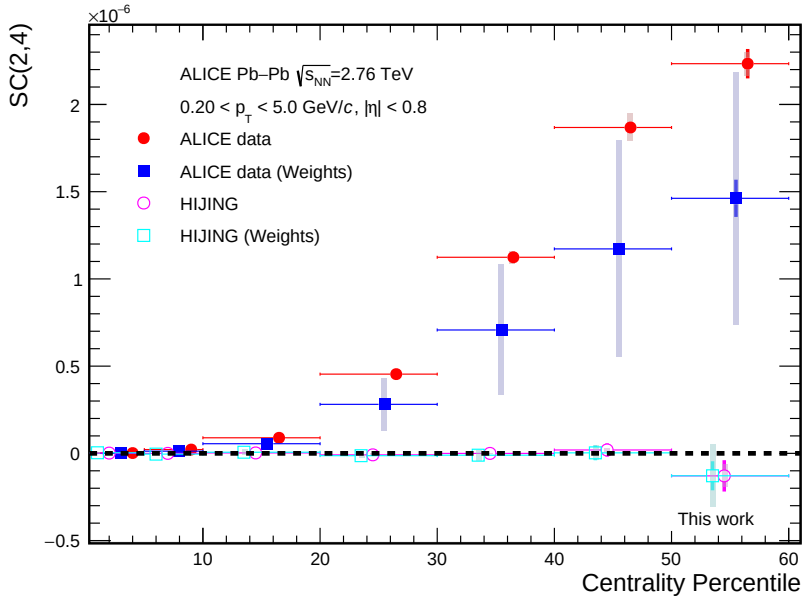

Figure 5.6.: Centrality dependence of SC(2,4).

5.2.2. p_{T}-dependence of SC(2,4)

In figs. 5.7 to 5.8 SC(2,4) is displayed as a function of transverse momentum from 0.20 GeV/c to 2.0 GeV/c in each centrality bin individually. We mainly see that the weighted and unweighted HIJING results are compatible with zero, indicating that we

manage to suppress the non-flow contribution within the p_{T}-bins for all centrality classes reliably. The flow signal is very weak in centrality bin 0.0 % to 5.0 %, where the values of SC(2,4) computed using the data is compatible with zero in each p_{T}-bin. Though the values do increase strongly with centrality and with p_{T}. The order of the values also changes drastically. While the largest value of SC(2,4) in p_{T}-bin 1.0 GeV/c to 2.0 GeV/c is approximately 1×10^{-6} in 10 % to 20 %, the largest value in 50 % to 60 % is roughly 35×10^{-6}. This is again almost an increase of two orders of magnitude.

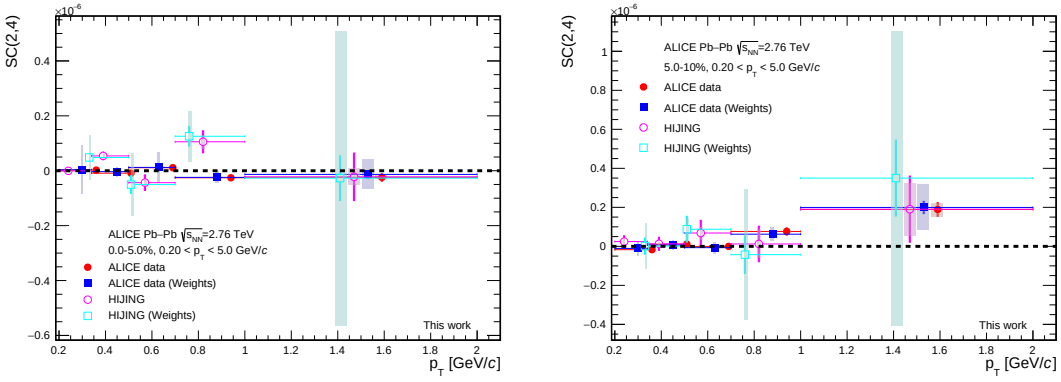

(a) p_{T}-dependence of SC(2,4) in centrality bin 0.0 % to 5.0 %.

(b) p_{T}-dependence of SC(2,4) in centrality bin 5.0 % to 10 %.

Figure 5.7.: p_{T}-dependence of SC(2,4) in centrality 0.0 % to 10 %. The red and blue markers show the unweighted and weighted result using the ALICE data respectively. The magenta and the cyan markers show the unweighted and weighted result using the HIJING data respectively.

5.2.3. η-dependence of SC(2,4)

In figs. 5.9 to 5.10 SC(2,4) is displayed as a function of pseudorapidity from -0.80 to 0.80 in each centrality bin individually. Overall, the HIJING result is again compatible with zero within the uncertainty and we observe non-zero values for SC(2,4) for centrality bins larger than 20 %. In total, the η-dependence of SC(2,4) is flat and we do not see a non-trivial dependence similar to what we observed for p_{T}. Also, the order of the values does not change. In centrality bin 20 % to 30 % the weighted result is approximately 0.5×10^{-6} in all η-bins while in centrality bin 50 % to 60 % it is approximately 4×10^{-6}. And, as was the case with the integrated result of SC(2,4), the weighted results are smaller than the unweighted results, independent of centrality and η-bin. This also indicates that there is no correlation between the p_{T}- and η-dependence of SC(2,4).

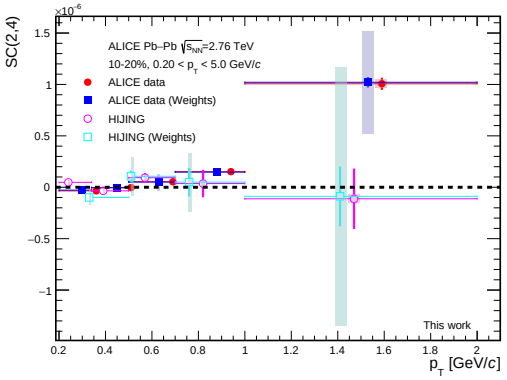

(a) p_{T}-dependence of SC(2,4) in centrality bin 10 % to 20 %.

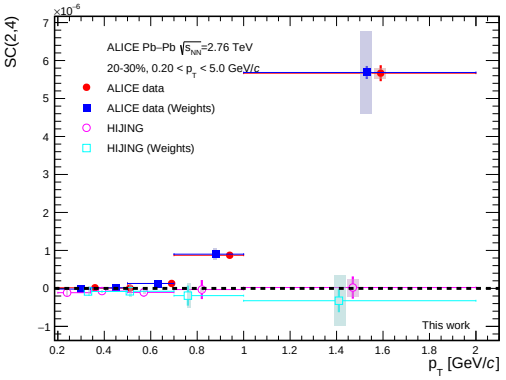

(b) p_{T}-dependence of SC(2,4) in centrality bin 20 % to 30 %.

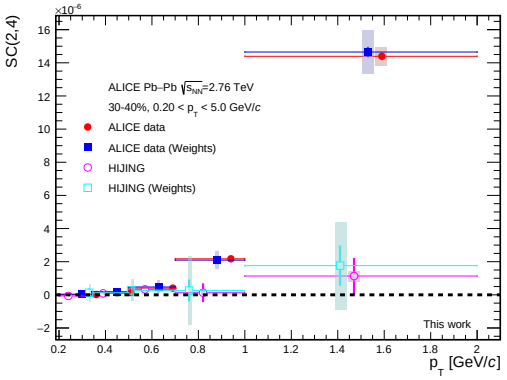

(c) p_{T}-dependence of SC(2,4) in centrality bin 30 % to 40 %.

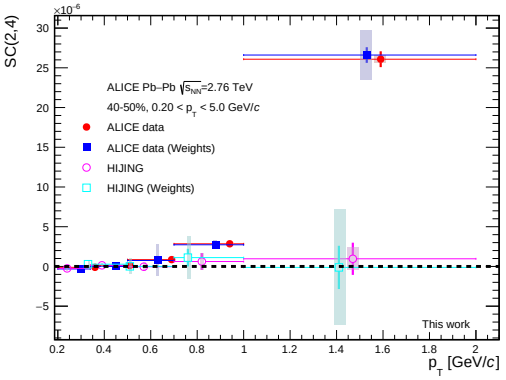

(d) p_{T}-dependence of SC(2,4) in centrality bin 40 % to 50 %.

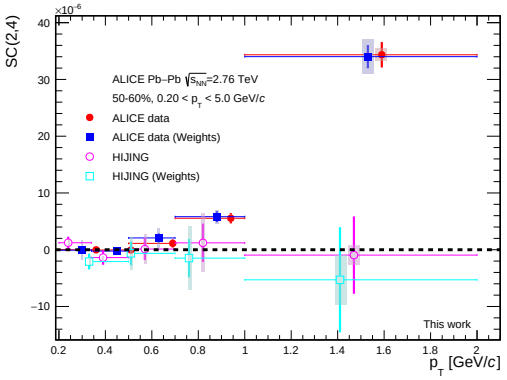

(e) p_{T}-dependence of SC(2,4) in centrality bin 50 % to 60 %.

Figure 5.8.: p_{T}-dependence of SC(2,4) in centrality 10 % to 60 %. The red and blue markers show the unweighted and weighted result using the ALICE data respectively. The magenta and the cyan markers show the unweighted and weighted result using the HIJING data respectively.

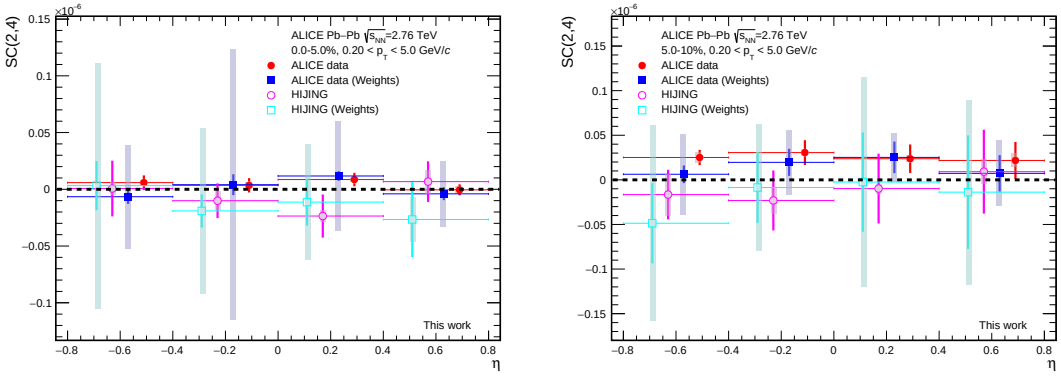

(a) η-dependence of SC(2,4) in centrality bin 0.0 % to 5.0 %.

(b) η-dependence of SC(2,4) in centrality bin 5.0 % to 10 %.

Figure 5.9.: η-dependence of SC(2,4) in centrality 0.0 % to 10 %. The red and blue markers show the unweighted and weighted result using the ALICE data respectively. The magenta and the cyan markers show the unweighted and weighted result using the HIJING data respectively.

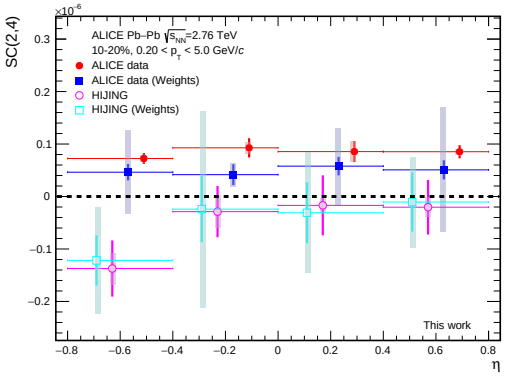

(a) η-dependence of SC(2,4) in centrality bin 10 % to 20 %.

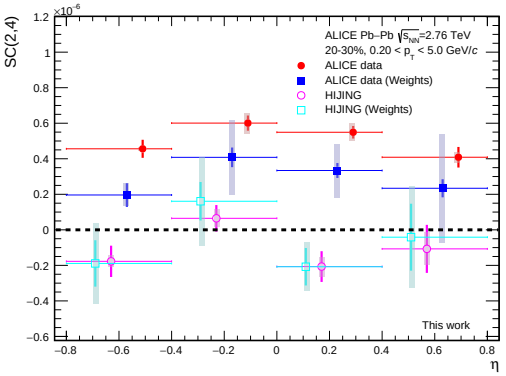

(b) η-dependence of SC(2,4) in centrality bin 20 % to 30 %.

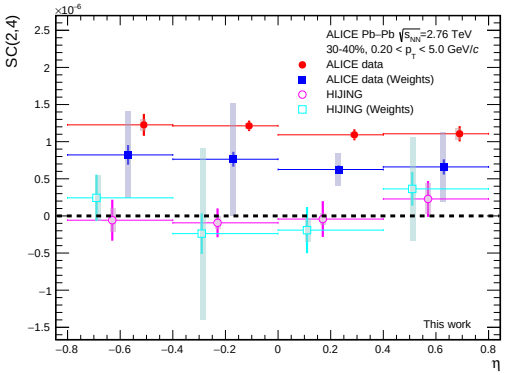

(c) η-dependence of SC(2,4) in centrality bin 30 % to 40 %.

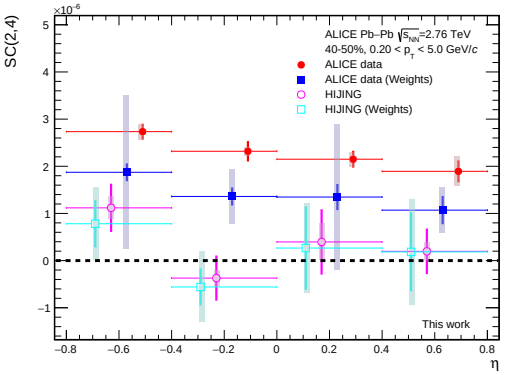

(d) η-dependence of SC(2,4) in centrality bin 40 % to 50 %.

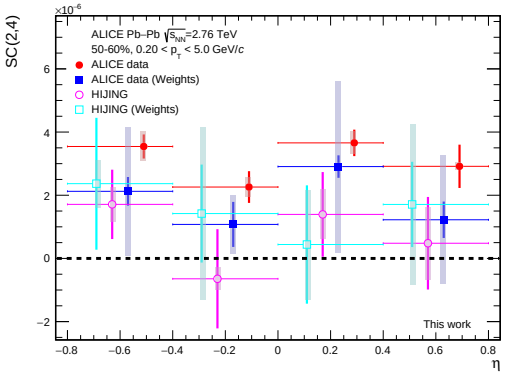

(e) η-dependence of SC(2,4) in centrality bin 50 % to 60 %.

Figure 5.10.: η-dependence of SC(2,4) in centrality 10 % to 60 %. The red and blue markers show the unweighted and weighted result using the ALICE data respectively. The magenta and the cyan markers show the unweighted and weighted result using the HIJING data respectively.

5.3. Experimental results for SC(2,3,4)

5.3.1. Centrality dependence of SC(2,3,4)

Figure 5.11 illustrates the centrality dependence of SC(2,3,4) from 0.0 % to 50 % centrality. We exclude the result for centrality bin 50 % to 60 % because of its huge statistical uncertainty. The result using HIJING data is consistent with zero in all centrality bins and the one using ALICE is non-zero for centrality larger than 30 %. Hence we are able to suppress the non-flow contributions and isolate the correlation between the flow amplitudes v_2^2, v_3^2 and v_4^2. In total, the value of SC(2,3,4) is negative and its magnitude of SC(2,3,4) increases with centrality. The result is also consistent with a previous measurement of SC(2,3,4) presented in [20].

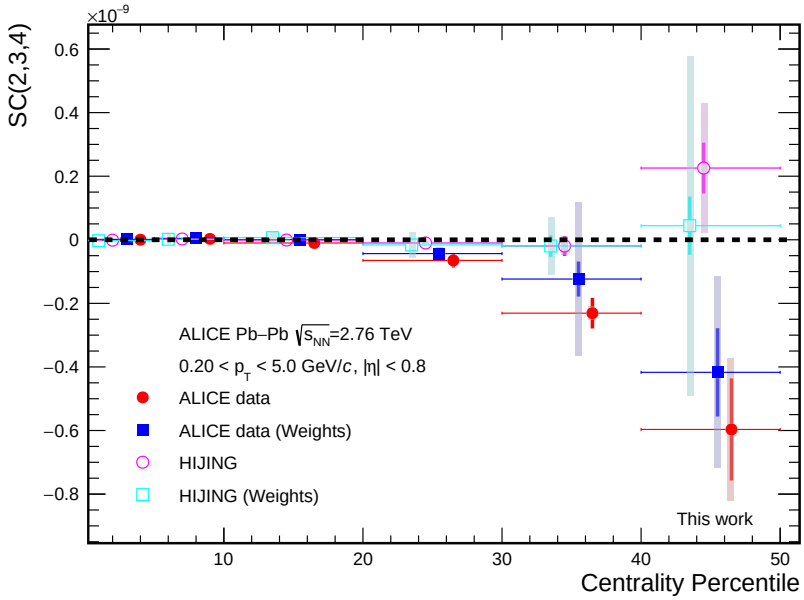

Figure 5.11.: Centrality dependence of SC(2,3,4).

5.3.2. p_{T}-dependence of SC(2,3,4)

The results of the measurements of the transverse momentum dependence of SC(2,3,4) are shown in fig. 5.12. While the HIJING results are again compatible with zero, so are the results using ALICE data. Considering the results for the centrality dependence only, a non-zero results would have been expected for centrality larger than 30 %. But even in

the centrality bins 30 % to 40 % and 40 % to 50 % we do not find a result in any p_{T}-bin where the value of SC(2,3,4) is significantly different from zero. Therefore, we have to conclude that the statistics available in the Run 1 data set from 2010 is not sufficient to extract the transverse momentum dependence of SC(2,3,4) with the chosen binning.

5.3.3. η-dependence of SC(2,3,4)

The results of the measurements of the pseudorapidity dependence of SC(2,3,4) are shown in fig. 5.12. As has been the case for all results so far, the HIJING results are again compatible with zero. Unfortunately, the results using the ALICE data are also compatible with zero, as was the case for the p_{T} dependence. Meaning, we have to conclude that the statistics available in the Run 1 data set from 2010 is not sufficient to extract the pseudorapidity dependence of SC(2,3,4) with the chosen binning.

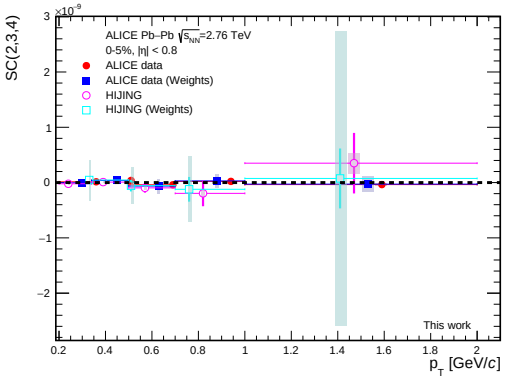

(a) p_T-dependence of SC(2,3,4) in centrality bin 0.0 % to 5.0 %.

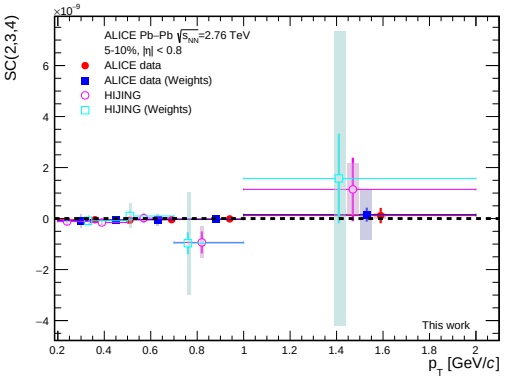

(b) p_T-dependence of SC(2,3,4) in centrality bin 5.0 % to 10 %.

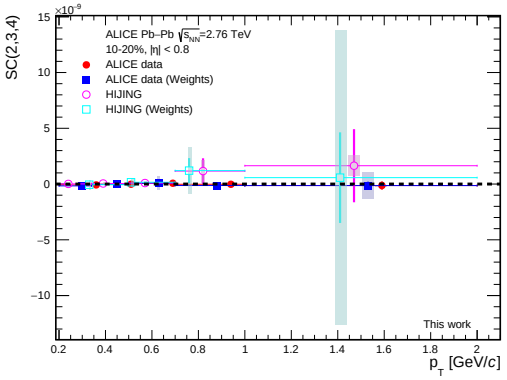

(c) p_T-dependence of SC(2,3,4) in centrality bin 10 % to 20 %.

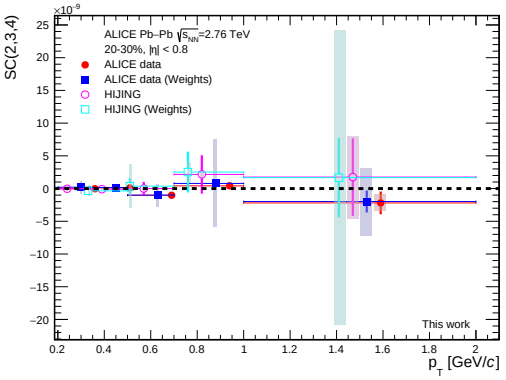

(d) p_T-dependence of SC(2,3,4) in centrality bin 20 % to 30 %.

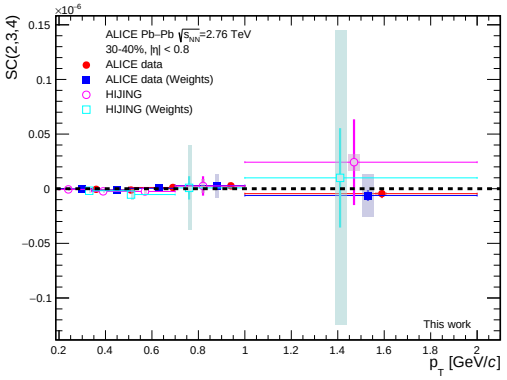

(e) p_T-dependence of SC(2,3,4) in centrality bin 30 % to 40 %.

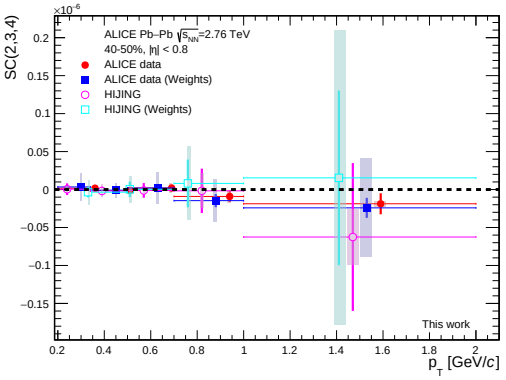

(f) p_T-dependence of SC(2,3,4) in centrality bin 40 % to 50 %.

Figure 5.12.: p_T-dependence of SC(2,3,4) in different centrality bins. The red and blue markers show the unweighted and weighted result using the ALICE data respectively. The magenta and the cyan markers show the unweighted and weighted result using the HIJING data respectively.

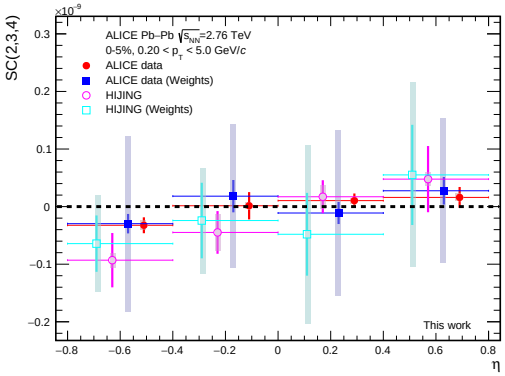

(a) η-dependence of SC(2,3,4) in centrality bin 0.0 % to 5.0 %.

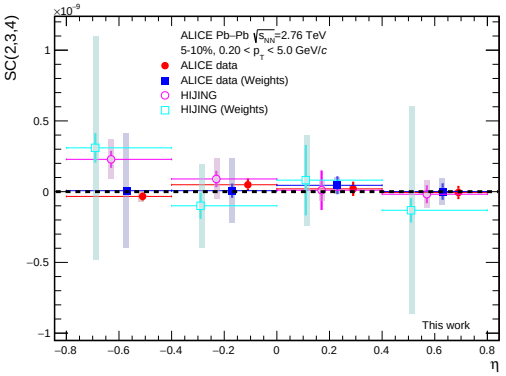

(b) η-dependence of SC(2,3,4) in centrality bin 5.0 % to 10 %.

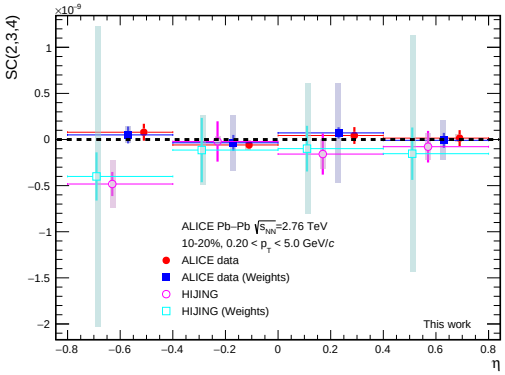

(c) η-dependence of SC(2,3,4) in centrality bin 10 % to 20 %.

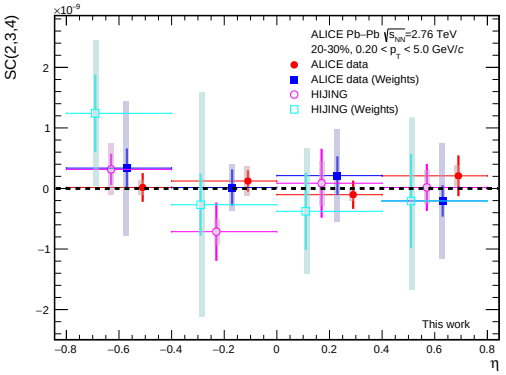

(d) η-dependence of SC(2,3,4) in centrality bin 20 % to 30 %.

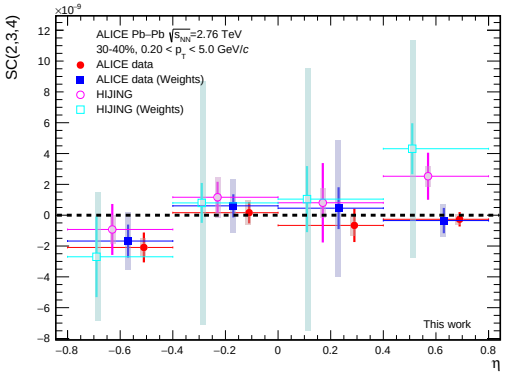

(e) η-dependence of SC(2,3,4) in centrality bin 30 % to 40 %.

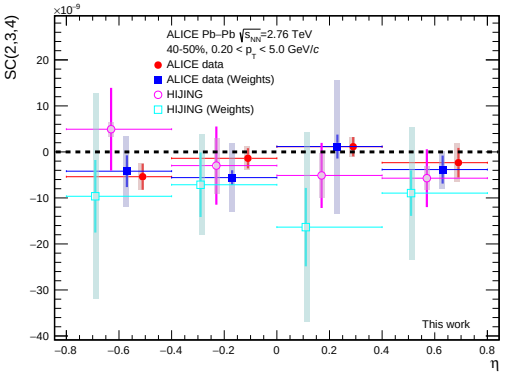

(f) η-dependence of SC(2,3,4) in centrality bin 40 % to 50 %.

Figure 5.13.: η-dependence of SC(2,3,4) in different centrality bins. The red and blue markers show the unweighted and weighted result using the ALICE data respectively. The magenta and the cyan markers show the unweighted and weighted result using the HIJING data respectively.

6. Summary

This thesis presents for the first time the measurements of transverse momentum and pseudorapidity dependence of Symmetric Cumulants SC(2,3), SC(2,4) and SC(2,3,4). This thesis also confirmed the established results for the centrality dependence of SC(2,3), SC(2,4) and SC(2,3,4) presented in [20]. These differential studies give new and independent information about the correlations between v_2^2, v_3^2 and v_3^2 and can be used to further constrain the properties of the Quark-Gluon Plasma.
For the computation of the SCs we use the generic framework introduced in [4]. We start by factorizing the joined probability density function of the azimuthal angles of the particles produced in a heavy-ion collision and expanding each marginal probability density function as a Fourier Series. These Fourier Series are parameterized, in each order n, by the flow amplitudes v_n and symmetry plane Ψ_n. The properties of the Quark-Gluon Plasma are encoded in the values of the different v_n and their mutual correlations. Using multiparticle correlation techniques we can estimate the value of flow harmonics by computing multiparticle correlators. Computing multiparticle correlators straight forwardly, i.e. with the use of nested loops over the data, is computationally not feasible. Therefore we use Q-vectors, which allow to obtain an analytically equivalent result passing over the data only once. Using this machinery, we can estimate the values of flow harmonics on an event-by-event basis.
The factorization of the joined probability density function of azimuthal angels is only valid if flow is the only physical effect which produces correlations among the generated particles, which is in general not the case. These effects are called non-flow and they introduce correlation between a subset of particles. For this reason we need an additional tool to estimate the expectation value of the flow harmonics from the event-by-event estimates that suppresses non-flow. This can be achieved with the use of cumulants. Cumulants can quantify the genuine correlation between all particles and therefore suppress the contribution from effects that only effect a subset of particles. If we evaluate a cumulant only in one harmonic n we can use it to estimate the expectation value of v_n. Symmetric cumulants are a special kind of cumulants where we evaluate the cumulant in at least two different harmonics n and m to estimate the correlation between v_n^2 and v_m^2. The same is true for higher order Symmetric cumulants that can measure the correlations between more flow harmonics.
This thesis uses Pb–Pb collision data taken by LHC Run 1 in 2010 with the ALICE detector at $\sqrt{s_{\mathrm{NN}}} = 2.76\,\mathrm{TeV}$. The experimental results in this thesis for SC(2,3) show that, integrated over the different centrality bins, it is negative and its magnitude increases with centrality. The same general behavior is observed for SC(2,3,4) while SC(2,4) is positive

and its magnitude also increases with centrality. The measurement of the transverse momentum dependence of SC(2,3) shows a non-trivial behavior. The value of SC(2,3) increases steadily with the transverse momentum in each centrality bin. The overall magnitude of the values of SC(2,3) within a centrality bin also increases sharply with the centrality. The same can be said for SC(2,4), but with an opposite sign. For SC(2,3,4) we do not observe any dependence due to the uncertainties. The available statistics are not sufficient to extract the transverse momentum dependence of SC(2,3,4). The pseudorapidity dependence of SC(2,3) and SC(2,4) is flat, i.e. they are constant. The statistics are also, regrettably, insufficient to extract the dependence of SC(2,3,4) on pseudorapidity.
The results have been validated by comparing them to results obtained by performing the exact same analysis on a HIJING data set which was anchored to the real data set. HIJING is a Monte Carlo event generator which implements all know physical effects present in heavy-ion collision except for flow. Therefore, performing the analysis on this data set should consistently yield a result compatible with zero in all bins because there are no correlation due to flow. The HIJING results have been consistently zero for all centrality, transverse momentum and pseudorapidity bins.
These measurements have been the first look at differential studies of Symmetric Cumulants. While the measurements have been able to extract the dependence of transverse momentum and pseudorapidity for SC(2,3) and SC(2,4), the binning was very coarse. Despite that, the statistics were not enough to make any statement about the dependence of SC(2,3,4). With the future increases of energy and luminosity in Run 3 of the LHC we will be able to study the dependence of three and higher order Symmetric cumulants and use a finer binning.

A. Derivations

In this Chapter we will outline the detailed mathematical proofs for the statements made in this thesis.

A.1. Fourier Coefficients of normalized linear function

The normalized linear function on the interval $[0, 2\pi]$ reads

$$f(\varphi) = \frac{1}{2\pi^2}\varphi\,. \tag{A.1}$$

Using eqs. (2.2) and (2.3) we can compute the coefficients of its Fourier series as described in eq. (2.1). The derivation for c_n reads

$$\begin{aligned}
c_n &= \int_0^{2\pi} \mathrm{d}\varphi f(\varphi) \cos(n\varphi)\,, && \text{(A.2)}\\
&= \frac{1}{2\pi^2} \int_0^{2\pi} \mathrm{d}\varphi\varphi \cos(n\varphi)\,, && \text{(A.3)}\\
&= \frac{1}{2\pi^2} \left[\frac{\varphi}{n} \sin(n\varphi) \Big|_0^{2\pi} - \frac{1}{n} \int_0^{2\pi} \mathrm{d}\varphi \sin(n\varphi) \right]\,, && \text{(A.4)}\\
&= \frac{1}{2\pi^2} \left[\frac{1}{n^2} \cos(n\varphi) \Big|_0^{2\pi} \right]\,, && \text{(A.5)}\\
&= 0\,. && \text{(A.6)}
\end{aligned}$$

The derivation for s_n looks similar and reads

$$s_n = \int_0^{2\pi} \mathrm{d}\varphi f(\varphi) \sin(n\varphi) \,, \tag{A.7}$$

$$= \frac{1}{2\pi^2} \int_0^{2\pi} \mathrm{d}\varphi\varphi \sin(n\varphi) \,, \tag{A.8}$$

$$= \frac{1}{2\pi^2} \left[-\frac{\varphi}{n} \cos(n\varphi) \Big|_0^{2\pi} + \frac{1}{n} \int_0^{2\pi} \mathrm{d}\varphi \cos(n\varphi) \right] , \tag{A.9}$$

$$= \frac{1}{2\pi^2} \left[-\frac{2\pi}{n} + \frac{1}{n^2} \sin(n\varphi) \Big|_0^{2\pi} \right] , \tag{A.10}$$

$$= -\frac{1}{n\pi} \,. \tag{A.11}$$

Hence, the Fourier series is

$$f(\varphi) = \frac{1}{2\pi} \left[1 - \frac{2}{\pi} \sum_{n=1}^{\infty} \frac{\sin(n\varphi)}{n} \right] . \tag{A.12}$$

A.2. Parameterization of Fourier Series

In the following we want to show the equality between eq. (2.1) and eq. (2.6). For the equality to hold we will demonstrate that

$$c_n \cos(n\varphi) + s_n \sin(n\varphi) = v_n \cos[n(\varphi - \Psi_n)] \tag{A.13}$$

for all n and for a certain choice of v_n and Ψ_n. We start with the left hand side and rewrite the sine and cosine function as exponential functions and rearrange the terms resulting in

$$c_n \cos(n\varphi) + s_n \sin(n\varphi) = \frac{c_n}{2} \left(e^{in\varphi} + e^{-in\varphi} \right) + \frac{s_n}{2i} \left(e^{in\varphi} - e^{-in\varphi} \right) , \tag{A.14}$$

$$= \left(\frac{c_n}{2} + \frac{s_n}{2i} \right) e^{in\varphi} + \left(\frac{c_n}{2} - \frac{s_n}{2i} \right) e^{-in\varphi} \,, \tag{A.15}$$

$$= \frac{1}{2} \left[(c_n - is_n) e^{in\varphi} + (c_n + is_n) e^{-in\varphi} \right] . \tag{A.16}$$

$$\tag{A.17}$$

We can see that the factor in front of the first exponential is the complex conjugate of factor in front of the second exponential. If we define a complex number $\xi_n \in \mathbb{C}$ for each n as

$$\xi_n = c_n + is_n \tag{A.18}$$

then we receive

$$c_n \cos(n\varphi) + s_n \sin(n\varphi) = \frac{1}{2}\left[\xi_n^* e^{in\varphi} + \xi_n e^{-in\varphi}\right] . \tag{A.19}$$

Now we change the parameterization of ξ_n to polar coordinates in the complex plane to

$$\xi_n = v_n e^{in\Psi_n} , \tag{A.20}$$

where

$$v_n = \sqrt{c_n^2 + s_n^2} \tag{A.21}$$

and

$$\Psi_n = \frac{1}{n} \arctan \frac{s_n}{c_n} , \tag{A.22}$$

which gives us the parameterization of v_n and Ψ_n in terms of c_n and s_n. Plugging now eq. (A.20) into eq. (A.19) gives

$$c_n \cos(n\varphi) + s_n \sin(n\varphi) = \frac{1}{2}\left[v_n e^{-in\Psi_n} e^{in\varphi} + v_n e^{in\Psi_n} e^{-in\varphi}\right] , \tag{A.23}$$

$$= \frac{v_n}{2}\left[e^{in(\varphi-\Psi_n)} + e^{-in(\varphi-\Psi_n)}\right] , \tag{A.24}$$

$$= v_n \cos\left[n\left(\varphi - \Psi_n\right)\right] , \tag{A.25}$$

where we used the definition of the cosine function again as a sum of exponential functions and conclude the proof.

A.3. Symmetry properties of Fourier coefficients

In the definition of the Fourier Series in eq. (2.1) we sum over positive indices. It is also possible to define the sum over negative indices as well. We will not be using this definition but we still need to establish a relationship between coefficients c_n, s_n and c_{-n}, s_{-n} which also gives rise to a relationship between v_n, Ψ_n and v_{-n}, Ψ_{-n}. We reuse eqs. (2.2) to (2.3) and receive

$$c_{-n} = \int_0^{2\pi} \mathrm{d}\varphi f(\varphi) \cos(-n\varphi) = c_n \tag{A.26}$$

and

$$s_{-n} = \int_0^{2\pi} \mathrm{d}\varphi f(\varphi) \sin(-n\varphi) = -s_n . \tag{A.27}$$

where we exploited the symmetry properties of the sine and cosine function. Using these results and the parameterization given in eqs. (2.7) to (2.8) gives

$$\begin{aligned} v_{-n} &= \sqrt{c_{-n}^2 + s_{-n}^2}\,, && \text{(A.28)}\\ &= \sqrt{c_n^2 + (-s_n)^2}\,, && \text{(A.29)}\\ &= \sqrt{c_n^2 + s_n^2}\,, && \text{(A.30)}\\ &= v_n && \text{(A.31)} \end{aligned}$$

and

$$\begin{aligned} \Psi_{-n} &= \frac{1}{-n} \arctan \frac{s_{-n}}{c_{-n}}\,, && \text{(A.32)}\\ &= \frac{1}{-n} \arctan \frac{-s_n}{c_n}\,, && \text{(A.33)}\\ &= \frac{1}{n} \arctan \frac{s_n}{c_n}\,, && \text{(A.34)}\\ &= \Psi_n\,. && \text{(A.35)} \end{aligned}$$

A.4. Derivation of flow harmonics

In the following we will use these orthogonality relations:

$$\int_0^{2\pi} \mathrm{d}x \sin(mx+\alpha)\sin(nx+\beta) = \pi\cos(\alpha-\beta)\delta_{mn}\,, \tag{A.36}$$

$$\int_0^{2\pi} \mathrm{d}x \cos(mx+\alpha)\cos(nx+\beta) = \pi\cos(\alpha-\beta)\delta_{mn}\,, \tag{A.37}$$

$$\int_0^{2\pi} \mathrm{d}x \sin(mx+\alpha)\cos(nx+\beta) = \pi\sin(\alpha-\beta)\delta_{mn}\,. \tag{A.38}$$

We want to derive eq. (2.16). We start with eq. (2.6). By multiplying both sides with $\cos\left[n\left(\varphi - \Psi_n\right)\right]$ we receive

$$\begin{aligned} &\int_0^{2\pi} \mathrm{d}\varphi \cos\left[n\left(\varphi-\Psi_n\right)\right] f(\varphi) = \\ &\frac{1}{2\pi}\int_0^{2\pi} \mathrm{d}\varphi \cos\left[n\left(\varphi-\Psi_n\right)\right]\left[1 + 2\sum_{k=1}^{\infty} v_k \cos[k(\varphi-\Psi_k)]\right]\,. \end{aligned} \tag{A.39}$$

The left hand side is by definition the expectation value $\langle\cos\left[n\left(\varphi-\Psi_n\right)\right]\rangle$. It is left to show that the right hand side equals v_n. Multiplying out everything the right hand side

(RHS) results in

$$\begin{aligned} RHS = \frac{1}{2\pi}\Bigg[& \int_0^{2\pi} \mathrm{d}\varphi \cos\left[n\left(\varphi - \Psi_n\right)\right] \\ & + 2\int_0^{2\pi} \mathrm{d}\varphi \sum_{k=1}^{\infty} v_k \cos[k(\varphi - \Psi_k)] \cos[n(\varphi - \Psi_n)]\Bigg] . \end{aligned} \tag{A.40}$$

The first integral inside the bracket computes to

$$\int_0^{2\pi} \mathrm{d}\varphi \cos\left[n\left(\varphi - \Psi_n\right)\right] = \frac{1}{n} \sin\left[n\left(\varphi - \Psi_n\right)\right]\Big|_0^{2\pi} , \tag{A.41}$$

$$= \frac{1}{n}\left[\underbrace{\sin\left[n\left(2\pi - \Psi_n\right)\right]}_{\sin(-n\Psi_n)} - \sin\left(-n\Psi_n\right)\right] , \tag{A.42}$$

$$= 0 . \tag{A.43}$$

So this term drops. In the second integral we can change the order of integration and summation, so we arrive at

$$2\sum_{k=1}^{\infty} v_k \int_0^{2\pi} \mathrm{d}\varphi \cos[k(\varphi - \Psi_k)] \cos[n(\varphi - \Psi_n)] = 2\pi \sum_{k=1}^{\infty} v_k \cos\left(k\Psi_k - n\Psi_n\right) \delta_{kn} , \tag{A.44}$$

$$= 2\pi v_n , \tag{A.45}$$

where we used orthogonality relation from eq. (A.37) to solve the integral. The argument of the resulting cosine function is zero, so it evaluates to one, as we evaluate the Kronecker Delta and remove the sum. Plugging all results together we arrive at the result

$$\left\langle \cos\left[n\left(\varphi - \Psi_n\right)\right]\right\rangle = \frac{1}{2\pi}\left[0 + 2\pi v_n\right] , \tag{A.46}$$

$$= v_n . \tag{A.47}$$

A.5. Derivation of multiparticle correlators

We want to verify eq. (2.20). Therefore, we start with eq. (2.17), multiply both sides with $\cos\left[n\left(\varphi_1 - \varphi_2\right)\right]$ and integrate from 0 to 2π which results in

$$\begin{aligned} & \int_0^{2\pi} \mathrm{d}\varphi_1 \int_0^{2\pi} \mathrm{d}\varphi_1 \cos\left[n\left(\varphi_1 - \varphi_2\right)\right] f(\varphi_1, \varphi_2) = \\ & \int_0^{2\pi} \mathrm{d}\varphi_1 f_{\varphi_1}(\varphi_1) \int_0^{2\pi} \mathrm{d}\varphi_2 \cos\left[n\left(\varphi_1 - \varphi_2\right)\right] f_{\varphi_2}(\varphi_2) . \end{aligned} \tag{A.48}$$

The left hand side is by definition the expectation value $\langle \cos\left[n\left(\varphi_1 - \varphi_2\right)\right]\rangle$. To compute the left hand side, we start by evaluating the integral over φ_2 first, which reads

$$\begin{aligned} &\int_0^{2\pi} \mathrm{d}\varphi_2 f_{\varphi_2}(\varphi_2) \cos\left[n\left(\varphi_1 - \varphi_2\right)\right] = \\ &\frac{1}{2\pi} \int_0^{2\pi} \mathrm{d}\varphi_2 \cos\left[n\left(\varphi_1 - \varphi_2\right)\right] \left[1 + 2\sum_{k=1}^{\infty} v_k \cos[k(\varphi_2 - \Psi_k)]\right] . \end{aligned} \tag{A.49}$$

We can drop the first term inside the bracket, since we know from eq. (A.43) that this term vanishes. In the second part we can once again invert the order of integration and summation and arrive at

$$2\sum_{k=1}^{\infty} v_k \int_0^{2\pi} \mathrm{d}\varphi_2 \cos[n(\varphi_1 - \varphi_2)] \cos[k(\varphi_2 - \Psi_k)] = 2\pi \sum_{k=1}^{\infty} v_k \cos\left(n\varphi_1 - k\Psi_k\right) \delta_{kn} ,$$

(A.50)

$$= 2\pi v_n \cos\left[n\left(\varphi_1 - \Psi_n\right)\right] , \tag{A.51}$$

where we used eq. (A.37) again to solve the integral. In total the integration over φ_2 results in

$$\int_0^{2\pi} \mathrm{d}\varphi_2 f_{\varphi_2}(\varphi_2) \cos\left[n\left(\varphi_1 - \varphi_2\right)\right] = \frac{1}{2\pi}\left[0 + 2\pi v_n \cos\left[n\left(\varphi_1 - \Psi_n\right)\right]\right] , \tag{A.52}$$

$$= v_n \cos\left[n\left(\varphi_1 - \Psi_n\right)\right] . \tag{A.53}$$

Plugging this result into eq. (A.48) gives

$$\langle \cos\left[n\left(\varphi_1 - \varphi_2\right)\right]\rangle = v_n \underbrace{\int_0^{2\pi} \mathrm{d}\varphi_1 f_{\varphi_1}(\varphi_1) \cos\left[n\left(\varphi_1 - \Psi_n\right)\right]}_{v_n} , \tag{A.54}$$

$$= v_n^2 , \tag{A.55}$$

where we realized that the remaining integral is the expectation value we computed in appendix A.4.

A.6. Q-vector

We want to verify eq. (2.21). For this reason we first want to verify this relation:

$$\langle \cos\left[n\left(\varphi_1 - \varphi_2\right)\right]\rangle = \left\langle e^{in(\varphi_1 - \varphi_2)} \right\rangle . \tag{A.56}$$

Evaluating the right hand side of this expression results in

$$\left\langle e^{in(\varphi_1-\varphi_2)} \right\rangle = \langle \cos\left[n\left(\varphi_1-\varphi_2\right)\right]\rangle + i\,\langle \sin\left[n\left(\varphi_1-\varphi_2\right)\right]\rangle\,, \tag{A.57}$$

where we used Euler's identity to rewrite the exponential function and the linearity of the integral to split the expectation value operator onto both summands. All that is left to show is that the expectation value of the sine function vanishes. The expectation value reads

$$\langle \sin\left[n\left(\varphi_1-\varphi_2\right)\right]\rangle = \int_0^{2\pi} \mathrm{d}\varphi_1 \int_0^{2\pi} \mathrm{d}\varphi_2 \sin\left[n\left(\varphi_1-\varphi_2\right)\right] f(\varphi_1,\varphi_2)\,, \tag{A.58}$$

$$= \int_0^{2\pi} \mathrm{d}\varphi_1 \int_0^{2\pi} \mathrm{d}\varphi_2 \sin\left[n\left(\varphi_1-\varphi_2\right)\right] f_{\varphi_1}(\varphi_1) f_{\varphi_2}(\varphi_2)\,. \tag{A.59}$$

We start by performing the integral over φ_2. The integral reads

$$\begin{aligned} &\int_0^{2\pi} \mathrm{d}\varphi_2 f_{\varphi_2}(\varphi_2) \sin\left[n\left(\varphi_1-\varphi_2\right)\right] = \\ &\frac{1}{2\pi}\int_0^{2\pi} \mathrm{d}\varphi_2 \sin\left[n\left(\varphi_1-\varphi_2\right)\right] \left[1 + 2\sum_{k=1}^{\infty} v_k \cos[k(\varphi_2-\Psi_k)]\right]\,. \end{aligned} \tag{A.60}$$

We can drop the 1 inside the bracket, because

$$\int_0^{2\pi} \mathrm{d}\varphi \sin\left[n\left(\varphi-\Psi_n\right)\right] = -\frac{1}{n}\cos\left[n\left(\varphi-\Psi_n\right)\right]\Big|_0^{2\pi}\,, \tag{A.61}$$

$$= -\frac{1}{n}\left[\underbrace{\cos\left[n\left(2\pi-\Psi_n\right)\right]}_{\cos(-n\Psi_n)} - \cos\left(-n\Psi_n\right)\right]\,, \tag{A.62}$$

$$= 0\,. \tag{A.63}$$

The other term inside the bracket, after changing the order of summation and integration, computes to

$$2\sum_{k=1}^{\infty} v_k \int_0^{2\pi} \mathrm{d}\varphi_2 \sin[n(\varphi_1-\varphi_2)]\cos[i(\varphi_2-\Psi_k)] = 2\pi\sum_{k=1}^{\infty} v_k \sin\left(n\varphi_1 - k\Psi_k\right)\delta_{kn}\,, \tag{A.64}$$

$$= 2\pi v_n \sin\left[n\left(\varphi_1-\Psi_n\right)\right]\,, \tag{A.65}$$

where we used eq. (A.38) to evaluate the integral. In total the integration over φ_2 results in

$$\int_0^{2\pi} \mathrm{d}\varphi_2 f_{\varphi_2}(\varphi_2) \sin\left[n\left(\varphi_1-\varphi_2\right)\right] = \frac{1}{2\pi}\left[0 + 2\pi v_n \sin\left[n\left(\varphi_1-\Psi_n\right)\right]\right]\,, \tag{A.66}$$

$$= v_n \sin\left[n\left(\varphi_1-\Psi_n\right)\right]\,. \tag{A.67}$$

Plugging this result into eq. (A.48) gives

$$\langle \sin\left[n\left(\varphi_1 - \varphi_2\right)\right]\rangle = v_n \int_0^{2\pi} \mathrm{d}\varphi_1 f_{\varphi_1}(\varphi_1) \sin\left[n\left(\varphi_1 - \Psi_n\right)\right] . \tag{A.68}$$

The remaining integral reads

$$\begin{aligned} &\int_0^{2\pi} \mathrm{d}\varphi_1 f_{\varphi_1}(\varphi_1) \sin\left[n\left(\varphi_1 - \Psi_n\right)\right] = \\ &\int_0^{2\pi} \mathrm{d}\varphi_1 \sin\left[n\left(\varphi_1 - \Psi_n\right)\right] \left[1 + 2\sum_{k=1}^{\infty} v_k \cos[k(\varphi_1 - \Psi_k)]\right] . \end{aligned} \tag{A.69}$$

The integral over 1 inside the break evaluates again to zero. The remaining integral, after inverting the order of integration and summation, evaluates to

$$2\sum_{k=1}^{\infty} v_k \int_0^{2\pi} \mathrm{d}\varphi_1 \sin[n(\varphi_1 - \Psi_n)] \cos[k(\varphi_2 - \Psi_k)] = 2\pi \sum_{k=1}^{\infty} v_k \sin\left(n\Psi_n - k\Psi_k\right) \delta_{kn} ,$$

$$\tag{A.70}$$

$$= 2\pi v_n \sin\left(0\right) , \tag{A.71}$$

$$= 0 , \tag{A.72}$$

which gives the final result

$$\langle \sin\left[n\left(\varphi_1 - \varphi_2\right)\right]\rangle = 0 . \tag{A.73}$$

Now that we verified eq. (A.56), we change perspective. Instead of evaluation the expectation value as an integral over a PDF, we evaluate it as a mean over a data set. Hence, we write

$$\left\langle e^{in(\varphi_1 - \varphi_2)} \right\rangle = \frac{1}{M\left(M-1\right)} \sum_{\substack{k,l=1 \\ k \neq l}}^{M} e^{in(\varphi_k - \varphi_l)} , \tag{A.74}$$

where we sum over all pairs φ_k and φ_l, except for the cases where $k = l$ to avoid autocorrelations. Because we do not compute these, in the prefactor we have to divide by $M(M-1)$ instead of M^2. Looking at eq. (2.22), we see that we can rewrite the prefactor as

$$\frac{1}{\binom{M}{2} 2!} = \frac{1}{\frac{M!}{2!(M-2)!} 2!} , \tag{A.75}$$

$$= \frac{(M-2)!}{M!} , \tag{A.76}$$

$$= \frac{1}{M\left(M-1\right)} , \tag{A.77}$$

which is the same prefactor as in eq. (A.74). In order to simplify further, we have a look at this identity:

$$\sum_{k,l=1}^{M} e^{in(\varphi_k-\varphi_l)} = \sum_{\substack{k,l=1\\k\neq l}}^{M} e^{in(\varphi_k-\varphi_l)} + \sum_{\substack{l=1\\l=k}}^{M} \underbrace{e^{in(\varphi_k-\varphi_l)}}_{=1\,\forall l}, \tag{A.78}$$

$$= \sum_{\substack{k,l=1\\k\neq l}}^{M} e^{in(\varphi_k-\varphi_l)} + M\,. \tag{A.79}$$

The left hand side can also be written as

$$\sum_{k,l=1}^{M} e^{in(\varphi_k-\varphi_l)} = \sum_{k,l=1}^{M} e^{in\varphi_k} e^{-in\varphi_l}\,, \tag{A.80}$$

$$= \left(\sum_{k=1}^{M} e^{in\varphi_k}\right)\left(\sum_{l=1}^{M} e^{-in\varphi_l}\right)\,, \tag{A.81}$$

$$= Q_n Q_n^*\,, \tag{A.82}$$

$$= |Q_n|^2\,. \tag{A.83}$$

This means we can rewrite eq. (A.74) to

$$\left\langle e^{in(\varphi_1-\varphi_2)}\right\rangle = \frac{1}{\binom{M}{2}2!}\left(\sum_{k,l=1}^{M} e^{in(\varphi_k-\varphi_l)} - M\right)\,, \tag{A.84}$$

$$= \frac{1}{\binom{M}{2}2!}\left(|Q_n|^2 - M\right) \tag{A.85}$$

and conclude the proof.

A.7. Cumulants

The main goal is to verify eq. (2.41). But before that, we need to show several other relations. Firstly, we want to explicitly show that

$$\left\langle\left\langle e^{\pm in\varphi}\right\rangle\right\rangle = 0\,. \tag{A.86}$$

Expanding the exponential function and the inner expectation value, which corresponds to computing the average with respect to φ, we receive

$$\left\langle e^{in\varphi}\right\rangle = \int_0^{2\pi} \mathrm{d}\varphi f\left(\varphi\right)\cos\left(n\varphi\right) \pm i\int_0^{2\pi} \mathrm{d}\varphi f\left(\varphi\right)\sin\left(n\varphi\right)\,. \tag{A.87}$$

Reusing results from previous calculations we can immediately write the result as

$$\left\langle e^{in\varphi} \right\rangle = 2\pi v_n \left[\cos(\Psi_n) \pm i \sin(\Psi_n)\right] . \tag{A.88}$$

Evaluating the outer expectation value, which corresponds to computing the average with respect to Ψ_n, gives

$$\begin{aligned}
\left\langle \left\langle e^{in\varphi} \right\rangle \right\rangle &= 2\pi v_n \left(\langle \cos(\Psi_n) \rangle - i \langle \sin(\Psi_n) \rangle\right) , && \text{(A.89)} \\
&= v_n \left(\int_0^{2\pi} \mathrm{d}\Psi_n \cos(\Psi_n) - i \int_0^{2\pi} \mathrm{d}\Psi_n \sin(\Psi_n) \right) , && \text{(A.90)} \\
&= 0 , && \text{(A.91)}
\end{aligned}$$

where we used the fact that the symmetry planes are uniformly randomly distributed between 0 and 2π, hence

$$\langle g(\Psi_n) \rangle = \frac{1}{2\pi} \int_0^{2\pi} \mathrm{d}\Psi_n g(\Psi_n) . \tag{A.92}$$

Next, we want to derive a general expression for a 3-particle cumulant. Therefore, we start with a 3-particle PDF and decompose it. For the sake of simplicity, we will immediately write the decomposition in terms of cumulants and moments, namely as

$$\begin{aligned}
\langle X_1 X_2 X_3 \rangle = &\langle X_1 \rangle \langle X_2 \rangle \langle X_3 \rangle \\
&+ \langle X_1 \rangle \langle X_2 X_3 \rangle_c + \langle X_2 \rangle \langle X_1 X_3 \rangle_c + \langle X_3 \rangle \langle X_1 X_3 \rangle_c \\
&+ \langle X_1 X_2 X_3 \rangle_c .
\end{aligned} \tag{A.93}$$

Inverting this to isolate the 3-particle cumulant, we receive

$$\begin{aligned}
\langle X_1 X_2 X_3 \rangle_c = &\langle X_1 X_2 X_3 \rangle \\
&- \langle X_1 \rangle \langle X_2 X_3 \rangle_c - \langle X_2 \rangle \langle X_1 X_3 \rangle_c - \langle X_3 \rangle \langle X_1 X_2 \rangle_c \\
&- \langle X_1 \rangle \langle X_2 \rangle \langle X_3 \rangle .
\end{aligned} \tag{A.94}$$

Using the usual parameterization $X_1 = e^{\pm in\varphi_1}$, we see immediately that terms proportional to a 1-particle average drop if we compute all event averages. But we can also conclude that the 3-particle correlator will vanish, because the single event average will again produce a term which will be proportional to the cosine of the symmetry plane and the all event average over this term vanishes again. Which means in total

$$\left\langle \left\langle e^{in(\pm\varphi_1 \pm \varphi_2 \pm \varphi_3)} \right\rangle_c \right\rangle = 0 . \tag{A.95}$$

Now we decompose the joint PDF of 4 particles and arrive at

$$\begin{aligned}
\langle X_1 X_2 X_3 X_4 \rangle = &\langle X_1 \rangle \langle X_2 \rangle \langle X_3 \rangle \langle X_4 \rangle \\
&+ \langle X_1 \rangle \langle X_2 X_3 X_4 \rangle_c + \langle X_2 \rangle \langle X_1 X_3 X_4 \rangle_c \\
&+ \langle X_3 \rangle \langle X_1 X_2 X_4 \rangle_c \langle X_4 \rangle \langle X_1 X_2 X_3 \rangle_c \\
&+ \langle X_1 X_2 \rangle_c \langle X_3 X_4 \rangle_c + \langle X_1 X_3 \rangle \langle X_2 X_4 \rangle_c + \langle X_1 X_4 \rangle \langle X_2 X_3 \rangle_c \\
&+ \langle X_1 X_2 X_3 X_4 \rangle_c .
\end{aligned} \tag{A.96}$$

Inverting and isolating the 4-particle cumulant reads

$$\begin{aligned}\langle X_1X_2X_3X_4\rangle_c = &\langle X_1X_2X_3X_4\rangle \\ &- \langle X_1\rangle\langle X_2X_3X_4\rangle_c - \langle X_2\rangle\langle X_1X_3X_4\rangle_c \\ &- \langle X_3\rangle\langle X_1X_2X_4\rangle_c\langle X_4\rangle\langle X_1X_2X_3\rangle_c \\ &- \langle X_1X_2\rangle_c\langle X_3X_4\rangle_c - \langle X_1X_3\rangle_c\langle X_2X_4\rangle_c - \langle X_1X_4\rangle_c\langle X_2X_3\rangle_c \\ &- \langle X_1\rangle\langle X_2\rangle\langle X_3\rangle\langle X_4\rangle\,.\end{aligned} \tag{A.97}$$

Setting $X_1 = e^{in\varphi_1}$, $X_2 = e^{in\varphi_2}$, $X_3 = e^{-in\varphi_3}$ and $X_4 = e^{-in\varphi_4}$, adding the all event average and dropping all 1- and 3-particle correlators gives

$$\begin{aligned}\left\langle\left\langle e^{in(\varphi_1+\varphi_2-\varphi_3-\varphi_4)}\right\rangle_c\right\rangle &= \left\langle\underbrace{\left\langle e^{in(\varphi_1+\varphi_2-\varphi_3-\varphi_4)}\right\rangle}_{=v_n^4}\right\rangle \\ &\quad - \underbrace{\left\langle\left\langle e^{in(\varphi_1+\varphi_2)}\right\rangle\right\rangle}_{=0}\underbrace{\left\langle\left\langle e^{in(-\varphi_3-\varphi_4)}\right\rangle\right\rangle}_{=0} \\ &\quad - \left\langle\underbrace{\left\langle e^{in(\varphi_1-\varphi_3)}\right\rangle}_{=v_n^2}\right\rangle\left\langle\underbrace{\left\langle e^{in(\varphi_2-\varphi_4)}\right\rangle}_{=v_n^2}\right\rangle \\ &\quad - \left\langle\underbrace{\left\langle e^{in(\varphi_1-\varphi_4)}\right\rangle}_{=v_n^2}\right\rangle\left\langle\underbrace{\left\langle e^{in(\varphi_2-\varphi_3)}\right\rangle}_{=v_n^2}\right\rangle\,,\end{aligned} \tag{A.98}$$

$$= \left\langle v_n^4\right\rangle - 2\left\langle v_n^2\right\rangle^2\,, \tag{A.99}$$

where we recognize the 2- and 4-particle correlators and that

$$\left\langle\left\langle e^{\pm in(\varphi_k+\varphi_l)}\right\rangle\right\rangle = 0\,. \tag{A.100}$$

Like with the 1-particle cumulant, if we evaluate the single even average we get a term which will be proportional to the cosine or sine of the symmetry plane Ψ and these terms evaluate to 0 if we take the all-event average afterwards.

A.8. 2-particle correlators with weighted sum

We want to verify eq. (2.54). We will start with the following identity, where

$$\sum_{k,l=1}^{M} w_k w_l e^{in(\varphi_k-\varphi_l)} = \sum_{\substack{k,l=1\\k\neq l}}^{M} w_k w_l e^{in(\varphi_k-\varphi_l)} + \sum_{\substack{k,l=1\\k=l}}^{M} \underbrace{w_k w_l}_{w_k^2} \underbrace{e^{in(\varphi_k-\varphi_l)}}_{=1}, \tag{A.101}$$

$$= \sum_{\substack{k,l=1\\k\neq l}}^{M} w_k w_l e^{in(\varphi_k-\varphi_l)} + \sum_{k=1}^{M} w_k^2 \,. \tag{A.102}$$

This we can be rewritten as

$$\sum_{\substack{k,l=1\\k\neq l}}^{M} w_k w_l e^{in(\varphi_k-\varphi_l)} = \sum_{k,l=1}^{M} w_k w_l e^{in(\varphi_k-\varphi_l)} - \sum_{k=1}^{M} w_k^2 \,, \tag{A.103}$$

$$= \left(\sum_{k=1}^{M} w_k e^{in\varphi_k}\right)\left(\sum_{l=1}^{M} w_l e^{-in\varphi_l}\right) - \sum_{k=1}^{M} w_k^2 \,, \tag{A.104}$$

$$= |Q_n|^2 - \sum_{k=1}^{M} w_k^2 \,. \tag{A.105}$$

The final step is now rewriting

$$\langle 2 \rangle = \frac{\sum\limits_{\substack{k,l=1\\k\neq l}}^{M} w_k w_l e^{in(\varphi_k-\varphi_l)}}{\sum\limits_{\substack{k,l=1\\k\neq l}}^{M} w_k w_l} \,, \tag{A.106}$$

$$= \frac{1}{\sum\limits_{\substack{k,l=1\\k\neq l}}^{M} w_k w_l} \left(|Q_n|^2 - \sum_{k=1}^{M} w_k^2\right) \,, \tag{A.107}$$

which concludes the proof.

A.9. Expectation value of 2-particle correlator with p_{T} dependence

We want to compute the expectation value of a 2-particle correlator when the flow harmonics are a function of transverse momentum. We start with the generic formula of

2-particle correlator

$$\int_0^{2\pi} \mathrm{d}\varphi_1 \int_0^{\infty} \mathrm{d}p_1 \int_0^{2\pi} \mathrm{d}\varphi_2 \int_0^{\infty} \mathrm{d}p_2 \cos\left[n\left(\varphi_1 - \varphi_2\right)\right] f\left(\varphi_1, p_1; \varphi_2, p_2\right) = \int_0^{\infty} \mathrm{d}p_1 f_{p_1}(p_1) \int_0^{\infty} \mathrm{d}p_2 f_{p_2}(p_2) \int_0^{2\pi} \mathrm{d}\varphi_1 f_{\varphi_1}(\varphi_1, p_1) \int_0^{2\pi} \mathrm{d}\varphi_2 f_{\varphi_2}(\varphi_2, p_2) \cos\left[n\left(\varphi_1 - \varphi_2\right)\right] , \tag{A.108}$$

where we split the joint PDF $f\left(\varphi_1, p_1; \varphi_2, p_2\right)$ into marginal PDF for the azimuthal angels $\varphi_{1,2}$ and the momenta $p_{1,2}$. The marginal PDF of $\varphi_{1,2}$ follow a Fourier series as described by eq. (2.1) with the exception that v_n are now functions of p. The marginal PDF of transverse momentum $p_{1,2}$ follow a Boltzmann distribution as described by eq. (2.56). We can solve the integral over the azimuthal angles immediately by reusing the results from appendix A.5. The result reads

$$\left\langle \cos\left[n\left(\varphi_1 - \varphi_2\right)\right]\right\rangle = \int_0^{\infty} \mathrm{d}p_1 f_{p_1}(p_1) v_n(p_1) \int_0^{\infty} \mathrm{d}p_2 f_{p_2}(p_2) v_n(p_2) , \tag{A.109}$$

$$= \left[\int_0^{\infty} \mathrm{d}p f(p) v_n(p)\right]^2 , \tag{A.110}$$

$$= \left[\mathcal{N} \int_0^{\infty} \mathrm{d}p\, v_n(p) p \exp\left(-\frac{\sqrt{p^2 + m^2}}{T}\right)\right]^2 . \tag{A.111}$$

Using the parameters stated in section 2.9.2 and eq. (2.57) for the functional dependence of v_2 on p_T we can compute the integral numerically which results in

$$\left\langle \cos\left[n(\varphi_1 - \varphi_2)\right]\right\rangle = 1.6787 \times 10^{-2} . \tag{A.112}$$

A.10. Fully generic 2-particle correlator with Q-vectors

We want to verify that

$$\langle 2\rangle_{n_1,n_2} = \frac{N\langle 2\rangle_{n_1,n_2}}{D\langle 2\rangle_{n_1,n_2}} \tag{A.113}$$

holds with the expression of $N\langle 2\rangle_{n_1,n_2}$ as given by eq. (2.72) and $D\langle 2\rangle_{n_1,n_2}$ as given by eq. (2.73). Therefore, we plug the values into the definitions and compute

$$N\langle 2\rangle_{n_1,n_2} = Q_{n_1,1}Q_{n_2,1} - Q_{n_1+n_2,2}\,, \tag{A.114}$$

$$= \sum_{k=1}^{M} w_k e^{in_1\varphi_k} \sum_{l=1}^{M} w_l e^{in_1\varphi_l} - \sum_{r=1}^{M} w_r^2 e^{i(n_1+n_2)\varphi_r}\,, \tag{A.115}$$

$$= \sum_{k,l=1}^{M} w_k w_l e^{i(n_1\varphi_k+n_2\varphi_l)} - \sum_{r=1}^{M} w_r^2 e^{i(n_1+n_2)\varphi_r}\,, \tag{A.116}$$

$$= \sum_{\substack{k,l=1\\k\neq l}}^{M} w_k w_l e^{i(n_1\varphi_k+n_2\varphi_l)}\,. \tag{A.117}$$

And for the Denominator we receive

$$D\langle 2\rangle_{n_1,n_2} = Q_{0,1}^2 - Q_{0,2}\,, \tag{A.118}$$

$$= \left(\sum_{k=1}^{M} w_k\right)^2 - \sum_{r=1}^{M} w_r^2\,, \tag{A.119}$$

$$= \sum_{k,l=1}^{M} w_k w_l - \sum_{r=1}^{M} w_r^2\,, \tag{A.120}$$

$$= \sum_{\substack{k,l=1\\k\neq l}}^{M} w_k w_l\,. \tag{A.121}$$

Putting everything together we get

$$\langle 2\rangle_{n_1,n_2} = \frac{N\langle 2\rangle_{n_1,n_2}}{D\langle 2\rangle_{n_1,n_2}}\,, \tag{A.122}$$

$$= \frac{\sum\limits_{\substack{k,l=1\\k\neq l}}^{M} w_k w_l e^{i(n_1\varphi_k+n_2\varphi_l)}}{\sum\limits_{\substack{k,l=1\\k\neq l}}^{M} w_k w_l}\,, \tag{A.123}$$

concluding the proof.

A.11. Derivation of SC(n, m)

We want to verify that eq. (2.83). Using the previous results from section appendix A.7 we can write

$$\mathrm{SC}(n,m) = \left\langle \left\langle e^{in(\varphi_1-\varphi_2)+im(\varphi_3-\varphi_4)} \right\rangle_c \right\rangle , \tag{A.124}$$

$$= \left\langle \underbrace{\left\langle e^{in(\varphi_1-\varphi_2)+im(\varphi_3-\varphi_4)} \right\rangle}_{=v_n^2 v_m^2} \right\rangle \tag{A.125}$$

$$- \left\langle \underbrace{\left\langle e^{in(\varphi_1-\varphi_2)} \right\rangle}_{=v_n^2} \right\rangle \left\langle \underbrace{\left\langle e^{im(\varphi_3-\varphi_4)} \right\rangle}_{=v_m^2} \right\rangle \tag{A.126}$$

$$- \left\langle \underbrace{\left\langle e^{in\varphi_1+im\varphi_3)} \right\rangle}_{=0} \right\rangle \left\langle \underbrace{\left\langle e^{-in\varphi_2-im\varphi_4)} \right\rangle}_{=0} \right\rangle \tag{A.127}$$

$$- \left\langle \underbrace{\left\langle e^{in\varphi_1-im\varphi_4)} \right\rangle}_{=0} \right\rangle \left\langle \underbrace{\left\langle e^{-in\varphi_2+im\varphi_3)} \right\rangle}_{=0} \right\rangle , \tag{A.128}$$

$$= \left\langle v_n^2 v_m^2 \right\rangle - \left\langle v_n^2 \right\rangle \left\langle v_m^2 \right\rangle , \tag{A.129}$$

where we used that $\left\langle e^{\pm in\varphi_k \pm im\varphi_l} \right\rangle = 0$ since $n - m \neq 0$ for $n \neq m$.

A.12. Analytical result for Toy Monte Carlo study for SC(2,3)

We want to verify the analytical result for SC(2,3) in section 2.13. Using the PDF as given by eq. (2.85) as well as the limits for $v_2 \in [0.15, 0.25]$ and $v_3 \in [0.15, 0.15]$, we

explicitly write

$$\mathrm{SC}(2,3) = \left\langle v_2^2 v_3^2 \right\rangle - \left\langle v_2^2 \right\rangle \left\langle v_3^2 \right\rangle , \tag{A.130}$$

$$= \int_{0.15}^{0.25} \mathrm{d}v_2 \int_{0.05}^{0.15} \mathrm{d}v_3 f(v_2, v_3) v_2^2 v_3^2 \tag{A.131}$$

$$- \int_{0.15}^{0.25} \mathrm{d}v_2 \int_{0.05}^{0.15} \mathrm{d}v_3 f(v_2, v_3) v_2^2 \tag{A.132}$$

$$- \int_{0.15}^{0.25} \mathrm{d}v_2 \int_{0.05}^{0.15} \mathrm{d}v_3 f(v_2, v_3) v_3^2 , \tag{A.133}$$

$$= \mathcal{N} \int_{0.15}^{0.25} \mathrm{d}v_2 \int_{0.05}^{0.15} \mathrm{d}v_3 (v_2 + v_3) v_2^2 v_3^2 \tag{A.134}$$

$$- \mathcal{N} \int_{0.15}^{0.25} \mathrm{d}v_2 \int_{0.05}^{0.15} \mathrm{d}v_3 (v_2 + v_3) v_2^2 \tag{A.135}$$

$$- \mathcal{N} \int_{0.15}^{0.25} \mathrm{d}v_2 \int_{0.05}^{0.15} \mathrm{d}v_3 (v_2 + v_3) v_3^2 . \tag{A.136}$$

The normalization constant can be computed with

$$\mathcal{N} = \left(\int_{0.15}^{0.25} \mathrm{d}v_2 \int_{0.05}^{0.15} \mathrm{d}v_3 f(v_2, v_3) \right)^{-1} , \tag{A.137}$$

$$= \left(\int_{0.15}^{0.25} \mathrm{d}v_2 \int_{0.05}^{0.15} \mathrm{d}v_3 (v_2 + v_3) \right)^{-1} . \tag{A.138}$$

Plugging in all the values we receive the numerical result

$$\mathrm{SC}(2,3) = -2.7700 \times 10^{-7} . \tag{A.139}$$

Bibliography

[1] J. Adam et al. "Correlated Event-by-Event Fluctuations of Flow Harmonics in Pb-Pb Collisions at $\sqrt{s_{\mathrm{NN}}} = 2.76$ TeV". In: *Physical Review Letters* 117.18 (Oct. 2016).

[2] B. Alver et al. *The PHOBOS Glauber Monte Carlo*. 2008.

[3] Pedro Bicudo, Melanie Cardoso, and Nuno Cardoso. "QCD confinement and chiral crossovers, two critical points". In: (Feb. 2011).

[4] Ante Bilandzic et al. "Generic framework for anisotropic flow analyses with multiparticle azimuthal correlations". In: *Phys. Rev. C* 89 (6 June 2014), p. 064904.

[5] Wojciech Broniowski and Wojciech Florkowski. "Geometric relation between centrality and the impact parameter in relativistic heavy-ion collisions". In: *Phys. Rev. C* 65 (2 Jan. 2002), p. 024905.

[6] Murray Gell-Mann. *A schematic model of baryons and mesons*. North-Holland Publishing Company, 1964.

[7] Jeff Greensite. *An introduction to the confinement problem*. Springer, 2020.

[8] David J. Gross and Frank Wilczek. "Ultraviolet Behavior of Non-Abelian Gauge Theories". In: *Phys. Rev. Lett.* 30 (26 June 1973), pp. 1343–1346.

[9] Miklos Gyulassy and Xin-Nian Wang. "HIJING 1.0: A Monte Carlo program for parton and particle production in high energy hadronic and nuclear collisions". In: *Computer Physics Communications* 83.2-3 (Dec. 1994), pp. 307–331.

[10] Ulrich Heinz and Maurice Jacob. *Evidence for a New State of Matter: An Assessment of the Results from the CERN Lead Beam Programme*. 2000.

[11] Ulrich Heinz and Raimond Snellings. "Collective Flow and Viscosity in Relativistic Heavy-Ion Collisions". In: *Annual Review of Nuclear and Particle Science* 63.1 (Oct. 2013), pp. 123–151.

[12] Ulrich W. Heinz. *"RHIC serves the perfect fluid" – Hydrodynamic flow of the QGP*. 2005.

[13] F. Karsch and E. Laermann. *Thermodynamics and in-medium hadron properties from lattice QCD*. 2003.

[14] Peter F. Kolb. "v_4 : A small, but sensitive observable for heavy ion collisions". In: *Phys. Rev. C* 68 (3 Sept. 2003), p. 031902.

[15] Peter F. Kolb and Ulrich Heinz. *Hydrodynamic description of ultrarelativistic heavy-ion collisions*. 2003.

[16] P. K. Kovtun, D. T. Son, and A. O. Starinets. "Viscosity in Strongly Interacting Quantum Field Theories from Black Hole Physics". In: *Physical Review Letters* 94.11 (Mar. 2005).

[17] Lev Davidovich Landau. "On the multiparticle production in high-energy collisions". In: 1953.

[18] C. Loizides. "Glauber modeling of high-energy nuclear collisions at the subnucleon level". In: *Phys. Rev. C* 94 (2 Aug. 2016), p. 024914.

[19] Michael L. Miller et al. "Glauber Modeling in High-Energy Nuclear Collisions". In: *Annual Review of Nuclear and Particle Science* 57.1 (Nov. 2007), pp. 205–243.

[20] Cindy Mordasini. "Generalisation of the Cumulants of Flow Amplitudes to the higher orders. Verallgemeinerung der Kumulanten der Flussamplituden auf die höheren Ordnungen". Presented 13 Apr 2021. Feb. 2021.

[21] J. Scott Moreland, Jonah E. Bernhard, and Steffen A. Bass. "Alternative ansatz to wounded nucleon and binary collision scaling in high-energy nuclear collisions". In: *Phys. Rev. C* 92.1 (2015), p. 011901.

[22] H. Niemi, K. J. Eskola, and R. Paatelainen. "Event-by-event fluctuations in a perturbative QCD + saturation + hydrodynamics model: Determining QCD matter shear viscosity in ultrarelativistic heavy-ion collisions". In: *Physical Review C* 93.2 (Feb. 2016).

[23] H. Niemi et al. "Event-by-event distributions of azimuthal asymmetries in ultrarelativistic heavy-ion collisions". In: *Physical Review C* 87.5 (May 2013).

[24] R. Nouicer. "New state of nuclear matter: Nearly perfect fluid of quarks and gluons in heavy-ion collisions at RHIC energies". In: *The European Physical Journal Plus* 131.3 (Mar. 2016).

[25] Jean-Yves Ollitrault. "Anisotropy as a signature of transverse collective flow". In: *Phys. Rev. D* 46 (1 July 1992), pp. 229–245.

[26] Roman Pasechnik and Michal Šumbera. "Phenomenological Review on Quark–Gluon Plasma: Concepts vs. Observations". In: *Universe* 3.1 (), p. 7.

[27] H. David Politzer. "Reliable Perturbative Results for Strong Interactions?" In: *Phys. Rev. Lett.* 30 (26 June 1973), pp. 1346–1349.

[28] Hugh David Politzer. *Asymptotic Freedom; an approach to strong interactions*.

[29] S M Sanches, D A Fogaça, and F S Navarra. "The time evolution of the quark gluon plasma in the early Universe". In: *Journal of Physics: Conference Series* 630 (July 2015), p. 012028.

[30] Sourav Sarkar, Helmut Satz, and Bikash Sinha. *The physics of the quark-gluon plasma introductory lectures*. Springer Berlin, 2013.

[31] Edward Shuryak. "Strongly coupled quark-gluon plasma in heavy ion collisions". In: *Reviews of Modern Physics* 89.3 (July 2017).

[32] Edward Shuryak. "What RHIC experiments and theory tell us about properties of quark–gluon plasma?" In: *Nuclear Physics A* 750.1 (Mar. 2005), pp. 64–83.

[33] P. Skands. "Introduction to QCD". In: *Searching for New Physics at Small and Large Scales*. WORLD SCIENTIFIC, Sept. 2013.

[34] George Sterman. "Some Basic Concepts of Perturbative QCD". In: (2008).

[35] M. Tanabashi et al. "Review of Particle Physics". In: *Phys. Rev. D* 98 (3 Aug. 2018), p. 030001.

[36] S. Voloshin and Y. Zhang. "Flow study in relativistic nuclear collisions by Fourier expansion of azimuthal particle distributions". In: *Zeitschrift für Physik C Particles and Fields* 70.4 (Dec. 1996), pp. 665–671.

[37] Xin-Nian Wang and Miklos Gyulassy. "hijing: A Monte Carlo model for multiple jet production in pp, pA, and AA collisions". In: *Phys. Rev. D* 44 (11 Dec. 1991), pp. 3501–3516.

[38] Li Yan. "A flow paradigm in heavy-ion collisions". In: *Chinese Physics C* 42.4 (Apr. 2018), p. 042001.

[39] G. Zweig. "An SU(3) model for strong interaction symmetry and its breaking. Version 1". In: (Jan. 1964).

[40] G. Zweig. "An SU(3) model for strong interaction symmetry and its breaking. Version 2". In: *DEVELOPMENTS IN THE QUARK THEORY OF HADRONS. VOL. 1. 1964 - 1978*. Ed. by D. B. Lichtenberg and Simon Peter Rosen. Feb. 1964, pp. 22–101.